Università degli Studi di Padova

Dipartimento di Fisica e Astronomia "Galileo Galilei"

Corso di Laurea Magistrale in Astronomia

Tesi di Laurea Magistrale in Astronomia

Calibrating the TP-AGB Phase through Resolved Stellar Populations in the Small Magellanic Cloud

Relatore: Prof. Paola Marigo
Correlatore: Dr. Léo Girardi

Laureanda: Giada Pastorelli

Anno Accademico 2014-2015

29/09/2015

Contents

List of Figures

List of Tables

Abstract

The modelling of the Thermally Pulsing Asymptotic Giant Branch (TP-AGB) phase is crucial for our understanding of galaxy evolution and for the derivation of basic galaxy properties, i.e. mass and age, up to high redshift. Despite its importance, this evolutionary phase is still affected by large uncertainties. The aim of this Thesis is to provide a starting point for extending the calibration of the latest TP-AGB models from Marigo and Girardi (2007) and Marigo et al. (2013) on the basis of the complete census of AGB stars in the Small Magellanic Cloud (SMC; Boyer et al., 2011). For this purpose, taking advantage of the spatially-resolved Star Formation History (SFH) of the SMC derived by Rubele et al. (2015), the population synthesis code TRILEGAL has been used to simulate the infrared photometry of the SMC. The resulting TP-AGB star counts, color-magnitude diagrams (CMDs), luminosity functions and color histograms have been analyzed and compared with their observed counterparts, in order to provide preliminary indications about the calibration of the key parameters of the TP-AGB evolution, i.e. stellar lifetimes, efficiencies of the third dredge-up and mass loss, dust production. Two sets of evolutionary tracks have been tested (Girardi et al., 2010; Marigo et al., 2013), as well as several circumstellar dust bolometric corrections based on models from Groenewegen (2006), Bressan et al. (1998) and Nanni et al. (2013; in prep.). In addition, the latest libraries of C- and M-star spectra have been used (Aringer et al. 2009; in prep.). This exploratory analysis shows that the observed TP-AGB star counts, the magnitude intervals and the average shapes of the luminosity functions, as well as the morphology of the observed CMDs, are better reproduced adopting the Marigo et al. (2013) evolutionary tracks. However, from the data-models comparison, some discrepancies have come to light. Although it is necessary to further investigate the nature of these discrepancies, these preliminary results suggest that: (i) the mass-loss efficiency of the most massive TP-AGB stars, experiencing the Hot Bottom Burning, should be increased, (ii) the formation of C-AGB stars needs to be made more efficient and/or the mass loss during this phase should be somewhat reduced, (iii) some prescriptions used in modelling the dust effects should be revised in order to accurately reproduce the most reddened TP-AGB stars.

Riassunto

La modellistica della fase di *Thermally Pulsing Asymptotic Giant Branch* (TP-AGB) risulta essere cruciale per la nostra comprensione dell'evoluzione delle galassie e per la determinazione di proprietà fondamentali delle galassie, ovvero massa ed età, fino ad alto *redshift*. L'obiettivo di questa tesi è fornire un punto di partenza per estendere la calibrazione dei più recenti modelli di TP-AGB (and Marigo and Girardi 2007, Marigo et al. 2013), sulla base del censimento completo delle stelle AGB nella piccola Nube di Magellano (SMC; Boyer et al. 2011). A tal fine, avvalendosi della storia di formazione stellare spazialmente risolta derivata da Rubele et al. (2015), il codice di sintesi di popolazioni stellari TRILEGAL è stato utilizzato per simulare la fotometria infrarossa della piccola Nube di Magellano. I risultanti conteggi di stelle TP-AGB, i diagrammi colore magnitudine, le funzioni di luminosità e gli istogrammi in colore sono stati analizzati e confrontati con le loro controparti osservate, al fine di fornire indicazioni preliminari sulla calibrazione dei parametri fondamentali dell'evoluzione della fase di TP-AGB, ovvero tempi di vita, efficienze di terzo dredge-up e perdita di massa, produzione di polvere. Sono stati testati due set di tracce evolutive (Girardi et al. 2010, Marigo et al. 2013), oltre a diverse correzioni bolometriche per la polvere circumstellare basate sui modelli di Groenewegen (2006), Bressan et al. (1998) e Nanni et al. (2013; in prep.). Inoltre, sono state utilizzate le più recenti librerie di spettri di stelle C ed M (Aringer et al. 2009; in prep.). Questa analisi esplorativa mostra che i conteggi stellari, gli intervalli di magnitudine e l'andamento medio delle funzioni di luminosità, in aggiunta alla morfologia dei diagrammi colore-magnitudine osservati, risultano essere riprodotti meglio utilizzando le tracce evolutive di Marigo et al. (2013). Sono tuttavia emerse delle discrepanze dal confronto tra modelli e osservazioni. Sebbene sia necessario studiare ulteriormente la natura di tali discrepanze, questi risultati preliminari suggeriscono che: (i) l'efficienza della perdita di massa delle stelle di TP-AGB più massicce, che subiscono il processo di Hot Bottom Burning, deve essere aumentata, (ii) la formazione delle stelle ricche di carbonio deve essere resa più efficiente e/o l'efficienza della perdita di massa in tale fase deve essere in qualche misura ridotta, (iii) alcune prescrizioni utilizzate nel modellare gli effetti della polvere devono essere riviste, per poter riprodurre le stelle di TP-AGB maggiormente arrossate.

Chapter 1

Introduction

The Thermally Pulsing Asymptotic Giant Branch (TP-AGB) is an advanced evolutionary phase during which stars of low- and intermediate-mass (1-8 $M_{\odot}$) experience helium and hydrogen double shell burning, reach their highest luminosities, synthesize new elements (e.g. ^{4}He, ^{12}C, ^{7}Li, Na, Mg, Al, slow-neutron capture nucleosynthesis products), go through mass loss via stellar winds and finally reach the stage of white dwarfs.

TP-AGB stars are red, cool giants therefore their luminosities peak in the near infrared (near-IR), while circumstellar dust emits at mid- to far-IR wavelengths. The impact of this evolutionary phase spans from chemical evolution and Spectral Energy Distribution (SED) of galaxies to dust production in galaxies at low and high redshift.

Despite its importance in our understanding of galaxy evolution, the TP-AGB modelling is still affected by large uncertainties due to the presence of several and interconnected processes (third dredge-up, hot bottom burning, stellar winds, long period pulsations, reprocessing of radiation by circumstellar dust in mass-losing stars), for which a robust theory is still lacking, though promising steps are being taken. In this context a fundamental contribution to a quantitative calibration of the TP-AGB as a function of age and metallicity can be provided by observations of resolved stellar populations. So far, the classical approach of the TP-AGB calibration as a function of age has been based on star counts, integrated fluxes and spectral classification of Magellanic Cloud (MC) clusters. However these clusters span a limited range of metallicity and are affected by large Poisson errors due to the low-number statistics of AGB stars. Therefore time has come to extend the calibration taking advantage of the excellent data of resolved TP-AGB populations in nearby galaxies, including MCs, M31, M33 and dwarf galaxies. These data make it possible to substantially improve the models calibration thanks to the detailed Star Formation History (SFH) and to the wider metallicity range covered.

The purpose of this Thesis is to provide a starting point for a reliable calibration of the latest TP-AGB models from Marigo and Girardi (2007), Marigo et al. (2013), based on the complete census of AGB stars in the Small Magellanic Cloud (SMC), photometrically classified by Boyer et al. (2011), on the basis of SAGE-SMC[1] data. The photometric data set includes optical photometry from the Magellanic Clouds Photometric Survey (MCPS), JHK_s photometry from the Two Micron All Sky Survey (2MASS) and the InfraRed Survey Facility (IRSF), mid-IR photometry from Spitzer's IRAC, far-IR photometry from MIPS.

Taking advantage of the spatially-resolved SFH of the SMC, derived for a 14 deg^2 area, split into 120 subregions, including its main body and wing (Rubele et al. 2015), the population synthesis code TRILEGAL (Girardi et al. 2005) will be used to simulate the photometry of the SMC. The latter will be compared to the SAGE-SMC data.

[1] Surveying the Agents of Galaxy Evolution in the Tidally Stripped, Low Metallicity SMC (SAGE-SMC).

The TRILEGAL code produces mock stellar catalogs for a galaxy given its mass, distance, Star Formation Rate (SFR) as a function of age, Age Metallicity Relation (AMR) and Initial Mass Function (IMF), as well as tables of stellar evolutionary tracks and bolometric corrections. The main output parameters are bolometric luminosity, intial and final mass, age, metallicity, period and photometry in a wide range of bandpasses, for each simulated star. The flexibility of the code gives the possibility to easily change all the input datasets, hence testing different models is quite straightforward.

Two sets of TP-AGB stellar evolutionary tracks will be tested. The first one corresponds to the evolutionary tracks contained in Girardi et al. (2010), which are basically the tracks described in Marigo and Girardi (2007) and Marigo et al. (2008) with some updates. The second set corresponds to evolutionary tracks computed by means of the `COLIBRI` code described in Marigo et al. (2013). Moreover, three different sets of dust bolometric corrections will be adopted. The first two sets are the same as in Marigo et al. (2008) and have been derived from two indipedent radiative transfer calculations, based on Groenewegen (2006) and Bressan et al. (1998), respectively. The third set is based on the new model for condensation and growth of dust grains developed by Nanni et al. (2013) and Nanni et al. (in prep.). Finally, two different library of carbon star spectra are adopted: the first is based on Loidl et al. (2001) and the second on Aringer et al. (2009).

Star counts, colors and morphology of Color-Magnitude Diagrams (CMDs) derived from the simulations, luminosity functions and color histograms will be compared to the observed ones, in order to better constrain key parameters of TP-AGB evolution, i.e. stellar lifetimes, efficiencies of the third dredge-up and mass loss, dust production.

The Thesis is organized as follows: Chapter 2 gives an overview of the evolution of low- and intermediate-mass stars, with a detailed description of the TP-AGB phase; Chapter 3 deals with the TP-AGB modelling, i.e. the stellar evolutionary models, the stellar atmosphere models and the dust models adopted, in addition to a brief overview about the present-day TP-AGB calibration; Chapter 4 presents the database that contains all information about the bulk of TP-AGB stars in the SMC, i.e the SAGE-SMC survey (Boyer et al. 2011), and the spatially-resolved SFH of the SMC derived by Rubele et al. (2015); Chapter 5 describes the population synthesis code TRILEGAL and all details about the computation of the synthetic photometry of the SMC; in Chapter 6 the synthetic photometry of the SMC is compared with the observations, by means of infrared CMDs, luminosity functions and color histograms, and the preliminary indications about the calibration of the key parameters of the TP-AGB phase are presented; Conclusions and future perspectives are discussed in Chapter 7.

Chapter 2

The Evolution of low- and intermediate-mass stars

In this section I will describe the evolution of low-and intermediate-mass stars from the Zero Age Main Sequence up (ZAMS) to the final stages of Planetary Nebulae (PN) and White Dwarfs (WD). Particular attention will be devoted to the Thermally Pulsing Asymptotic Giant Branch (TP-AGB) phase.

The description of the evolution of stars after the Main Sequence (MS) can be carried out more easily by classifying stars according to their initial mass M. Low-mass stars have masses in the range M $\approx$ 0.8 - 2 $M_{\odot}$. After the MS they develop a degenerate helium core and pass through the relatively long-lived Red Giant Branch Phase (RGB), that ends when the He is ignited in the core producing the so-called *Helium Flash*. The upper mass limit is often denoted as M_{HeF}. Intermediate-mass stars have masses between M $\approx M_{HeF}$ and M $\approx$ 8 $M_{\odot}$. The He ignition in the non-degenerate core is stable and leads to the development of a degenerate Carbon-Oxygen (C-O) core. Both low- and intermediate-mass stars evolve through the AGB phase during which they experience strong mass loss, with rates $\dot{M}$ that typically increase from $\dot{M} \approx 10^{-7}\ M_{\odot}/yr$ up to $\approx 10^{-4}\ M_{\odot}/yr$. This maximum level of mass-loss rate marks the onset of the so-called "super-wind" phase that causes a rapid removal of the whole envelope while the bare C-O core will eventually cool as a WD. Massive stars have masses greater than M $\approx$ 8 $M_{\odot}$ and have a non-degenerate CO core. Thus the ignition of C is stable and if mass is larger than M $\approx$ 11 $M_{\odot}$ the nuclear burning cycle can continue until the formation of an Iron core which collapses and produces a Supernova explosion.

2.1 The evolution prior to the AGB phase

2.1.1 The Main Sequence

After the pre-main sequence (PMS) phase, stars with masses larger than 0.08 $M_{\odot}$ stably burn and convert hydrogen into helium in their cores. According to their mass and composition, stars are located on the ZAMS in the Hertzsprung-Russell Diagram (HRD), from which they evolve towards higher luminosities and larger radii.

Examples of stellar evolutionary tracks of low- and intermediate-mass stars are shown in Figures 2.1 and 2.2 for two different values of initial metallicity, Z=0.001 and Z=0.02. The evolution from the PMS up to the TP-AGB phase is computed by means of the `PARSEC` code (Bressan et al. 2012), while the evolution from the first thermal pulse until the entire

envelope is removed by stellar winds is computed by means of the COLIBRI code (Marigo et al. 2013). Details about these two stellar evolution codes will be given in Section 3.1.

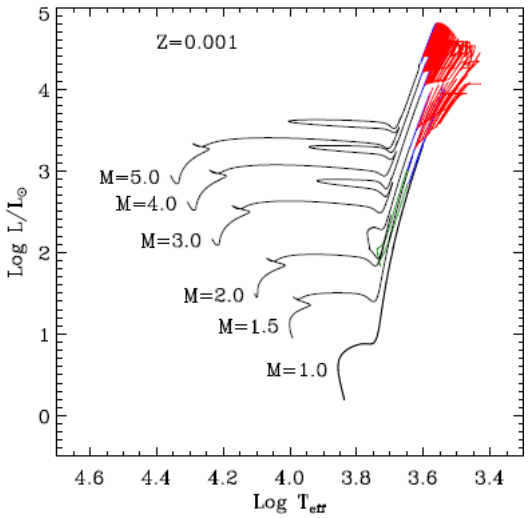

Figure 2.1: Evolutionary tracks for stars with Z=0.001 and masses of 1, 1.5, 2, 3, 4, 5 $M_{\odot}$. The blue lines correspond to thermal pulses developed when C/O < 1, red lines correspond to thermal pulses when C/O > 1. The He-burning phase of low-mass stars is plotted in green. The evolution prior to the TP-AGB phase is computed with PARSEC code, while the subsequent evolution, until the entire envelope is lost, by means of COLIBRI code.

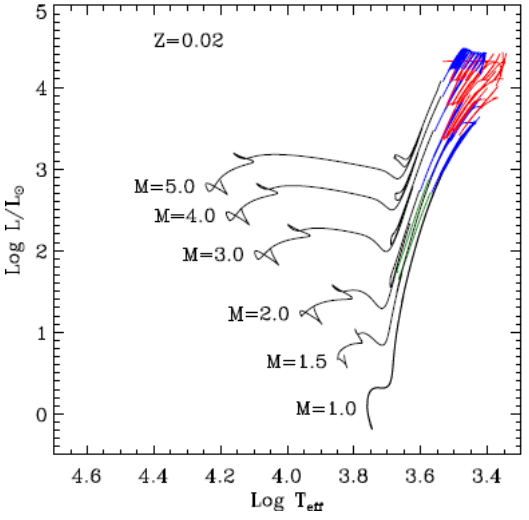

Figure 2.2: The same as in Fig. 2.1 with Z=0.02

Low-mass stars evolve towards higher effective temperature ($T_{\rm eff}$) and their increase in radius is modest, while stars with M $\gtrsim$ 1.3 $M_{\odot}$ move towards lower $T_{\rm eff}$ and their radii strongly increase.
During the central hydrogen burning stars are in hydrostatic equilibrium (HE) and thermal equilibrium (TE) and the evolution in the HRD is due to chemical evolution of the interior:

the conversion of H into He increases the mean molecular weight μ which in turn increases the luminosity L as we can see from the homology relation $L \propto \mu^4 M^3$, moreover the central temperature T_c remains almost constant due to the thermostat effect of nuclear reactions. In this situation, the ideal-gas law implies a decrease of the ratio between central pressure P_c and central density ρ_c, which causes non-homologous changes in the structure.

In stars more massive than 1.3 $M_\odot$ the dominant nuclear reaction cycle is the CNO cycle which is very sensitive to the temperature and allows only small variations of T_c and ρ_c: the envelope must expands in order to maintain HE and TE. The great sensitivity on temperature results also in the presence of convective cores which are well mixed and the consequence is an increase of the MS lifetime. During the evolution, the mass of the convective core decreases as a consequence of the decreasing opacity. When H is almost exhausted, T_c increases to maintain the energy production and when H is completely exhausted within the whole convective core, the nuclear reaction rate decreases, the energy losses at the surface exceed energy production in the center and the stars undergo an overall contraction to restore the thermal equilibrium. The contraction and the heating of the core makes the temperature sufficiently high for the ignition of the CNO cycle in a shell around the He core. This is the beginning of the hydrogen-shell burning phase.

The main nuclear reactions in stars with $M \lesssim 1.3\ M_\odot$ are those of the proton-proton chain (pp chain), which have a lower sensitivity to the temperature, hence allow a greater increase in T_c and ρ_c with respect to CNO cycle reactions. The HE can be maintained with a smaller expansion of the envelope and the result is a modest increase in radius and an evolution almost parallel to the ZAMS. Low-mass stars have radiative core therefore a H abundance gradient develops, resulting in a gradually outwards H depletion and in a smooth transition between core H-burning and H-shell burning.

2.1.2 The hydrogen-shell burning

Initially, the H-shell burning phase in intermediate-mass stars is relatively slow because stars are in TE and the H-burning occurs in a thick shell. When the He core mass exceeds the Schoenberg-Chandrasekhar limit core contraction accelerates and the envelope expands according to the "mirror principle". The temperature and density gradients between core and envelope increase and the H-burning proceeds in a thin shell. Until H-burning occurs in a thick shell the radius remains relatively small, while the more rapid expansion phase results in a decrease of the surface luminosity. The evolution across the HRD occurs on the Kelvin-Helmholtz timescale producing the so-called *Hertzsprung gap*, a distinctive feature of all intermediate-mass HRD.

The decreasing temperature and the increasing opacity of the expanding envelope make it unstable to convection, starting from the surface. The star is located closed to the Hayashi line in the HRD and begins to ascend the Red Giant Branch (RGB). During this phase, the expansion continues in response to core contraction and the luminosity increase at almost constant effective temperature. The H-shell burning phase of intermediate-mass stars occurs on a thermal timescale, making the RGB a very-short lived phase.

During the expansion, the base of the convective envelope reaches the region in which the material previously processed by H-burning and CNO cycle is present. This material is then mixed throughout the envelope and appears at the surface. The process is called *dredge-up* (DU) and occurs also in low-mass stars. The He core of intermediate-mass stars remains non-degenerate and the ignition of He in the core occurs in a stable way. The He ignition corresponds to a local maximum in luminosity and radius and marks the end of the RGB.

Low-mass stars have small or no convective core during central H-burning and their helium cores become degenerate before the central temperature is sufficiently high for helium ignition, therefore they settle into TE on the RGB. Stars with M $\lesssim$ 1.1 $M_\odot$ are below the SC limit and can remain in TE with an isothermal helium core. The nuclear energy generation gradually moves out to a thick shell and the core slowly grows in mass and contracts, while the envelope expands and the shell becomes thinner in mass. The helium core becomes degenerate and the pressure exerted by the degenerate electron allows the star to remain in HE and TE. At the same time the envelope has become largely convective and the star is located at the base of the RGB. Since low-mass stars can remain in HE and TE throughout H-shell burning there is no gap in HRD and this long-lived phase corresponds to the well populated Subgiant Branch (SGB) of old stellar populations in globular clusters. Since stars with masses between M $\approx$ 1.1 - 1.5 $M_\odot$ develop a small convective core during the MS, their evolutionary tracks exhibit a "hook" when H is exhausted in the center. The subsequent evolution is similar, the core remain in TE until it becomes degenerate on the RGB and this implies a slow evolution on the SGB. Stars with mass in the range M $\approx$ 1.5 - 2 $M_\odot$ reach their SC limit before the helium core has become degenerate and experience a rapid expansion until they reach the RGB, resulting in a small Hertzsprung gap.

2.1.3 The Red Giant Branch

The structure of a low-mass red giant can be considered as a function of its core mass and almost independent of the total mass of the star. A very tight relation between helium core mass M_c and luminosity exists and it can be approximated by the following relation that holds for $M_c \lesssim 0.5\ M_\odot$ ((Boothroyd and Sackmann 1988a)):

$$L = 11.6\ \mu^7 M_c^7 (Z_{CNO})^{1/12} \tag{2.1}$$

where Z_{CNO} is the sum of carbon, nitrogen and oxygen abundances and μ is the mean molecular weight in the envelope (all quantities are expressed in solar units).

The location of the Hayashi line, i.e. the location of the RGB, depends not only on the mass but also on metallicity. Higher-mass stars have higher $T_{\rm eff}$ at the same luminosity and more metal-rich stars with the same mass and L are located at lower $T_{\rm eff}$. Metal-rich stars of a given mass have slightly larger radii and lower effective temperatures than stars of the same mass but lower metallicity. The evolution proceeds towards larger radii and higher luminosities and speeds up as L increases. When stars reach the Tip of the RGB the temperature is high enough for helium ignition in the core, which is degenerate and causes thermonuclear runaway known as *Helium Flash*.

Three main processes characterize the RGB evolution. The first dredge-up (FDU) occurs when the convective envelope penetrates in the deeper layers where H-burning products are present. As a consequence of the mixing, the He surface abundance increases, the H abundance decreases as well as the ratio between Carbon and Nitrogen (C/N). When the H-shell reaches the discontinuity left by the convective envelope, the burning rate slows down leading to a slightly decrease in L, followed by an increase of L after the discontinuity is overcome. The resulting loop in the HRD produces the "bump" in the luminosity functions of old star clusters. During the RGB phase low-mass stars experience significant mass losses at a rate of about $10^{-7} - 10^{-8} M_\odot/yr$. The process is not well understood and the effect of mass-loss is usually included in stellar models by means of empirical or semi-empirical relations. One of the most popular choice is the use of the classical Reimers (1975) law, which contains an adjustable efficiency parameter $\eta_{\rm R}$. More recently, Schröder and Cuntz (2005) proposed a semi-empirical, modified version of Reimers (1975)

law, based on the assumption that the stellar wind originates from magneto-acoustic waves operating below the stellar chromosphere. This relation also contains a fitting parameter η. Low-mass stars can lose up to the 20% of their initial mass and a precise calibration of $\eta_{\rm R}$ or η is necessary to account for the morphology of the Horizontal Branch in Galactic Globular clusters populated by low-mass stars during the helium-burning phase.

2.1.4 The Helium burning phase

The helium burning phase starts when the temperature in the He core reaches $T_c \approx 10^8$ K and the 3α reactions produce energy at a significant rate. The reactions involved are the same for all stellar masses but the conditions in the core at the ignition of He are different in low-mass stars which have a degenerate He core and in more massive stars which have non-degenerate core.

In intermediate-mass stars nuclear burning is thermally stable and since the He-burning reactions are very sensitive to the temperature the energy production is concentrated towards the center, giving rise to a convective core with a mass growing with time. After He ignition at the TRGB, the envelope contracts and the stellar radius decreases. The luminosity also decreases while the envelope is mostly convective and the star moves along its Hayashi line until the envelope becomes mostly radiative and the $T_{\rm eff}$ increases. The star moves away from the RGB and this is the beginning of the "blue loop" in the HRD of intermediate-mass stars. When the loop reaches its hottest point, the stellar radius has a minimum after which the envelope expands and the star moves again towards the RGB. At the end of the He core burning intermediate-mass stars find themselves very close to their Hayashi line. The blue extension of the loops increases with stellar mass. Stars with $M \lesssim 4\ M_\odot$ describe loops which remain very close to the RGB. The occurrence and extension of blue loops depend on metallicity, ratio between He core mass and envelope mass, shape of H abundance profile above the core, convective overshooting.

Low-mass stars ignite helium in a degenerate core giving rise to the helium flash and the helium burning starts with essentially the same core mass $M_c \approx 0.45\ M_\odot$. After the thermonuclear runaway the condition of degeneracy is lifted when the temperature reaches about 3×10^8 K, the further nuclear burning of helium is thermally stable and proceeds in a convective core. The evolution through the helium flash is not calculated for the tracks shown in Figures 2.1 and 2.2. The models are evolved from a Zero Age Horizontal Branch sequence corresponding to the onset of steady He burning in the center. Luminosity and radius have decreased and the core has expanded while the envelope has contracted, with the H-shell acting as a "mirror". The position of the stars in the HRD does not change significantly. The luminosity is determined mainly by the core mass which is approximately the same for all masses, therefore the luminosity at which He burning occurs is almost independent of mass. At fixed composition, only the envelope mass varies from star to star and determine the radius and effective temperature of He burning stars. At solar metallicity, all stars are located in the Red Clump, observed in CMDs of low-mass old stellar populations. However, stars with small envelope mass can be hotter than Red Clump stars and furthermore at low metallicity the critical envelope mass below which stars become small and hotter is larger. He burning stars then form the so called Horizontal Branch in the HRD.

At the end of the He burning phase, a central core composed of carbon and oxygen is formed. The subsequent evolution of low- and intermediate-mass star is qualitatively similar and it will be discussed in detail in the next section.

2.2 The evolution during the AGB phase

When He is exhausted in the center, the carbon-oxygen (C-O) core contracts and He burning occurs in a shell around the C-O core. At this stage the star has two active burning shells, so that the core contraction is followed by the expansion of the He-rich layers above and the outer envelope contracts. However, the expansion of the He-rich zone decreases the temperature in the H-shell that quenches off. Thus, the entire envelope starts expanding and cooling down. The star moves towards lower $T_{\rm eff}$ and higher luminosities and evolve along the Asymptotic Giant Branch (AGB) in the HRD.

The initial phase during which the stellar luminosity is provided almost exclusively by the He-shell burning is the Early AGB (E-AGB) phase. The mass of the C-O core gradually increases until it becomes degenerate. Stars more massive than about 4 $M_\odot$ (the exact value depends on composition and overshooting) can experience a second dredge-up episode. As a consequence of expansion and cooling, the convective envelope can penetrate into the He-rich layers. The continuing expansion and cooling of these layers increases their opacity and the growing energy flux produced by the He-shell allow the deep penetration of the envelope. In lower-mass stars the H-shell remains active and the second dredge-up does not occur. The material which is dredged up and appears at the surface consists mainly of He and ^{14}N. Compared to the RGB FDU it is qualitatively similar but the effect is more dramatic, in fact the dredged up material can be as much as 1 $M_\odot$ in the most massive AGB stars. Furthermore, the occurrence of the second dredge-up reduced the mass of the H-exhausted core, limiting the mass of the white dwarf that remains at the end of the AGB phase.

During this phase the luminosity provided by neutrinos can balance the gravitational energy released by the C-O core contraction. Thus, the density increase becomes more significant than the temperature increase and the strong electron degeneracy stops the core contraction. The He-burning shell rapidly approaches the H-He discontinuity and its luminosity decreases due to the lack of fuel. The layers above respond with a contraction that heats up the extinguished H-burning shell which is finally re-ignited. This is the beginning of the double shell burning phase. The He-shell burning occurs in a thin shell and becomes thermally unstable. This phase is characterised by periodic thermal pulses and it thus referred to as Thermally Pulsing AGB (TP-AGB).

2.2.1 The TP-AGB phase

The schematic evolution of the inner layers of a TP-AGB star during and between two consecutive thermal pulses is shown in Figure 2.3.
The He-shell burning remains inactive for most of the time, while the H-shell burning adds mass to the intershell region until a critical value is reached and the He is ignited. The resulting thermonuclear runaway, called helium shell flash, produces a huge energy flux that drives convection in the whole intershell region, thus producing the intershell convection zone (ICZ). The ICZ mixes the elements produced by He burning, in particular ^{12}C produced by 3α reactions throughout the intershell region. The large energy release by He-shell flash causes the expansion and the cooling of the intershell region leading to quench of the H-shell and allowing a deeper penetration of the outer convective envelope. The material of the intershell region (mainly He and C) is mixed and appears at the surface. This is the third dredge-up and this term is used even for stars that do not experience second dredge-up and for all subsequent dredge-up events. After the third dredge-up, the H-shell is re-ignited while the He-shell is inactive again. During this interpulse period, H-burning adds mass to the intershell until the next thermal pulse. The pulse cycle

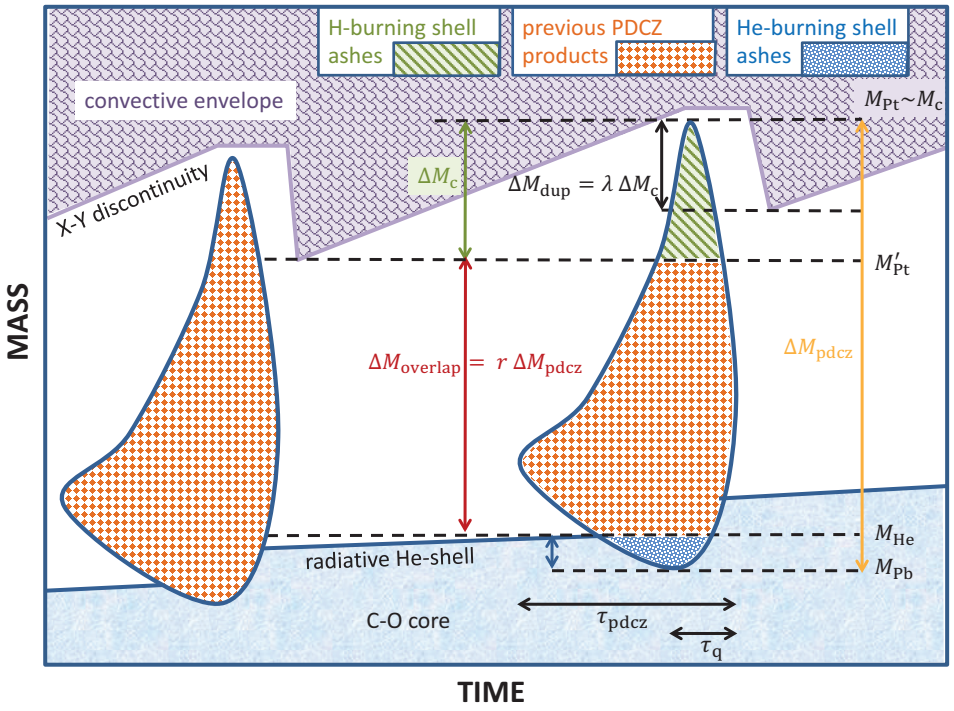

Figure 2.3: Schematic evolution of an AGB star through two consecutive thermal pulses (Marigo et al. 2013).

repeats many times and the amplitude of the pulse increases at each cycle, facilitating the occurrence of the third dredge-up. An important consequence of thermal pulses and third dredge-up is the limitation of the CO core mass growth. A very efficient dredge-up implies that in the long-term the core mass does not increase significantly.

The main effect of thermal pulses and third dredge-up is the photospheric enrichment of carbon. The surface ^{12}C abundance increases at each dredge-up episode until it eventually exceeds the ^{16}O abundance. The ratio between the photospheric abundance of carbon and oxygen (C/O ratio) is a fundamental quantity that determines the spectral features af AGB stars. The low temperature of AGB star atmosphere causes the C and O atoms to be bound into CO molecules. When C/O is less than 1, the remaining O atoms form oxygen-rich molecules, such as Titanium Oxide (TiO) and water (H_2O), as well as dust particles, mainly silicate grains. The spectra of O-rich AGB stars are classified as type M. The repeated dredge-up events make the C/O ratio grater than 1, leading to the formation of carbon-rich molecules (C_2, CN) and carbonaceous grains like graphite. These more evolved stars are classified as carbon stars (spectral type C).

During the interpulse period in stars with M $\gtrsim 4-5$ M$_\odot$, the temperature at the base of the convective envelope can become so high that H-burning through CNO cycle takes place. The main effects of this process, known as Hot-Bottom Burning (HBB), are an increase in the surface luminosity and the conversion of dredged-up ^{12}C into ^{14}N. HBB thus prevents massive AGB stars to become carbon stars and makes them efficient producers of nitrogen. If the HBB is very efficient, the activation of the ON cycle causes the conversion of ^{16}O into ^{14}N and the C/O can become larger than 1.

The efficiency of third dredge-up and HBB depends on several factors, mainly stellar masses and metallicity, which will be discussed in the next section, as well as the complex interplay between the two processes.

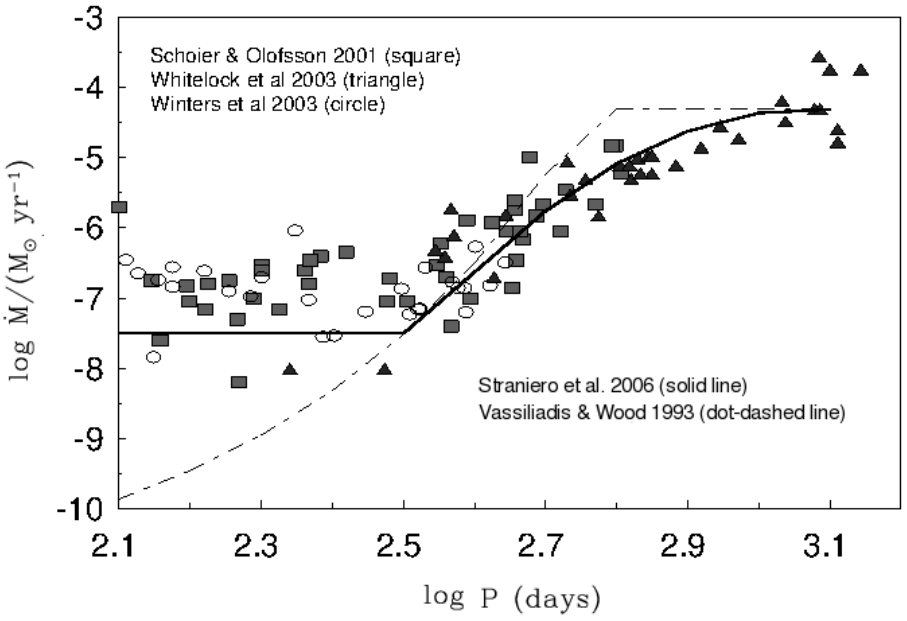

Figure 2.4: Comparison between mass loss rates and periods, as measured by various authors, and prescriptions used in stellar evolution calculations. Mass loss rates and periods for O-rich AGB stars (open circles) are measured by Winters et al. (2003), while C-rich AGB stars data (squares and triangles) are from Schoier & Olofsson (2001) and Whitelock et al. (2003), respectively. The dot-dashed line represents the prescription by Vassiliadis & Wood (2003) and the solid line the prescription by Straniero et al. (2006). Figure adapted from Straniero et al. (2006).

The stellar properties are mainly determined by the mass of the degenerate C-O core, thus similarly to the RGB, there is a relation between core mass and surface luminosity (CMLR; Wagenhuber and Groenewegen (1998)):

$$L = (18160 + 3980\mathrm{Z}_i)(\mathrm{M}_c - 0.4468) + 10^{2.705+1.649\mathrm{M}_c} \tag{2.2}$$

where Z_i is the initial metallicity. This approximate relation holds only during the quiescent interpulse period, while it is violated during the first sub-luminous thermal pulses, in stars with very efficient third dredge-up, and in massive stars experiencing HBB which may become significantly over-luminous compared to what expected for the same core mass.

TP-AGB stars experience strong mass-loss through stellar winds, as clearly demonstrated by their SEDs which show large IR excess. Furthermore many AGB stars, knows as OH/IR stars, are almost completely enshrouded in dusty circumstellar envelopes and are not visible at optical wavelengths. Although the driving mechanism of mass-loss in not yet completely understood, it is widely accepted that it is a two-steps process, involving dynamical pulsations and radiation pressure on dust particles.
Along the AGB, stars evolve towards larger radii and undergo strong radial pulsations. An observational correlation between pulsation period and mass-loss rate exists (see Fig. 2.4): the evolution proceeds with increasing pulsation periods and thus increasing mass-loss rates, from $\dot{\mathrm{M}}$ 10^{-8} $M_\odot/yr$ for Mira variables up to $\dot{\mathrm{M}} \approx 10^{-4}$ $M_\odot/yr$, which is the value typically inferred for dust enshrouded OH/IR stars. This phase of very strong mass-loss is referred to as "superwind" and marks the end of the AGB phase, since when a star enters this phase the H-envelope is rapidly removed.

The basic physical picture is illustrated in Figure 2.5. Radial pulsations induce shock waves in the stellar atmosphere, which bring gas out to larger radii, resulting in an increase of the gas density in the atmosphere. At about 1.5 - 2 stellar radii, the temperature is low enough that dust particle can condense. Optical properties of dust grains depend on their composition, in particular carbonaceous grains are more opaque than silicates, however they are sufficiently opaque to be easily accelerated by the radiation pressure resulting from the high stellar luminosity. Although dust fraction is only about 1% of the gas in the atmosphere, the molecular gas is dragged along by the accelerated dust particles producing a large-scale outflow.

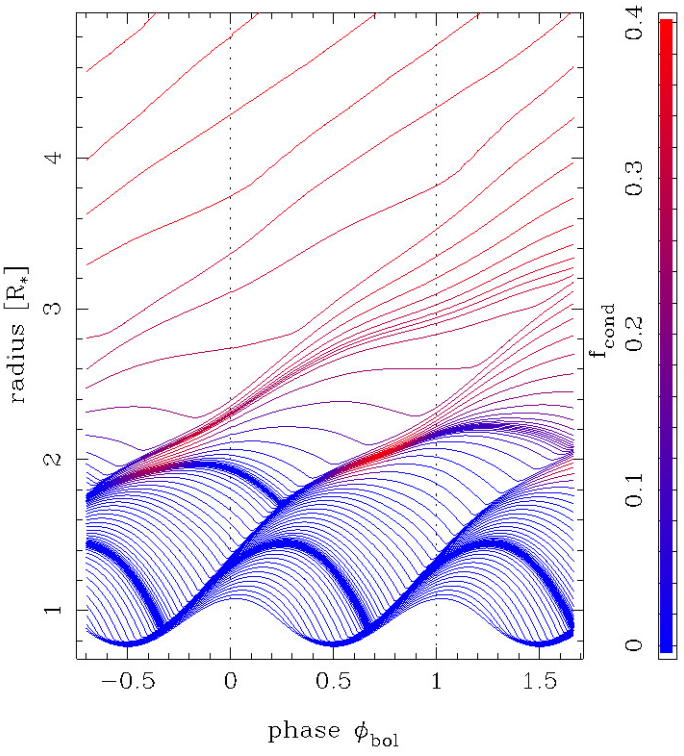

Figure 2.5: Scenario of a pulsation-enhanced dust-driven wind, from Nowotny et al. (2010). The plot illustrates the different regions within the atmosphere of a typical mass-losing LPV. The innermost, dust-free layers below $\approx 2R_\star$ are subject to strictly regular motions caused by the pulsating interior (shock fronts). The dust-forming region (colour-coded is the degree of dust condensation f_c) at $\approx 2-3R_\star$ where the stellar wind is triggered represents dynamically a transition region with moderate velocities, not necessarily periodic. A continuous outflow is found from $\approx 4R_\star$ outwards, where the dust-driven wind is decisive from the dynamic point of view.

An important consequence of mass-loss is the reduction of the stellar lifetimes of the TP-AGB phase: the increasing mass-loss rate causes a rapidly increasing removal of the H-rich envelope. The high mass-loss rate experienced in the super-wind phase determines both the maximum luminosity and the final mass (i.e. the mass of the remaining white-dwarf) of AGB stars. AGB lifetimes are also affected by the third dredge-up and HBB efficiency, which modifies the surface chemical composition, mainly in terms of C/O. The chemical composition controls the atmospheric molecular opacity and the dust grains composition, which in turn influence the mass-loss rate. In general, the transition to carbon star makes the mass-loss rate increase, resulting in a shortening of stellar lifetimes. The second important consequence of mass-loss is the enrichment of Interstellar Medium (ISM)

by AGB ejecta, the composition of which depends again on dredge-up and HBB efficiencies as well as dust formation efficiency. The detailed modelling of TP-AGB phase is thus fundamental for the understanding of several astrophysical aspects, including chemical evolution and SEDs of galaxies, multiple stellar populations in star clusters, interpretation of integrated colors of galaxies in both local and far Universe. A more detailed discussion about the impact of the TP-AGB stars evolution will be given in Section 3.4.

2.2.2 Post-AGB evolution

Once the H-rich envelope is almost completely removed, the envelope shrinks and the stellar radius decrease at almost constant luminosity because the stars follows the CMLR and evolves along a horizontal track in the HRD towards higher $T_{\rm eff}$. This is the post-AGB phase and has a typical timescale of about 10^4 years. The mass of the envelope decreases as a consequence of the H-shell burning at the bottom and the continuing mass loss at the top of the envelope. When the $T_{\rm eff} \approx 3 \times 10^4$ K, a weak but fast wind develops driven by radiation pressure in UV absorption lines and dust grains are destroyed by the strong UV flux. Part of the circumstellar envelopes becomes ionized and the stars appears as a planetary nebula, radiating in recombination lines. Finally, when the mass of the envelope has decreased enough, the H-burning shell is extinguished and the star cools down as a white dwarf.

Chapter 3

TP-AGB modelling and present-day calibration

In order to take into account AGB stars in models of galaxies and in particular the contribution of carbon stars, three major ingredients are necessary. First, evolutionary tracks must be able to provide the distributions of luminosities, effective temperatures and surface compositions of red giants as a function of age, initial mass and metallicity. The stellar models used in this work will be described in Section 3.1. Secondly, synthetic spectra are necessary to allow the conversion of model quantities into observable properties of stars. In Section 3.2 the stellar atmosphere models in use will be presented (Aringer et al. 2009, Loidl et al. 2001; and Aringer et al. in prep.) The last but equally important point is the modelling of the circumstellar reddening by dust, described in Section 3.3.

3.1 Stellar models

In this work, two sets of stellar evolutionary tracks has been used and compared with observational data. The first one corresponds to the evolutionary tracks contained in Girardi et al. (2010; hereafter Gi10), which are basically the tracks described in Marigo and Girardi (2007; hereafter MG07) and Marigo et al. (2008) with some updates. In this case, the evolution prior to the TP-AGB phase, from the PMS up to the first thermal pulse, is taken from Girardi et al. (2000), while the TP-AGB phase is computed through the synthetic code described in MG07, starting from the physical conditions and the first thermal pulse up to the complete loss of the envelope via stellar winds. The second set follows the evolution from the PMS up to the first thermal pulse through the PAdova and TRieste Stellar Evolution Code (`PARSEC`), for which a detailed description is provided by Bressan et al. (2012); the evolution during the TP-AGB phase is then computed by means of the `COLIBRI` code described in Marigo et al. (2013).

3.1.1 The first set of evolutionary tracks

The computation of the evolution prior to the first TP-AGB thermal pulse is taken from Girardi et al. (2000) fot the initial metallicities Z = 0.0004, 0.001, 0.004, 0.008, 0.019, 0.03, and from Girardi (2001, unpublished; see `http://pleiadi.oapd.inaf.it`) for Z = 0.0001. The initial masses of these tracks are between 0.15 and 7 $M_\odot$, (models with $0.5 \lesssim M/M_\odot \lesssim 5$ are considered to undergo the TP-AGB phase).

The semi-analytic code used to compute the evolution during the TP-AGB phase (MG07) takes into account the crucial effects of third dredge up, hot bottom burning over-

luminosity and nucleosynthesis, variations of pulse cycle luminosities and $T_{\rm eff}$, opacity variations caused by changes of the envelope chemical composition, long-period variability and the switching between the first and fundamental overtone along the evolution. Furthermore, the formalism for the mass-loss rate is derived from pulsating dust-driven wind model for C- and O-rich AGB stars. These models consistently predict not only the time evolution on the HRD, but also the surface chemical composition variations, pulsation modes and periods, and mass-loss rates. The uncertain parameters of the models, mainly related to the third dredge-up, are calibrated in order to reproduce the carbon star luminosity functions (CSLF) in the Magellanic Clouds and the C- and M-star counts in Magellanic Cloud clusters. The main improvements of MG07 models over past works are summarized below, with particular attention to those relevant for this study:

- **Luminosity and core-mass growth**. A fundamental ingredient of synthetic models is the core-mass luminosity relation (CMLR), which is usually derived from complete AGB evolutionary calculations and it is strictly valid only before a thermal pulse, i.e. during the quiescent interpulse period. For low-mass models not experiencing the HBB, the adopted CMLR is taken from Wagenhuber and Groenewegen (1998). Models with M > 3.5 - 4.5 $M_{\odot}$ (the precise value depends on the metallicity) experience the HBB and the CMLR needs to be corrected to take into account the resulting over-luminosity. This correction represents an additional term according to Izzard et al. (2004) and takes into account the the increasing degeneracy of the core during the TP-AGB evolution. The adopted formalism allows to follow the detailed evolution of both stellar luminosity L(t) and L_H(t), which is the energy generation rate due to H-burning shell and together with the emitted energy per unit mass of H burnt into He (Q_H) and the H envelope abundance (X_H), it is used to calculate the core mass growth rate:

$$dM_c/dt = L_H(t)Q_H/X_H \tag{3.1}$$

  The growth of the core mass during the interpulse period can undergo a quasi-instantaneous reduction as a consequence of the convective dredge-up and affects the duration of the whole TP-AGB phase. Therefore it is necessary to properly take into account the deviation from the CMLR in order to predict reliable TP-AGB star counts through population synthesis methods.

- **Interpulse period.** The interpulse period τ_{ip} increases in the more massive models as a result of deep dredge-up events and affects the evolution over the quiescent regime, i.e. core mass and luminosity increase, as well as the frequency of dredge-up events themselves. The core mass-interpulse period relation accounting for the τ_{ip} is taken from Izzard et al. (2004), which add a positive term to the Wagenhuber and Groenewegen (1998) relation depending on the dredge-up efficiency λ.

- **Effective temperature.** In synthetic AGB models The effective temperatures ($T_{\rm eff}$) are usually estimated via analytic relations that fit the results of full stellar calculations (e.g., Izzard et al. 2004, Groenewegen and de Jong 1993). In MG07 $T_{\rm eff}$ is derived through a complete integration of static envelope models from the photosphere down to the core. The transition from oxygen-rich to carbon-rich surface composition resulting from the occurrence of the third dredge-up, as well as the inverse transition caused by the HBB, produces drastic opacity changes, which need to be taken into account especially in the treatment of C-stars evolutionary models. The improvement of TP-AGB models from MG07 consists in the calculation

of low-temperature molecular opacities consistently coupled with the actual surface chemical composition. This treatment allow to predict the "red tail of carbon stars" observed in near-infrared color-magnitude diagrams of the MCs (Marigo et al. 2003).

- **Third dredge-up.** The treatment of the third dredge-up is equivalent to the one illustrated in Marigo et al. (1999) and requires three quantity to be specified, which in this case are:

  (i) The minimum core-mass required for the occurrence of the mixing event, M_c^{min}. This value is taken from Karakas et al. (2002) which proposed a relation M_c^{min}(M,Z) based on grids of complete AGB calculations with stellar masses between 1 and 6 $M_\odot$ and metallicities Z = 0.02, 0.008,0.004. However, M_c^{min} has been corrected by MG07 in order to reproduce the CSLF of the MCs and to include the effects of convective overshooting.

  (ii) The third dredge-up efficiency, λ, which is usually expressed by $d\lambda = \delta M_{dred}/\delta M_c$ where M_{dred} is the mass brought up to surface at a thermal pulse and δM_c is the increment of the core mass over the preceding interpulse period. In previous studies the value of λ is chosen to be the same for all stellar masses, while in MG07 this assumption has been relaxed in order to account for both the mass and metallicity dependences found on the base of complete AGB models from Karakas et al. (2002) and Izzard et al. (2004).

  (iii) The chemical composition of the intershell, i.e. the abundances of ^{4}He, C and O as a function of the core mass growth is derived on the base of the nucleosynthesis calculations by Boothroyd and Sackmann (1988b). As shown in Figure 9 in MG07, the fractional mass of C and O rapidly increases during the first pulses up to a maximum value, while the He abundance follow and inverse trend.

- **Hot-bottom burning.** HBB takes place in TP-AGB models with $M \geq 3.5-4.5\ M_\odot$, depending on metallicity, and correspond to the H-burning via the CNO-cycle in the deepest layers of the convective envelopes. The main effects of the HBB, as already described in Section 2.2, are the breaking of the CMLR, the changes in the surface chemical composition which can prevent the formation of C-stars by converting C into N, or in some cases, when the temperature at the base of the convective envelope is high enough to activate the ON cycle, HBB can favour the formation of C-stars. The treatment of the HBB process is the same as in Marigo et al. (1999). Briefly, the element abundances in the envelope models are determined at each time step during the interpulse period by solving a network of nuclear reactions, according to the temperature and density stratifications found by numerical integrations of a complete envelope model. The HBB nucleosynthesis results to be consistently coupled with the structural evolution of the envelope, making the MG07 synthetic models very similar to the complete ones. As en example, the MG07 code allows to naturally predict the temporal evolution of the temperature at the base of the convective envelope, which is directly related to the efficiency of the HBB.

- **Mass-loss rates.** The calculation of mass-loss rates, $\dot{M}$, during the TP-AGB evolution is performed in a different way depending on whether the stellar model is oxygen-rich or carbon-rich.

  For O-rich AGB stars the results of dynamical atmosphere models by Bowen and Willson (1991) are adopted, including dust for long-period variables. Since the results from Bowen and Willson (1991) are only valid for AGB stars pulsating in the

fundamental mode (FM), MG07 estimate the mass-loss rate for stars pulsating in the first overtone (FOM) through a different procedure, fully described in Sec. 2.8.1 of MG07.

For C-rich stars, MG07 distinguished two different regimes of mass-loss. The first is applied to low-luminosity, short-period, high-effective temperature red giants, for which the dominant mechanism of mass-loss is a pulsation driven wind. These stars follow the semi-empirical relation of Schröder et al. (2003) until a critical luminosity is reached. The subsequent regime of mass-loss in fact refers to the development of a dust-driven wind, which requires a minimum luminosity, such that the acceleration provided by radiation pressure on dust grains could overcome the inward gravitational pull. In this case, the values of $\dot{M}$ are derived from the pulsating dust-driven wind models from Winters et al. (2000, 2003).

In both cases, the mass-loss rates depend on the pulsation period, which is computed along the evolutionary tracks following the period-mass-radius relations derived by Ostlie & Cox (1986), Fox & Wood (1982), Wood et al. (1983).

As already mentioned, the MG07 evolutionary tracks have been improved by Gi10 which modified the prescription for the mass-loss rate. The main problem of TP-AGB tracks from MG07 is the duration of TP-AGB phase. Gi10 demonstrate that a reduction of TP-AGB lifetimes up to a factor of 6-7 is necessary to reproduce the observations of a sample of 12 resolved galaxies from the ACS Nearby Galaxy Survey Treasury characterized mainly by low-mass, metal-poor stars ($M \lesssim 1.5\ M_{\odot}$ and [Fe/H] $\lesssim$ -1.0). In these conditions, dust-driven winds might be less efficient with respect to those found in more luminous and cool giants. The prescription for the "pre-dusty" winds, i.e. before the onset of winds driven by radiation pressure on dust grains, is a kind of Reimers (1975) law, taken from Schröder and Cuntz (2005) which estimate the mass-loss rate $\dot{M}_{\text{pre-dust}}$ as follows:

$$\dot{M}_{\text{pre-dust}} = \eta \frac{LR}{M} \left(\frac{T_{eff}}{4000\ K} \right)^{3.5} \left(1 + \frac{g_{\odot}}{4300\ g} \right) \quad [M_{\odot} yr^{-1}] \tag{3.2}$$

where g and $g_{\odot}$ are the stellar and the solar surface gravity respectively while η is a fitting parameter set to $\eta = 0.8 \times 10^{-13}$ and it is calibrated in order to reproduce the morphology of horizontal branches in globular clusters. This relation is used until the minimum mass-loss rate $\dot{M}^{min}_{dust}$ required for the development of a dust-driven wind is reached. $\dot{M}^{min}_{dust}$ is calculated as in Gail and Sedlmayr (1987) and depends on the the opacity contributions from the gas, κ_{gas}, and dust, $\kappa_{dust,i}$ species, as well as the condensation degree of the ith dust species. When the star enters the dust-driven wind phase (as soon as $\dot{M}_{\text{pre-dust}} \geq \dot{M}^{min}_{dust}$), two different formalism has been tested by Gi10. The first one is based on Bowen and Willson (1991) (the same as MG07), but following the suggestion of Willson (2000) to relax the metallicity dependence. The second is based on Bedijn (1988) with a different calibration of the parameters. The use of these two prescriptions for mass-loss leads to a much better description of the data with respect to TP-AGB models from MG07 with an overestimation of the lifetimes by a factor up to 2. In both cases, there is a good agreement between simulations and data, as a result of the shortening of TP-AGB lifetimes derived by the non-negligible "pre-dust" mass-loss rate and by the higher efficiency of dust-driven winds compared to MG07. In addition, the Gi10 code computes, for the first time, the low-temperature opacities on-the-fly by means of the `ÆSOPUS` tool (Marigo and Aringer 2009), avoiding the loss in accuracy due to the interpolation on pre-computed opacity tables.

Furthermore, the Gi10 TP-AGB models naturally recover the initial-final mass relation of population II stars derived by Kalirai et al. (2009).
As already mentioned above, TP-AGB models from Gi10 constitute the first set of evolutionary tracks which will be used in the population synthesis simulations described in Section 5.

3.1.2 Evolutionary tracks from PARSEC & COLIBRI

PARSEC Tracks. The fundamental physical inputs of the PARSEC code are summarised below. The PARSEC code computes the stellar tracks for stars with initial masses between 0.1 and 12 $M_\odot$, with a resolution of 0.05 $M_\odot$ and ∼0.2 $M_\odot$ for low- and intermediate-mass stars respectively. The range of metallicities is from 0.0005 to 0.07.
Solar distribution of heavy elements. For each element heavier than ^{4}He its fractional abundance is assigned relative to the total solar metallicity, i.e. $X_{i,\odot}/Z_\odot$ which is the reference distribution. The reference solar distribution of metals consists of 90 chemical elements, the abundances of which are taken from Grevesse and Sauval (1998) and Caffau et al. (2011). The resulting present-day metallicity of the Sun is $Z_\odot = 0.01524$.
Opacities. The opacity of the stellar matter has been evaluated by means of pre-computed Rosseland mean opacities $\kappa_R(\rho, T)$, thus it depends on temperature and density, but also on the gas chemical composition specified by the X and Y abundances and by the distribution of heavy elements. At high temperature, in the range $4.2 \leq log(T/K) \leq 8.7$, the opacities are those provided by the Opacity Project At Livermore (OPAL) while at lower temperature ($3.2 \leq log(T/K) \leq 4.1$), they have been computed through the ÆSOPUS code. A linear interpolation between the opacities from OPAL and ÆSOPUS has been adopted for the temperature in the transition region $4.1 \leq log(T/K) \leq 4.2$. Two distinct sets of opacity table are generated: the H-rich one and the H-free one (X=0) that describes the opacities for the He-burning regions.
Convection and overshooting. The overshoot across the border of convective regions is described by the parameter Λ_c, which is the mean free-path of fluid elements (mixing length) and it is proportional to the local pressure scale height. The overshoot parameter Λ_c in the convective core is chosen according to the stellar mass in order to describe the transition between radiative and convective cores: $\Lambda_c = 0$ for $M \leq M_{O1}$, Λ_c increases linearly up to $\Lambda_{max} = 0.5$ between $M \leq M_{O1}$ and $M \leq M_{O2}$, $\Lambda_c = \Lambda_{max}$ for $M \geq M \leq M_{O2}$. The values of $M = M_{O1}$ and $M = M_{O2}$ depend on the initial chemical composition. The overshoot efficiency in the convective envelope is tratead as in Alongi et al. (1991) and Bressan et al. (1993), with $\Lambda_e = 0.05$ for $M \leq M_{O1}$ and $\Lambda_e = 0.7$ for $M \geq M_{O1}$, the transition between these two values is smooth.

Recently, the data base of PARSEC tracks has been complemented with new models of massive stars (up to 350 $M_\odot$), from the PMS to the central carbon ignition, covering a broad range of metallicities, $0.0001 \leq Z \leq 0.04$, (Chen et al. 2015).

COLIBRI tracks. The COLIBRI code, fully described in Marigo et al. (2013), is used to compute stellar models starting from the first thermal pulse until the almost complete loss of the envelope by stellar winds. The initial conditions for each stellar model with initial parameters (M_i,Z_i) at the first thermal pulse (core-mass, luminosity, effective temperature, envelope chemical composition) are taken from the the PARSEC data base. The COLIBRI code represents a fundamental step-forward in the development of envelope-based TP-AGB models (MG07) and the numerous improvements implemented make it perform much more like an "almost-full" model rather than an "improved synthetic" one. The robust numerical

stability and the high computational speed of the code allow to perform a multiparametric and accurate calibration of the TP-AGB phase. COLIBRI maintains a few basic feature of the TP-AGB models developed by MG07, but contains fundamental improvements that enhance its predictive power with respect to MG07 and Gi10 evolutionary tracks, as already shown by Marigo et al. (2013) and confirmed by this work (see Section 5.2).

With respect to purely-synthetic TP-AGB models, COLIBRI relaxes a significant part of the analytic formalism in favour of detailed physics applied to complete envelope models, integrated from the atmosphere down to the H-burning shell. A direct consequence of this approach is the possibility to follow the basic changes in the envelope and both the energetics and nucleosynthesis of the HBB with a level of accuracy than can even go beyond the accuracy of full models.

In the following, a brief summary of the COLIBRI features is presented, while the reader should refer to Marigo et al. (2013) for a detailed description of all input physics and the solutions method adopted, as well as the analytic relations of COLIBRI.

- **Opacities.** One of the most important feature is the accurate *on-the-fly* computation of the equation of state for roughly 800 atoms and molecular species, as well as the Rosseland mean opacities throughout the atmosphere and the deep envelope. This has been obtained by the inclusion of the ÆSOPUS code (Marigo and Aringer 2009) for $3.2 \leq \log T \leq 4.2$ and the *Opacity Project* (OP) code (Badnell et al. 2005, Seaton 2005) for $4.2 \leq \log T \leq 8$, as internal routines in COLIBRI. This technique allows in particular to follow in detail the evolution of the surface C/O ratio which is fundamental because of the dramatic impact on molecular chemistry, opacity, effective temperature resulting from the transition between C-rich and O-rich composition, as well as for the chemical and physical properties of the dust, as described in Sec. 3.3 and 5.2.

- **Hot Bottom Burning.** Another substantial improvement is related to the description of the HBB process which is described by coupling a complete nuclear network with a time-dependent diffusion scheme for convection. This approach allows to treat the lithium nucleosynthesis in intermediate-mass AGB stars with HBB. In the case of ^{7}Li and ^{7}Be nuclei, the usual approximation of *instantaneous mixing* in the whole convective envelope is no longer valid and ^{7}Li nucleosynthesis follows the *Cameron-Fowler beryllium transport mechanism*: in the outermost layers ^{7}Li is efficiently produced and sustained by electron captures on ^{7}Be nuclei until the reservoir of ^{3}He is exhausted or HBB is extinguished due to envelope ejection by stellar winds. In addition, COLIBRI allows to computed the nucleosynthesis of CNO, NeNa and MgAl cycles which is of particular interest in the context of multiple stellar populations in globular clusters. In the so-called self-enrichment scenario, the HBB nucleosynthesis in metal-poor AGB stars could explain the anticorrelations (CN, ONa, MgAl) observed in galactic globular clusters. COLIBRI gives the possibility to investigate the chemical yields of low metallicity AGB stars and put important constraints on the different scenarios of origin of multiple stellar populations.

- **Third dredge-up.** The occurrence of the third dredge-up as a function of current mass and composition is established by following the same approach as in MG07. However, Marigo et al. (2013) replaced the use of the parameter M_c^{min}, i.e. minimum core mass, with T_{dup} which is the minimum temperature that the envelope base must exceed to activate the third dredge-up. Since the determination of the temperature T_{dup} (or equivalently the M_c^{min} parameter) and the third dredge-up efficiency parameter λ is affected by large theoretical uncertainties, the approach used in COLIBRI is

to treat them as free parameters and to calibrate them with the largest possible set of observations.

- **Pulse-driven nucleosynthesis.** The chemical composition of the dredged-up material, mainly in terms of ^{4}He, ^{12}C, ^{16}O, ^{22}Ne and ^{23}Na, is predicted by means of a full nuclear network, which includes the triple-α reaction and the most important α-captures reactions, applied to a simple model for the evolution Pulse-Driven Convection Zone (PDCZ) (see Fig. 2.3).

- **Mass-loss rates.** The mass-loss rates are determined following the same approach as in Gi10. As long as pulsation-driven wind is the dominant mechanism of mass-loss, the semi-empirical relation by Schröder and Cuntz (2005) is adopted. The dust-driven wins regime is treated as in Gi10 and follows the approach of Bedijn (1988). The mass-loss rate is then assumed to be a function of basic stellar parameters (mass M and radius R) and is expressed by $\dot{M} = e^{M^a R^b}$. The free parameter a and b have been calibrated on a sample of Galactic LPVs with measured mass-loss rates, pulsation periods, stellar masses, radii and effective temperatures. This formalism predicts an exponential increas of mass-loss rates during the TP-AGB evolution until typical values of super-winds, described as in Vassiliadis and Wood (1993) are reached ($\sim 10^{-5} - 10^{-4}\ M_{\odot}/yr$).

The evolutionary tracks from the `PARSEC` code coupled with those computed by means of the `COLIBRI` code constitute the second set of evolutionary tracks used in this work. At each calibration step, for each selected combination of free parameters, to obtain a complete grid of stellar evolution models that cover a large range of metallicities, from very low to super-solar values, we need to compute ≈ 1000 TP-AGB tracks in the domain of low- and intermediate-mass stars. New grids of TP-AGB tracks need to be computed every time an input prescription is changed. The `COLIBRI` turns out to be suitable tool to carry out this kind of demanding procedure.

3.2 Stellar atmospheres models and bolometric corrections

In order to directly compare the predictions of stellar models with observations, one of the fundamental steps is the construction of an assembly of spectral fluxes, covering wide enough ranges of initial metallicities, effective temperatures and surface gravity values, which allow the conversion from model predicted quantities (luminosity, effective temperature) to observed quantities (magnitudes and colors).

Evolutionary tracks obtained by stellar model calculations must be transformed into isochrones, which in turn must be converted to the photometric system of interest by means of the appropriate bolometric corrections. This procedure is described in Marigo et al. (2008) for isochrones computed from MG07 evolutionary tracks. They presented a large set of theoretical isochrones which have been converted to about 20 different photometric systems using synthetic photometry applied to an updated library of stellar spectra. Given the spectral flux at the stellar surface, bolometric corrections for any set of filter transmission curves are calculated following the approach of Girardi et al. 2002. The library of stellar spectra is in constant updating, in particular synthetic spectra for cool evolved stars have been derived and included in the more recent version of the TRILEGAL code.

The sets of bolometric corrections adopted in this work are based on different library of stellar spectra according to the spectral type and surface temperature:

- **"Hot stars".** The term "hot stars" refers to stars with effective temperature larger than about 4000 K. In this case, the bolometric corrections are based on stellar atmospheres models computed with the ATLAS9 code and the new Opacity Distribution Functions (ODFNEW; Castelli & Kurucz 2003). The model grids cover a temperature range between $3500 - 50000$ K and are computed for metallicities $[M/H] = 0.0, -0.5, -1.0, -1.5, -2.0, -2.5, 0.5, 0.2$ and for gravity values from $\log g = 0.0$ to $\log g = +5.0$ in steps of $+0.5$.

- **Cool C-rich giants.** Two different libraries of carbon star spectra are adopted and tested in this work. The first one includes C-star spectra from Loidl et al. (2001), as in Marigo et al. (2008). These spectra, derived from hydrostatic model atmospheres computed with MARCS code (Hofner et al. 2003), cover a temperature range of $2600 \leq (T_{\rm eff}/K) \leq 3600$, they are computed for C/O = 1.1 for all $T_{\rm eff}$ and for C/O = 1.4 for $T_{\rm eff} \leq 3200$ K and only for the solar metallicity. Furthermore, they extend only to the mid-IR wavelengths, i.e. 2.5 μm. The second library includes C-star spectra from Aringer et al. (2009; hereafter A09), which have produced hydrostatic atmosphere models with the COMARCS code, covering a range of $T_{\rm eff}$ between 2400 and 4000 K, surface gravities from $\log g = 0.0$ to $\log g = -1.0$, metallicities from $Z_\odot$ to 1/10 $Z_\odot$ and C/O ratios from 1.05 up to 5.0.

- **Cool O-rich giants.** The library of stellar spectra has been derived from COMARCS atmosphere models (Aringer et. al in prep.) covering the same ranges of effective temperature, metallicities, gravity and C/O ratio values as in A09.

All of the bolometric corrections for cool giants are derived from hydrostatic model atmospheres which do not take into account neither the influence of dynamical processes, such as pulsation and mass-loss, nor the reddening due to circumstellar dusty envelopes. As a direct consequence, these models fail to reproduce the "tail" of extreme AGB stars in the Magellanic Clouds. This feature is instead reproduced when the bolometric corrections include the dust effect. However, C-star bolometric corrections based on A09 atmosphere model results to be one of the fundamental improvement since the work of Marigo et al. (2008).

3.3 Radiative transfer calculations across dusty envelopes

The general effect of dust is to shift part of the intrinsic emitted power of a source from the optical-ultraviolet to the mid- and far- infrared region of the spectrum. Moreover, the envelopes of AGB stars are considered to be one of the two main producers of interstellar grains together with supernoavae explosions. Taking into account the effects of reprocessing of photospheric radiation by dusty Circumstellar Envelopes (CSEs) of cool giants is fundamental to succeed in reproducing the photometric properties of redder and cooler AGB stars.

The determination of the optical properties of dust, i.e. the efficiency of absorption and scattering as a function of wavelengths, which basically depends on dust composition and grain size distribution, results to be a very complex issue for AGB envelopes. First of all, composition and grain size are expected to be very different from the ones present in the Insterstellar Medium. Furthermore, the strong mass-loss experienced by AGB stars is also

dependent on the dust composition. The overall picture is that despite the observational and theoretical progress, the dust formation and evolution in AGB stars is still affected by large uncertainties.

In this work, three different sets of dust bolometric corrections based on different approaches for the circumstellar dust treatment are used to simulate the SMC photometry, with the aim of comparing them and providing indications for their calibration.

The first two sets of bolometric corrections are the same as in Marigo et al. (2008) and has been derived from two indipedent radiative transfer calculations, based on Groenewegen (2006; hereafter G06) and Bressan et al. (1998; hereafter B98) respectively. These models are calculated with 1-dimendional code that solve the radiative transfer equation and the thermal balance equation in a self-consistent way.

The most important difference between B98 and G06 is the adopted dust composition and the coverage of stellar parameters. For G06 calculations, the adopted dust composition is (1) 100% Aluminium Oxide (AlOx) (2) a combination of 60% AlOx and 40% silicates (3) 100% silicates, for O-rich stars, whereas for C-rich stars two kinds of dust are considered: (1) a combination of 85% Amorphous Carbon (AMC) and 15% Silicon Carbide (SiC) (2) 100% AMC. For B98, the dust composition is carbon for C-rich stars and silicates for O-rich stars. For a detailed description of the models, the reader should refer to the respective papers, while the detailed procedure to include the dust effect in the isochrones is described in Marigo et al. (2008).

The third set of bolometric corrections is based on the new model for condensation and growth of dust grains developed by Nanni et al. (2013) and Nanni et al. (in prep.; hereafter N15). N15 adopted a formalism of dust growth coupled with a stationary wind for both O-rich and C-rich stars. For O-rich stars, they considered the evolution of corundum (Al_2O_3), quartz (SiO_2), iron, olivine and pyroxene, whereas for C-rich stars amorphous carbon (AMC), silicon carbide (SiC) and iron are considered. In this model, dust formation in CSEs of AGB stars is assumed to be a two-step process. First, the more stable compounds (seed nuclei) form from the starting molecules, then the accretion proceeds by adding other molecules on the surface of the seed nuclei. The process of dust growth can trigger a dust-driven wind if the radiation pressure of the photons onto the dust grains overcomes the gravitational pull of the star. This dust formation model requires as input the characteristic stellar parameters, such as the mass-loss rate, the luminosity, effective temperature, the actual stellar mass, and the atmospheric gas abundances, including the C/O ratio. For each combination of these input quantities, the outcome of the model characterizes the proprierties of the dust produced in the CSE in terms of chemistry, dust relative abundances, dust condensation fractions, grain sizes, condensation temperatures. Other relevant outputs concern the outflow dynamics, in particular the outflow expansion velocity.

Differently from the previously adopted sets of models, some important quantities such as, the dust composition, its optical properties and so on, are self-consistently computed. It is worth noticing that the outcome of the dust formation model is dependent on the combination of the adopted stellar parameters. The dust formation model is coupled with the radiative transfer code MoD (More of Dusty) developed Groenewegen (2012) which is based on DUSTY by Ivezic et al. (1999). In particular, some of the outputs of the dust formation code, such as a) the optical depth at a given wavelength , b) the dust condensation temperature, c) the dust optical proprierties (dependent of the dust composition) d) the stellar photospheric spectrum, are employed as input parameters for the radiative transfer calculation for each CSEs.

3.4 Calibration of the TP-AGB phase

TP-AGB stars contribute significantly to the total luminosity of a single stellar population, with a peak of about 40% at ages between ≈ 1 and ≈ 3 Gyr. Since their luminosities peak in the near-IR and circumstellar dust emits at mid- to far-IR wavelengths, TP-AGB stars account for most of the infrared-bright objects in resolved galaxies, as demonstrated in the Magellanic Clouds (Boyer et al. 2011, Frogel et al. 1990).

Despite its importance in our understanding of galaxy evolution, the TP-AGB modelling is still affected by large uncertainties due to the presence of several and interconnected processes (third dredge-up, hot bottom burning, stellar winds, long period pulsations, reprocessing of radiation by circumstellar dust in mass-losing stars), for which a robust theory is still lacking, though promising steps have been made (Marigo et al. 2013, Herwig 2005, Karakas and Lattanzio 2014).

3.4.1 Population synthesis models and classical TP-AGB calibrators

The derivation and evolution of spectro-photometric properties of star clusters and galaxies is performed by means of Evolutionary Population Synthesis models (EPS) which are based on stellar evolution theory and predict the integrated properties of an object by adding up the contributions of the individual model stars after assuming an initial mass function (IMF) and a SFH.

There are basically two different techniques to include post-main sequence evolutionary phases, and in particular AGB stars, in EPS models, which are based on: (A) stellar tracks or isochrones and (B) the fuel consumption theorem (Renzini and Buzzoni 1986). Method (A) relies on the adopted stellar models and hence is affected by stellar evolution uncertainties, but allowing a direct comparison between predictions and observations it provides useful feedback of uncertain parameters. Method (B) makes use of empirical calibration of the nuclear fuel based on observed data and can accounts for the correct integrated light contribution of stellar populations, but cannot provide explicit feedback as in model (A). Futhermore, while the resolution element of method (B) is the single stellar population, so that it can be used only for the derivation of integrated properties of unresolved AGB stars, for method (A) the resolution element is the single star and it can predict both resolved and unresolved properties of stellar populations.

The importance of including TP-AGB stars in stellar population synthesis model has been recognized after Maraston (2005) demonstrated that the mass-to-light ratios for old stellar populations (0.5 - 2 Gyrs) can be greatly altered by the presence of TP-AGB stars and this translates into discrepancies in the determination of stellar masses and ages of high-redshift galaxies by factors 2 or more.

Since the work of Maraston (2005), the numerous calibration efforts of the TP-AGB phase as a function of age have been mainly based on star counts, integrated fluxes and spectral classification of Magellanic Clouds (MC) clusters. Such a calibration is limited by the low number statistics of TP-AGB stars (typically $\lesssim$5-10 per cluster) hence affected by large Poisson fluctuations, and by the narrow sampling of the age-metallicity plane. In addition, the age determination of most star clusters is uncertain and the presence of multiple stellar populations in clusters has been neglected in previous analysis.

Due to this limitations, present-day TP-AGB models applied to external galaxies overestimate to various extents the TP-AGB contribution in integrated spectra of galaxies and star counts, hence the need of enhancing the classical calibration by the inclusion of other key properties of TP-AGB stars, such as pulsation periods and surface chemical abundances, and move beyond the MCs clusters to extend the metallicity sampling.

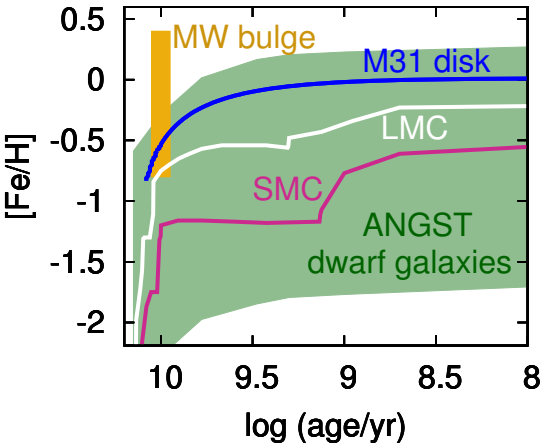

Figure 3.1: The relevant area in the age-metallicity plane that needs to be covered for a reliable TP-AGB calibration. In addition to the MCs, it includes M31 from PATH data, ANGST dwarf galaxies and Galactic Bulge from OGLE and WISE data.

This has become feasible thanks to the excellent data from the new generation of large imaging and spectroscopic surveys of nearby galaxies, which allow to improve the exploitation of MC data through the detailed and spatially resolved SFH for fields and clusters and to extend the metallicity range of the calibration. Figure 3.1 shows the relevant area in the age-metallicity plane that needs to be covered for a reliable calibration of the TP-AGB phase. In addition to the MCs, it includes data of M31 from the Panchromatic Hubble Andromeda Treasury (PATH) survey), ANGST dwarf galaxies and the Galactic Bulge from both the Optical Gravitational Lensing Experiment (OGLE) and the Widefield Infrared Survey Explorer (WISE).

3.4.2 Present and future TP-AGB calibration

One of the critical quantity that needs to be calibrated as a function of stellar mass and metallicity is the lifetime of the TP-AGB phase. Estimating the duration of the TP-AGB phase, $\tau_{\rm TP-AGB}$ is extremely important for two main reasons. First, the energy output of a TP-AGB star, $\rm E_{TP-AGB}$, hence its contribution to the integrated light of the host system, is controlled by its lifetime: $\rm E_{TP-AGB} \propto \int_0^{\tau_{TP-AGB}} \mathit{L}(\mathit{t})\,dt$. Second, the TP-AGB lifetime establishes the number of thermal pulses during the phase, hence the surface chemical enrichment due to mixing episodes, which in turn affects the ejecta of the stars and ultimately the ISM enrichment.

All recent works show a qualitative agreement in predicting a relation between $\tau_{\rm TP-AGB}$ and initial stellar mass that peaks at about $M_{initial} \approx 2\rm M_{\odot}$. This value is close to the critical mass required for the development of a degenerate He-core at the end of the main sequence and corresponds to the mininum core-mass required for the onset of thermal pulses. The interplay between several factors, i.e. core mass at first TP, evolution of the surface C/O, mass-loss, produce the non monotonic dependence of $\tau_{\rm TP-AGB}$ on the initial metallicity. The main parameter that directly controls TP-AGB lifetimes is the efficiency of mass-loss, which may vary with the metallicity.

With regard to TP-AGB models adopted in this thesis, those from MG07 have been calibrated in order to reproduce the carbon star luminosity functions in both MCs and the star counts in MCs clusters. As demonstrated by Gi10, these tracks over-predict of % 40 on

average the TP-AGB star counts in a sample of nearby galaxies observed with ANGST. Following the analysis of Gi10 the main problem of MG07 tracks is the overestimation of TP-AGB lifetimes due to the underestimation of mass-loss rates for low-mass, low-metallicity TP-AGB stars (see Sect. 3.1.1).

More recently, Rosenfield et al. (2014) analyzed star counts and luminosity functions of TP-AGB stars in six quiescent, low metallicity ([Fe/H] $\leq$ - 0.86) galaxies taken from the ANGST sample. They confirmed the importance of pre-dust mass loss and that the third dredge-up has no significant effects on lifetimes of low-mass, low-metallicity TP-AGB stars. The best-fitting mass-loss prescription from Rosenfield et al. (2014) has been adopted in the more recent version of the `COLIBRI` code.

The main purpose of this work is to provide a starting point for extending the calibration of the TP-AGB models from Marigo et al. (2013), based on star counts and luminosity functions of resolved TP-AGB stars in the SMC taken from the SAGE-SMC survey. A full description of both the photometric data and the SFH adopted in the population synthesis simulations will be given in the next chapter.

Chapter 4

Resolved AGB stars in the Small Magellanic Cloud

In this chapter, we will discuss the two datasets that are essential for the present work: the database that contains all information about the bulk of TP-AGB stars in the SMC, namely the SAGE-SMC survey, and the space-resolved SFH (and geometry) across the SMC galaxy as derived from VMC survey data by Rubele et al. (2015). These datasets allow the computations and data-model comparisons that will be described in the next chapter.

4.1 The SAGE-SMC Survey

The *Spitzer Space Telescope* Legacy program entitled "Surveying the Agents of Galaxy Evolution in the Tidally Stripped, Low Metallicity Small Magellanic Cloud" (SAGE-SMC; Gordon et al. (2011)) has provided a complete photometric survey of the evolved star populations in the SMC. The SAGE-SMC catalog includes optical to far-IR photometry, in particular UBVI photometry from the Magellanic Cloud Photometric Survey (MCPS), JHKs photometry from Two Micron All Sky Survey (2MASS) and the InfraRed Survey Facility (IRSF), mid-IR photometry from Spitzer's IRAC, far-IR photometry from MIPS. Its spatial coverage includes SMC bar, wing and tail regions and allows to examine the structure of SMC using the distribution of evolved stars.

In a recent study carried out by Boyer et al. (2011), SAGE-SMC photometry has been used to perform a stellar classification of cool evolved stars in SMC based on color-magnitude cuts in the CMDs. The photometry presented in Boyer et al. (2011) is a co-addition of two epochs of SAGE-SMC data, together with a third epoch from the *Spitzer* Survey of the SMC (S^3MC) where the coverage overlaps. Photometric errors are generally $\lesssim 0.1$ mag for all wavelengths, but for the faintest magnitude (≈ 2 mag) they are $\lesssim 0.2$ mag. Figure 4.1 shows the spatial coverage of each survey included in the SAGE-SMC catalog and the brightest 3.6μm point-sources are plotted for reference. The level of foreground and background contamination has been estimated using the data in a 1.6 deg^2 region of the eastern edge of SMC. From the black dashed box shown in Figure 4.1 a back-/foreground J - [8] versus 8μm absolute magnitude (M_8) CMD was created and subtracted from the full SMC (J - [8], M_8) CMD, giving a residual CMD which is dominated by RGB, Red Super Giant (RSG) and AGB stars, with features from OB stars and Young Stellar Objects (YSOs). The next sections describe in detail the selection criteria, the sources of contamination in the sample and the detection statistics.

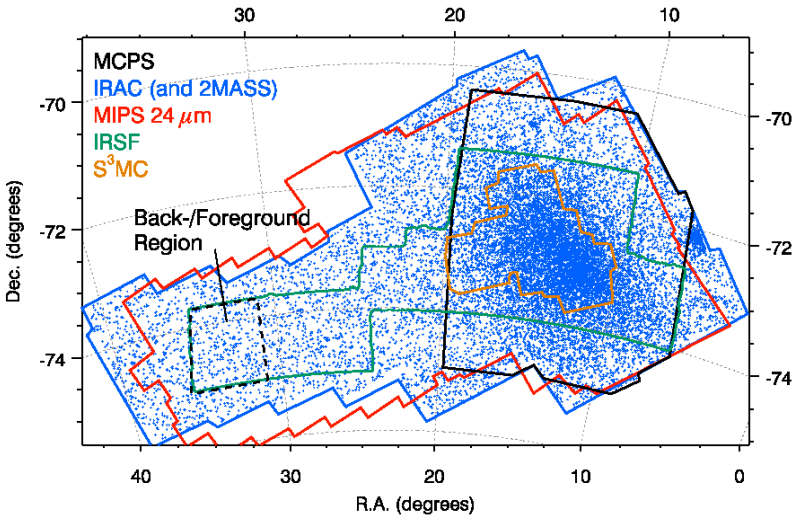

Figure 4.1: Coverage of the SAGE-SMC survey (Boyer et al. 2011). MCPS coverage is shown in black, IRAC and 2MASS in blue, MIPS 24μm in red, IRSF in green and S^{3}MC in orange. The sources plotted in blue are the brightest 3.6μm point-sources and the box with dashed black line is the region used to estimate the background and foreground contamination.

4.2 Classification criteria

The classification scheme adopted by Boyer et al. (2011) separates SMC stars in Red Giant Branch (RGB), Red SuperGiant (RSG), Carbon-rich AGB (C-AGB), Oxygen-rich AGB (O-AGB), anomalous Oxygen-rich AGB (aO-AGB) and extreme AGB (x-AGB). C-AGB and O-AGB stars are selected using color-magnitude cuts in the J - Ks vs. Ks CMD, following the same approach of Cioni et al. (2006) for the Large Magellanic Cloud (LMC). The adopted values of metallicity and distance of the SMC are Z $_{\rm SMC}$ = 0.2 Z$_\odot$ and d$_{\rm SMC}$ = 61 Kpc. All C-AGB and O-AGB stars are brighter than K0 line, defined as:

$$\mathrm{K0} = -0.48 \times (\mathrm{J} - \mathrm{Ks}) + 13.022 + 0.056[\mathrm{M/H}] \tag{4.1}$$

where the value of the metallicity is [M/H] = log(Z$_{\rm SMC}$/Z$_\odot$) = -0.699. K0 line has been shifted towards fainter magnitude to account for the difference in Ks band Tip of the RGB (TRGB) between the SMC and the LMC. Cioni et al. (2006) define other two lines which mark the separation between C- and O-AGB stars:

$$\mathrm{K1} = -13.333 \times (\mathrm{J} - \mathrm{Ks}) + 25.293 + 1.568[\mathrm{M/H}] \tag{4.2}$$

$$\mathrm{K2} = -13.333 \times (\mathrm{J} - \mathrm{Ks}) + 29.026 + 1.568[\mathrm{M/H}] \tag{4.3}$$

C-AGB stars have Ks > K2 while O-AGB stars are defined by K1 < Ks < K2. Furthermore, from the AGB sample Boyer et al. (2011) exclude stars fainter than both Ks-band and 3.6μm TRGB, estimated to be 12.7 mag and 12.6 mag respectively. In this way, RGB contamination is avoided and considering the TRGB at these two wavelengths allows to include also very extinguished AGB stars which can be fainter then Ks TRGB.

The class of the most redder AGB stars is denoted as extreme AGB (x-AGB). These stars are probably in the "superwind" phase with a mass-loss rate which can increase by a factor of 10 and they are obscured at optical wavelengths by a thick dust envelope. In

this case, dust extinction makes necessary the use of mid-IR photometry and x-AGB stars are selected as follows: (1) They are brighter than 3.6μm TRGB and J - [3.6] > 3.1 mag (2) The most dust-enshrouded ones with no near-IR detection, must satisfy [3.6] - [8] > 0.8 mag and [3.6] < 3.6μm TRGB.

Two additional criteria allow to minimize the contamination from YSOs and unresolved background galaxies: x-AGB stars must be brighter than the two lines defined in equations 4.4 and 4.5 in the (J - [8], [8]) and ([3.6] - [8], [8]) CMDs respectively.

$$[8] = 12 - (0.43 \times (J - [8])) \tag{4.4}$$

$$\begin{aligned} [8] &= 11.5 - 1.33 \times ([3.6] - [8]) \text{ if } ([3.6] - [8]) < 3 \\ [8] &= \text{constant} \qquad\qquad\qquad\quad \text{if } ([3.6] - [8]) > 3 \end{aligned} \tag{4.5}$$

RGB stars are affected by both foreground and background and YSOs contamination and the sample is not complete due to the limited sensitivity. Stars within a box spanning from (TRGB + 0.1 mag) < Ks < (TRGB + 3 mag) are classified as RGB and from this sample are excluded sources redder than the following line in the (J - [8], [8]) CMD:

$$[8] = A - (11.76 \times (J - [8])), \tag{4.6}$$

where A = 30.29.

The classification criteria adopted for selecting the RSG stars are as follows: (1) RSG stars are bluer than K1 line and to minimize the contamination from O-AGB stars the RSG branch width is restricted to $\triangle(J - Ks) = 0.2$ mag and a gap of 0.05 mag is left between RSG and O-AGB stars (2) To minimize foreground sources and RGB stars contamination RSG stars have Ks > Ks-TRGB.

Far-IR (FIR) objects include unresolved background galaxies, compact HII regions, planetary nebulae (PNe), YSOs and they are characterised by a SED rising from 8 to 24 μm. 57 FIR objects fall within the photometric selection criteria of AGB and RSG, especially among O-AGB and x-AGB samples and they have been considered in the separate category of FIR.

4.2.1 Anomalous AGB stars

Boyer et al. (2011) identified a new feature in the (J - [8], [8]) CMD suggesting the presence of a class of stars distinct from C- and O-AGB. They referred to these stars as anomalous Oxygen stars (aO-AGB), as they have been originally classified as O-rich by Cioni et al. (2006). These stars were selected from the original O-AGB sample if they are redder than the line defined in Eq. 4.6, with A = 27.95, and fainter than 8μm absolute magnitude, M_8= -8.3 mag; they were selected from the original C-AGB sample if they are bluer than the line defined by Eq. 4.6 with A = 31.47.

In a more recent work, Boyer et al. (2015) carried out a detailed analysis of chemistry, pulsation properties, stellar parameters and dust production of these stars and concluded that they are low-mass dusty AGB stars at the very end of their evolution, with median current stellar mass of about 0.94 $M_\odot$ and initial mass M < 1.25 $M_\odot$. The spectral classification has been performed for a sample of 273 aO-AGB stars in the SMC and results in 122 C-rich, 100 O-rich, 23 S-type and 28 unknown spectra. Since a high fraction ($\sim$ 45%) of the aO-AGB stars turned out to be C-rich, Boyer et al. (2015) refer to aO-stars simply as a-AGB stars. Their results suggest that a-AGB stars should be photometrically selected using the J - 8μm color, which is more reliable with respect to J - Ks color for the most evolved stars.

Since from the theoretical point of view the existence of AGB stars with parameters that correspond to those of a-AGB stars is expected, this new class has only an "observational" meaning, in the sense that its identification will be very useful when the classification criteria of a stellar population are only based on photometric data. The reader should refer to Section 5.3 for all the details concerning the star counts and selection criteria of the a-AGB stars in the simulated photometric catalogs.

4.3 Contamination and detection statistics

The contamination from foreground and background sources which is spatially uniform has been taken into account by the subtraction of the fore-/back-ground CMD from the full one. The level of contamination has been statistically estimated by considering the point-source density in the background/foreground region, which is 1.5×10^4 sources deg^{-2} and the size of the IRAC spatial coverage (≈ 30 deg^2). Boyer et al. (2011) expect contamination to account for 35%, 18% and 2.5% of RSG, RGB and O-AGB samples respectively, while the other types of AGB stars suffer from very low contamination, not being detected in the background/foreground region. As pointed out by the authors, many of the contaminating sources are bluer and/or fainter than the majority of cool evolved stars in the sample and therefore not included in the selection criteria, resulting in an overestimation of the contamination. Two additional sources of contamination are present, i.e. stars belonging to the foreground globular clusters 47 Tucanae and NGC 362 which have near-IR colors very similar to the SMC ones. In order to minimize this contamination, stars within $8'$ and $5'$ of the centers of 47 Tucanae and NGC 362 respectively has been excluded, which implies the elimination of 120 stars from the RGB sample, 108 stars from the RSG sample, 4 from the O-AGB and 1 from the C-rich samples.

Having applied the selection criteria described above and separated the FIR objects from the AGB sample, there is still a remaining contamination from YSOs, HII compact regions, unresolved background galaxies, but all of these contribution are expected to be low. Besides this, the photometric cuts separating C-AGB from O-AGB stars are approximate and a cross-contamination between the two samples is possible. Boyer et al. (2011) analysed this issue by comparing the infrared color-color diagrams (CCD) of the evolved stars in SMC with CCDs presented in the literature. IR colors are very useful to distinguish between cool evolved stars and to investigate dust properties in a large stellar population, especially when IR spectra are not available. The detailed discussion is presented in section 4.1 and 4.3 of Boyer et al. (2011), in which they conclude that their classification scheme reproduce the CCDs showing the separation of spectroscopically confirmed C-rich and O-rich dust-enshrouded sources (Lagadec et al. 2007); their CCDs are quite similar to those presented by Groenewegen2009 and Kastner2008; by comparing the CCDS with those presented by Sloan, which showed the separation of spectroscopically confirmed O-rich and C-rich stars, they concluded that the majority of x-AGB stars are carbon-rich and aO-AGB are dominated by O-rich chemistry.

The more relevant information about the detection statistics are summarized in Table 4.1, which provides the number of sources and the number of sources with 24 μm counterparts for each class of stars in the SAGE-SMC catalog and in Table 4.2 in which the percentage of AGB stars in the SMC is shown.

The near-IR and mid-IR photometric criteria led to the classification of 2 478 O-AGB, 1 729 C-AGB, 349 x-AGB and 1 244 aO-AGB stars, which represent the complete census of AGB stars in the SMC. In this work, infrared CMDs obtained from the SAGE-SMC catalog will be compared to the simulated CMDs in order to test the TP-AGB models with

Table 4.1: SAGE-SMC Source Statistics from Boyer et al. (2011).

Population	N	N_{24}[a]
Point-sources in both J and [3.6]	458 558	9 793
Point-sources with [3.6] < $TRGB_{[3.6]}$	19 290	3 878
C-AGB stars	1 729 (54)	964 (4)
O-AGB stars	2 478 (1 190)	249 (113)
x-AGB stars	349	323
aO-AGB stars	1244	117
RSG stars	3 325	538
RGB stars	135 437	41
FIR objects	360	360

Notes. The number in parenthesis is the number of stars in the original sample of C-AGB and O-AGB re-classified as aO-AGB stars.
[a] Number of sources with 24 μm counterparts.

Table 4.2: Evolved Star Statistics from Boyer et al. (2011).

AGB Type	Percentage of AGB stars
O-AGB	42.7 ± 1.0%
C-AGB	29.8 ± 0.8%
x-AGB	6.0 ± 0.3%
aO-AGB	21.5 ± 0.7%

the aim of reproducing as accurate as possible the morphology, the color distributions and the star counts.

Figure 4.2 shows the separation of evolved stars in SMC in a J - Ks vs. Ks CMD, resulting from the application of the selection criteria described above. The complete catalog of evolved stars and FIR objects in SMC compiled by Boyer et al. (2011) is available electronically[1] and a sample of the catalog is shown in table 4.3.

[1]Machine-Readable version:
http://iopscience.iop.org/1538-3881/143/5/127/suppdata/aj426961t4_ mrt.txt
Virtual Observatory version:
http://iopscience.iop.org/1538-3881/143/5/127/suppdata/aj426961t4_ votable.xml

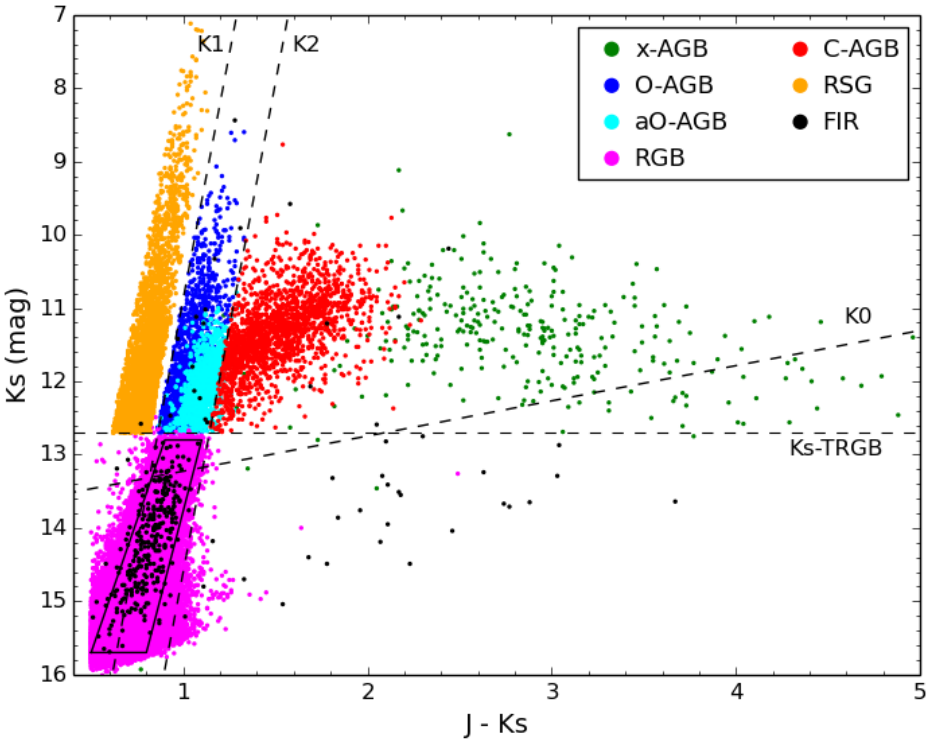

Figure 4.2: CMD showing the separation between RGB (magenta), RSG (orange), C-AGB (red), O-AGB (blue), aO-AGB (cyan), x-AGB stars (green) and FIR (black). The three lines K0, K1, K2 are defined in the text and separate AGB, C- and O-AGB stars, while the black box defines the RGB stars. The Ks-TRGB is also shown. All color-magnitude cuts are explained in the text.

Table 4.3: SAGE-SMC Catalog Sample

Name SSTISAGEMA	Class	2MASS			IRAC				MIPS
		J	H	K	3.6	4.5	5.8	8	24
J004654.98-730834.1	FIR	12.14±0.02	11.72±0.02	11.02±0.02	9.84±0.02	9.24±0.01	8.9±0.02	8.49±0.01	5.49±0.01
J011521.22-733015.0	O-AGB	12.64±0.03	12.35±0.03	11.68±0.03	9.87±0.02	9.25±0.01	8.68±0.01	8.12±0.01	6.89±0.02
J005317.67-724554.4	RSG	10.78±0.03	10.06±0.03	9.87±0.03	9.76±0.01	9.87±0.01	9.77±0.01	9.71±0.01	9.62±0.05
J005241.36-731207.4	RGB	13.62±0.03	13.22±0.03	13.09±0.03	13.06±0.04	13.1±0.03	13.2±0.07		
J005409.52-724143.1	x-AGB	12.32±0.03	11.91±0.04	11.1±0.03	9.18±0.03	8.32±0.03	7.73±0.02	6.93±0.02	4.79±0.01
J005148.79-730243.8	C-AGB	12.76±0.02	11.76±0.02	11.22±0.03	10.66±0.01	10.63±0.01	10.44±0.01	10.1±0.01	
J005147.71-730603.9	aO-AGB	13.34±0.03	12.51±0.04	12.26±0.03	12.02±0.03	12.07±0.01	11.94±0.02	11.82±0.02	

4.4 The Star Formation History of the SMC

In this section, a description of the VMC data available for the SMC will be given as well as the recovery method of the SFH used by Rubele et al. (2015).

4.4.1 The Vista Survey of the Magellanic Clouds

The VISTA Survey of the Magellanic Clouds (VMC) is a uniform and homogeneous survey of the Magellanic system in the near-IR bands (YJKs) with VISTA telescope. The main purposes of the survey, which is extensively described in Cioni et al. (2011), are the determination of the spatially-resolved SFH and the three-dimensional structure of the Magellanic system. VMC is designed to reach the oldest main sequence turn-off points in both the LMC and SMC, allowing the recovery of the SFH with a color-magnitude reconstruction method, which was first planned and tested by Kerber et al. (2009), applied to LMC data by Rubele et al. (2012) and more recently to SMC data by Rubele et al. (2015).

The use of near-IR photometry has the advantage to provide a view of the stellar populations almost unaffected by dust and, since near-infrared light is dominated by cool evolved giants, to better sampling the intermediate-age population. VMC provides also twelve-epochs photometry in the Ks band, allowing the derivation of more precise period-luminosity relations of variable stars, constraints on the distance and possible structures along the line of sight.

Present data of the SMC include most of its stellar mass, all of its bar, a significant fraction of its wing and a few outer regions. The data analysed by Rubele et al. (2015) come from the v1.1 and v1.2 VMC data retrieved from the VISTA Science Archive (VSA)[2] and comprise the ten SMC tiles for which the Ks multi-epoch photometry is almost complete. Figure 4.3 shows a density map of VMC sources with Ks < 18 mag and photometric errors smaller than 0.2 mag. The map is dominated by intermediate-age and old stellar populations and it is evident that the ten tiles cover the SMC main body, all of its bar (the densest blue region across the tiles 3_5, 4_5, 5_6) and more external regions towards N and NE of SMC (tiles 6_3 and 6_5). The VMC tiles used by Rubele et al. (2015) are listed in Table 4.4, which shows the equatorial coordinates of each tile center, the completion of the multi-epoch Ks photometry and some comments about the position of the tiles.

Table 4.4: VMC tiles used by Rubele et al. (2015). For each tile center, the equatorial coordinates and the completion of the multi-epoch Ks photometry are listed.

Tile	α (deg, J2000)	δ (deg, J2000)	Completion in Ks	Comments
SMC 3_3	11.1995	−74.2005	92%	S extreme of bar
SMC 3_5	21.9762	−74.0018	100%	S part of Wing
SMC 4_3	11.2810	−73.1094	88%	SW part of densest bar
SMC 4_4	16.3303	−73.0876	92%	central bar, slightly towards Wing
SMC 4_5	21.2959	−72.9339	92%	central part of Wing
SMC 5_3	11.2043	−72.0267	92%	NW of densest bar
SMC 5_4	16.1918	−71.9850	100%	NE part of densest bar
SMC 5_6	25.4401	−71.5879	88%	$\approx$ 4 deg E of main body
SMC 6_3	11.4311	−70.9266	78%	$\approx$ 1.5 deg NW of main body
SMC 6_5	20.4138	−70.7601	78%	$\approx$ 3 deg NE of main body

The total area covered is about ≈ 14 deg^2 and each tile (≈ 1.5 deg^2) has been subdivided into 12 subregions of $21.0' \times 21.5'$ (≈ 0.12 deg^2) for the SFH recovery. The subregions are numbered as shown in Figure 4.3.

[2] http://horus.roe.ac.uk/vsa

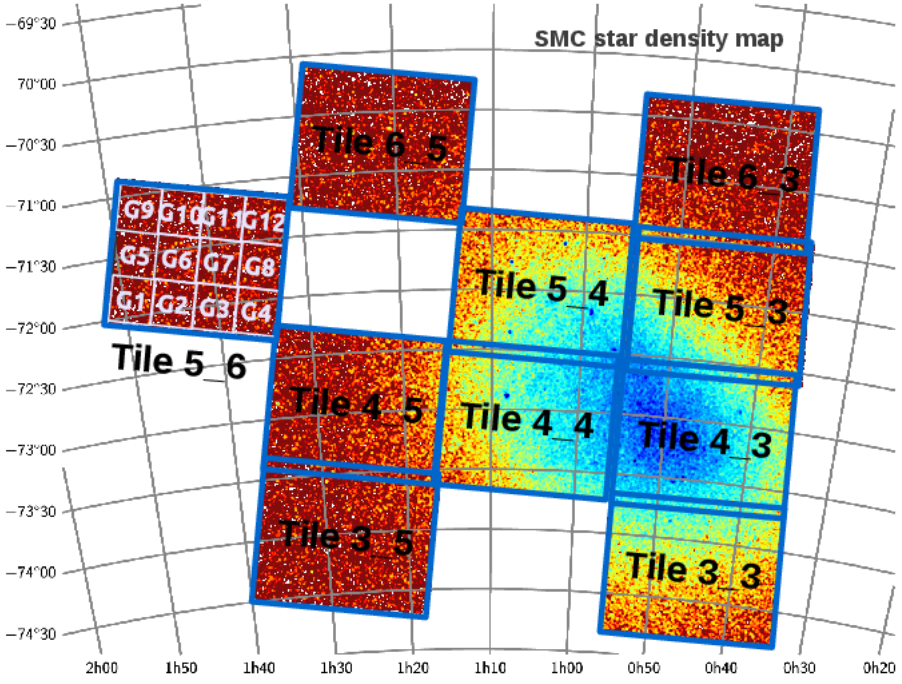

Figure 4.3: Sky position of VMC tiles used by Rubele et al. (2015). Each tile is subdivided into 12 subregions numbered as in tile 5_6.

4.4.2 The SFH recovery

Any method of SFH recovery is based on the assumption that a Composite Ctellar Population (CSP) can be considered as a combination of its constituent parts, which are simple stellar populations (SSP). Thus the recovery of the SFH of a CSP corresponds to the determination of the relative weight of each SSP. The technique is based on a statistical method that allows the recovery of non-parametrised SFH from the CMD of a CSP. The procedure of the SFH recovery is described with all details in Rubele et al. (2012). The key steps for the recovery of the SFH of the SMC, as derived by Rubele et al. (2015), are summarized in the following:

(i) For every subregion of a tile, an absolute distance modulus $(m\text{-}M)_o$ and a V-band extinction A_V is assumed.

(ii) "Partial models" which represents synthetic SSP are computed for age and metallicity bins which are small enough so that the SSP properties do not change significantly inside them and large enough that the SFH recovery could be performed with reasonable CPU times. Age bins are defined as in Rubele et al. (2012) and they are, in general, at equally space intervals of $\Delta log(t/yr) = 0$ dex, but for the youngest age bins for which wider interval are used. This choice is motivated by the fact that the age resolution is better at young ages and that the star counts at very young ages are very small. The reference metallicity for each age bin is defined according to the AMR derived by Piatti (2013c). The metallicity bins are separated by 0.15 dex from each other and a set of 5 partial models for each age bin covering an interval of ± 0.3 dex with respect to the reference metallicity[3] is computed. Table 4.5 shows the grid of partial models used in the SFH

[3]The value of the reference metallicity is derived from Piatti (2013c) AMR and it only used to define

recovery. The partial models are derived from PARSEC v1.0 evolutionary tracks, the same described in Section 3.1, they are computed for the entire range of age and metallicity of relevance and finally shifted to the chosen distance and extinction values.

Table 4.5: Grid of SMC stellar partial models used in the SFH recovery. Table from Rubele et al. (2015).

log(t/yr)	$[Fe/H]_1$	$[Fe/H]_2$	$[Fe/H]_3$	$[Fe/H]_4$	$[Fe/H]_5$
6.9	−0.10	−0.25	−0.40	−0.55	−0.70
7.4	−0.10	−0.25	−0.40	−0.55	−0.70
7.8	−0.10	−0.25	−0.40	−0.55	−0.70
8.1	−0.10	−0.25	−0.40	−0.55	−0.70
8.3	−0.20	−0.35	−0.50	−0.65	−0.80
8.5	−0.20	−0.35	−0.50	−0.65	−0.80
8.7	−0.20	−0.35	−0.50	−0.65	−0.80
8.9	−0.40	−0.55	−0.70	−0.85	−1.00
9.1	−0.55	−0.70	−0.85	−1.00	−1.15
9.3	−0.55	−0.70	−0.85	−1.00	−1.15
9.5	−0.70	−0.85	−1.00	−1.15	−1.30
9.7	−0.85	−1.00	−1.15	−1.30	−1.45
9.9	−1.15	−1.30	−1.45	−1.60	−1.75
10.075	−1.45	−1.60	−1.75	−1.90	−2.05

(3) the partial models are "degraded" to the conditions of the actual observation by applying the distribution of photometric errors and completeness and translated into Hess diagrams, which are maps of stellar density across the (J - Ks, Ks) and (Y - Ks, Ks) CMDs.

(4) By using the StarFISH optimization code by Harris & Zaritsky (2001), adapted for this specific case, the linear combination of partial models the best-fit the observed Hess diagram is determined. The bist-fit solution is derived from the minimisation of a chi-squared (χ^2) like statistics and characterised by the χ^2_{min} value, a measure of the residual between the best-fit model and the data.

(5) The procedure is repeated over a range of different distance moduli and extinctions values spanning from 18.6 - 19.3 mag and 0 - 0.8 mag, respectively. In such a way, the value of the χ^2_{min} allows to determine the best-fit SFH, i.e. SFR(and AMR, in addition to the distance and the extinction in the V-band for each subregion.

(6) By using the same method, one hundred synthetic realization of the best-fit model are performed and analysed in order to derive the dispersion of the resulting coefficients which represents the confidence level of the best-fit SFH, $(m\text{-}M)_o$ and A_V.

As a result of the CMD reconstruction method applied by Rubele et al. (2015) to every subregion of each SMC tile, the best-fitting SFR, AMR, distance and mean reddening, together with 68% confidence intervals, have been derived and will be used in this work as input in the population synthesis code TRILEGAL to simulate the photometry of the SMC. A description of the global SFR and AMR will be given here, while the reader should refer to Rubele et al. (2015) for the detailed analysis of the results for the 120 subregions.

The global SFR of the SMC, as illustrated in Figure 4.4, remained relatively modest, with mean values below 0.015 $M_\odot/yr$, for ages $\gtrsim$ 5 Gyr. An intensification of the SFR is clearly visible at an age of $\approx$ 5 Gyr, when it reached values of about 0.05 $M_\odot/yr$ and a large fraction of the stellar mass of the SMC formed. Between $\approx$ 5 and $\approx$ 1.5 Gyr, i.e. at intermediate ages, the SFR decreased to $\approx$ 0.025 $M_\odot/yr$, but reached another peak of $\approx$ 0.04 $M_\odot/yr$ at $\approx$ 1.5 Gyr. For ages younger than this latter value the resolution is

the location of partial models, thus it has no effect on the final AMR derived from the SFH recovery.

better and the SFR has increased by factors between 2 and 5 with respect to intermediate ages reaching a peak of SFR $\approx 1.25\ M_{\odot}/yr$ between 14 and 40 Myr. Figure 4.4 shows the relative stellar mass formation as a function of age and the cumulative stellar mass normalized to the total formed mass, i.e. $M_{SMC} \approx 3.85 \times 10^8\ M_{\odot}$, in the area sampled by VMC.

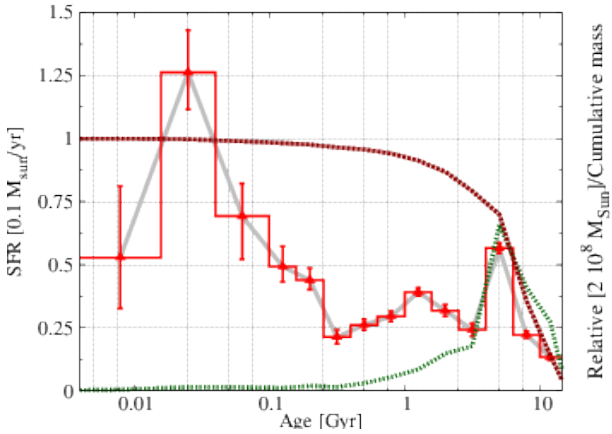

Figure 4.4: Global SFR(t) of the SMC (solid red line) and relative error bars. The relative stellar mass formation as a function of age is shown as a green dotted line and the cumulaive stellar mass normalised to the total formed mass ($3.85 \times 10^8\ M_{\odot}$) as a red dotted line. Rubele et al. (2015).

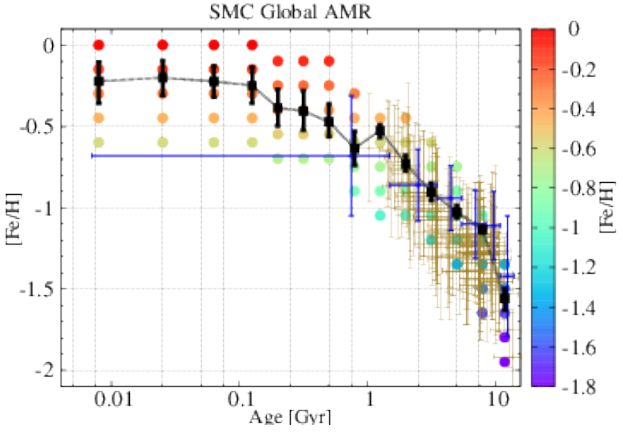

Figure 4.5: Global AMR of the SMC (solid black line) with error bars. The color points show the distribution of the partial models in the AMR diagram. The distribution of clusters analysed in Piatti (2012) is shwon by the the olive points with error bars while the mean metallicity values derived by Carretta et al. (2008) are shown as violet points (the vertical error bars indicate the metallicity dispersion inside the age bins delimited by the horizontal error bars.) Rubele et al. (2015).

The global age-metallicity relation derived by Rubele et al. (2015) is shown in Figure 4.5, from which it is clear that the metallicity has generally increased in time. An interesting feature is present at ages around ~ 1.2 Gyr which indicates an event of dilution in the metallicity that has reached a peak at ~ 1.5 Gyr followed by a decrease at ≈ 0.8 Gyr and then finally a steadily increase. In the same figure, two independents determinations of the AMR are also shown for comparison, one derived from the study of ages and metallicities og star clusters (Piatti 2011c) and the other from calcium triplet observations in 13 different SMC fields (Carrera et al. 2008).

Chapter 5

Simulating the SMC photometry with TRILEGAL

5.1 TRILEGAL input and output

The population synthesis code TRILEGAL produces mock stellar catalogues for a galaxy given its mass, distance, extinction, SFH and age metallicity relation, with the possibility to include the Milky Way foreground population. For a complete description of the code, the reader should refer to Girardi et al. (2005). A general scheme of TRILEGAL code is shown in Figure 5.1. The continuous arrows refer to the processes leading to the simulation of perfect photometric data (i.e. without errors) and they are performed inside the TRILEGAL main code and subroutines; the dashed arrows refer to optional steps, such as the creation of catalogs with photometric errors and they are usually performed with external scripts. In order to simulate the photometry of an external galaxy, the main input datasets are:

1. Tables of stellar evolutionary tracks, giving bolometric magnitude, effective temperature, surface gravity, core mass etc. as a function of initial mass, stellar age and metallicity. The two sets of tracks have been described in Section 3.1.

2. Tables of bolometric corrections for several filter pass-bands as a function of $T_{\rm eff}$, log g, [M/H] and relative absorption in the several pass-bands with respect to the V magnitude.

3. Initial Mass Function (IMF), SFR and AMR of the galaxy to be simulated

4. IMF, SFR, AMR and geometry of the Milky Way components being observed in addition to the external galaxy (usually in the foreground)

Stars are generated through a Monte Carlo simulation, according to a probability distribution and for each star the correspondent age, mass and metallicity are assigned using the SFR, AMR and IMF. The absolute photometry of each star is derived by interpolating grids of evolutionary tracks (or isochrones) and finally it is converted to apparent magnitude by means of bolometric corrections, distance modulus and extinction. The effect of circumstellar dust, which is fundamental in order to reproduce the photometry of TP-AGB stars, is taken into account using tables of bolometric corrections based on the dust models described in Section 3.3. For each simulated star, the main output parameters of a TRILEGAL simulation are bolometric luminosity, intial and final mass, age, metallicity [M/H], C/O ratio, core mass, pulsation period and apparent magnitude in the selected

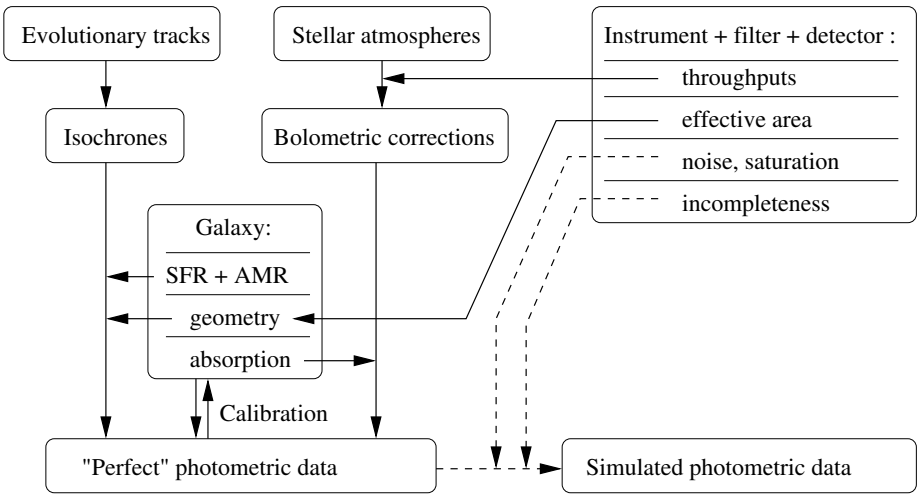

Figure 5.1: TRILEGAL scheme from Girardi et al. (2005)

photometric systems. The flexibility of the code gives the possibility to easily change all the input datasets, hence testing different stellar models and bolometric corrections is quite straightforward.

5.2 Simulating AGB stars in the SMC

The coverage of the SAGE-SMC and VMC surveys, already shown in Figures 4.1 and 4.3, are shown together in Figure 5.2

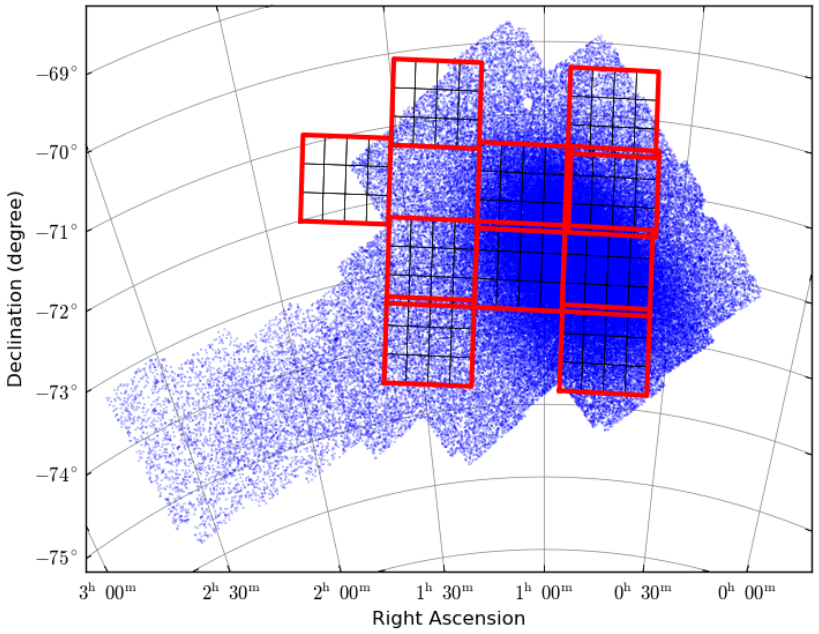

Figure 5.2: SMC stars classified by Boyer et al. (2011) (SAGE-SMC catalog) are shown in blue. The VMC tiles (in red) and subregions (in grey) for which the SFH has been derived is overplotted.

From each subregions of the ten VMC tiles, the stars classified by Boyer et al. (2011)

have been selected. The resulting catalog contains the information already present in the catalog compiled by Boyer et al. (2011) and in addition, every star has been assigned to the appropriate VMC tile and subregion.

Figure 5.3 shows the density map of the SMC stars from the SAGE-SMC catalog which have been classified by Boyer et al. (2011) and for which the SFH is available. In this work, the VMC tiles are numbered from 1 to 10, as shown in Figure 5.3 (the subregions numbering is the same as Rubele et al. (2015)). The VMC subregions completely covered by the SAGE-SMC survey are 99 (of 120) and most of them belongs to tiles from 1 to 7, which corresponds to the SMC main body and its bar (tiles 8, 9 and 10 have only a partial coverage, however they correspond to more external and less dense regions). Since the number of AGB stars in some of the less populated subregions is $\lesssim 20$, a TRILEGAL simulation has been performed for each subregion and the resulting 99 synthetic catalogs have been joined together in order to have statistically significant star counts.

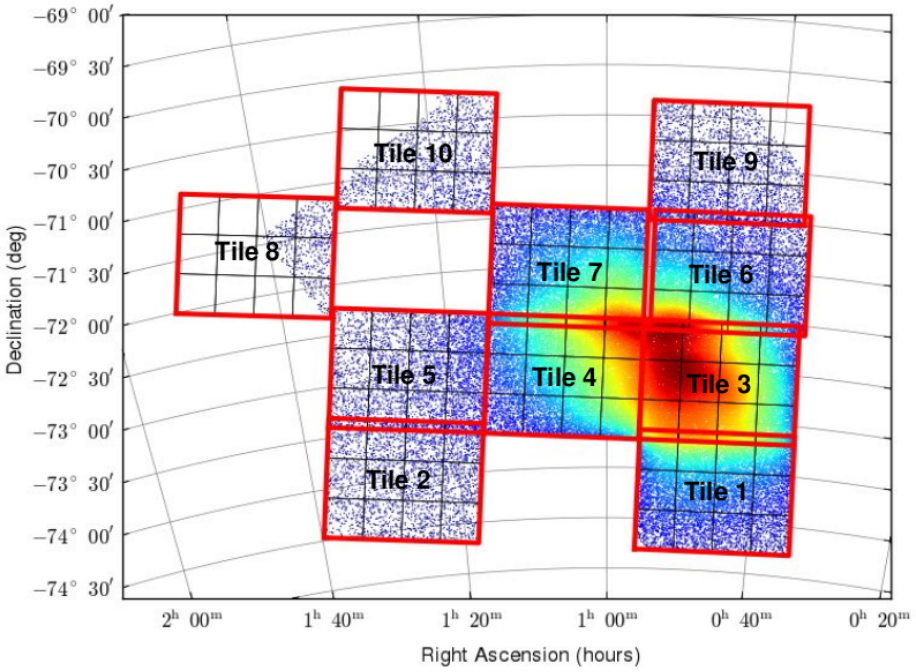

Figure 5.3: Density map of the SMC stars classified by Boyer et al. (2011) for which the SFH has been derived. The ten tiles of the VMC survey are plotted in red and the twelve subregions of each tile are also shown in grey color.

The simulations performed with TRILEGAL result in "perfect photometric catalogs" down to a specified magnitude, according to the input probability distributions, but for the Poisson noise. In order to take into account the photometric errors, the catalogs can be degraded a posteriori either by means of external subroutines or by including a table with actual photometric errors and completeness for each filter. In this work, the latter approach has been used. For each filter, i.e U, B, V, I, J, H, Ks, 3.6μm, 4.5μm, 5.8μm, 8.0μm and 24μm, the corresponding values of magnitude and photometric uncertainties have been extracted from the Boyer et al. (2011) catalog. The magnitudes values have been divided into 10 bins and for each bins the mean value of photometric uncertainties has been computed. As an example, Figure 5.4 shows the photometric errors as a function of magnitudes and the mean photometric errors computed for each magnitude bin, for some of the filters used in the simulation.

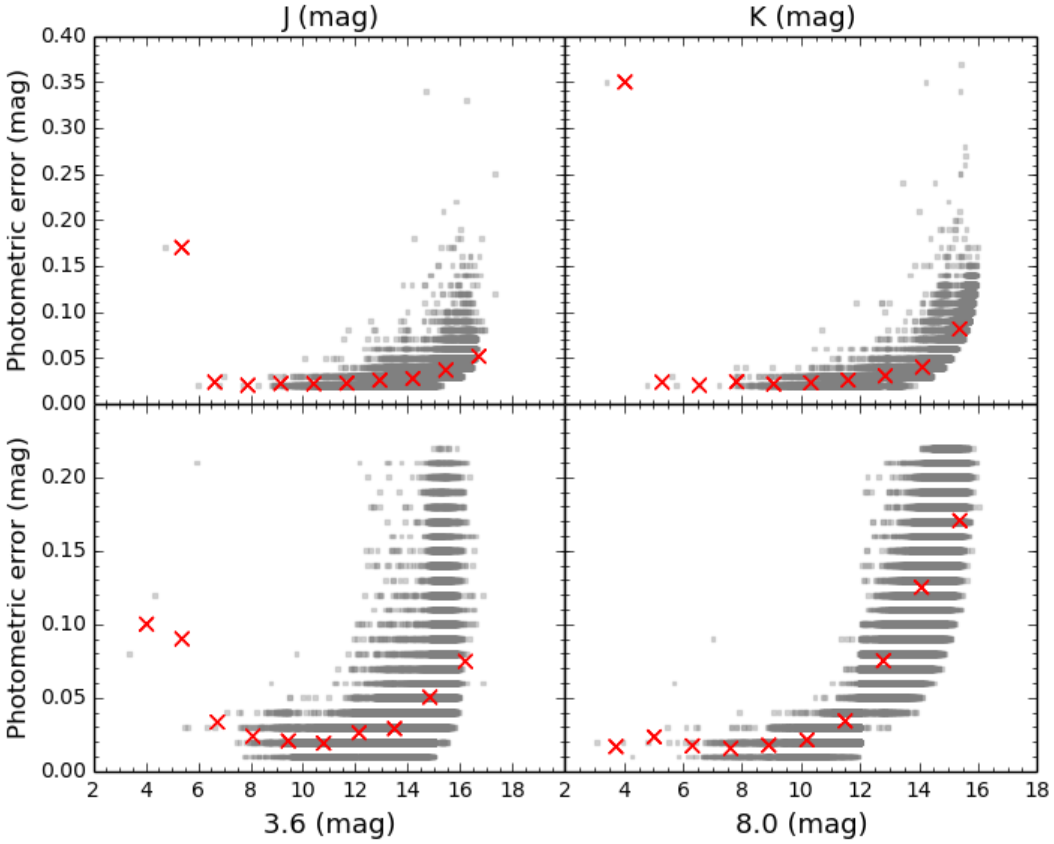

Figure 5.4: Photometric errors as a function of magnitude (grey pixels) and mean photometric errors (red crosses) computed for each magnitude bin, for J, Ks, 3.6μm and 8.0μm bands. Data from Boyer et al. (2011).

Given a set of stellar evolutionary tracks and bolometric corrections the synthetic photometry of each subregion is computed by using the following input data:

(i) The adopted IMF is a Chabrier (2001) log-normal function:

$$\phi_m \propto m \exp\left[-\frac{(\log\ m - \log\ m_0)^2}{2\sigma^2}\right], \tag{5.1}$$

with characteristic mass $m_0 = 0.1\mathrm{M}_\odot$ and dispersion $\sigma = 0.627$.

(ii) The above IMF refers to the mass distribution of single stars, however non-interacting binaries can also be simulated. Briefly, for each primary star of mass m_1, the probability f_b that this star contains a secondary star of mass m_2 is given by a flat distribution of mass rations in the interval $b_b - 1$. The adopted value for f_b and b_b are 0.3 and 0.7 respectively, as in Rubele et al. (2015).

(iii) The extinction in the V-band, as well as the distance values for each subregion are assumed to be the mean reddening value and the mean distance value of the corresponding subregion as derived by Rubele et al. (2015).

(iv) The total stellar mass of each simulated field is derived by integrating the SFR of each subregion over the entire range of age values, used in the SFH recovery. The total number of simulated stars is controlled by this quantity which acts as a normalization factor.

(v) The central coordinates of each subregion are taken from Rubele et al. (2015), while the field area is fixed to ≈ 0.12 deg^2.

(vi) the SFR and AMR are given together in the same input file and for this work only the mean values of SFR and AMR derived by Rubele et al. (2015) have been used. The required information are the values of each age bin, the value of the correspondent SFR (in units of $M_{\odot}/yr$) and the value of the metallicity Z. Whenever necessary, Z is converted to the logarithmic metal [M/H] content through the following approximate relation :

$$[M/H] = \log\left(\frac{Z/X}{Z_{\odot}/X_{\odot}}\right), \tag{5.2}$$

with $Z_{\odot} = 0.0152$. Since in the SMC the value of α enhancement with respect to scaled-solar composition is $[\alpha/Fe] \approx 0$ (Hill et al. 1997), [M/H] $\approx$ [Fe/H]. The accuracy of the [M/H] and [Fe/H] values derived by means of this relation is within ~ 0.03 dex. As an optional parameter, also the logarithmic value of the metallicity dispersion can be included.

As already mentioned above, the total number of simulated stars for a given field is controlled by both the SFR(t) and the stellar mass value of the field. In our case, the mass of each subregion of the SMC has been computed by integrating the SFR(t) over the age values. In order to check the consistency between the number of observed and simulated stars, the best choice is comparing the star counts on the RGB. The modelling of the RGB phase is in fact considered to be much more accurate than the TP-AGB phase and by performing this kind of check one can be quite confident that the total number of simulated stars is consistent with respect to the observed star counts. Thus, the direct comparison between TP-AGB star counts derived by observed and synthetic CMDs can be considered reliable enough to calibrate the TP-AGB lifetimes.

Since the RGB sample from Boyer et al. (2011) is not complete, this check has been performed using the photometric data from the 2MASS All-Sky Point Source Catalog (PSC Skrutskie et al. 2006), which is not corrected for background and foreground contamination. In order to account for the foreground contamination, which is expected to be much more relevant with respect to the background one, a TRILEGAL simulation of the Milky Way foreground has been computed and then added to the mock photometric catalog of the SMC field. Figure 5.5 shows the comparison between the 2MASS data and a TRILEGAL simulation of the SMC field that includes the 99 subregions with SAGE-SMC and VMC coverage. The evolutionary tracks adopted in this case are from `PARSEC` and `COLIBRI`. A rectangular box spanning from $0.5 < \mathrm{J} - \mathrm{K_s} < 1.3$ and $13 < \mathrm{Ks} < 14$ has been defined in order to check the consistency between the number of observed and simulated RGB stars. The model overestimates the RGB star counts in the selected box by about 12.6%.

The main reason that accounts for this discrepancy is the different version of PARSEC tracks used by Rubele et al. (2015) in the SFH recovery. In addition, the uncertainties in the SFH may contribute to this discrepancy. To overcome this issue one possibility could be to recompute the SFH of the SMC by using the same version of `PARSEC` tracks adopted in this work. However, this is a very time consuming procedure and it is beyond the scope of the present work.

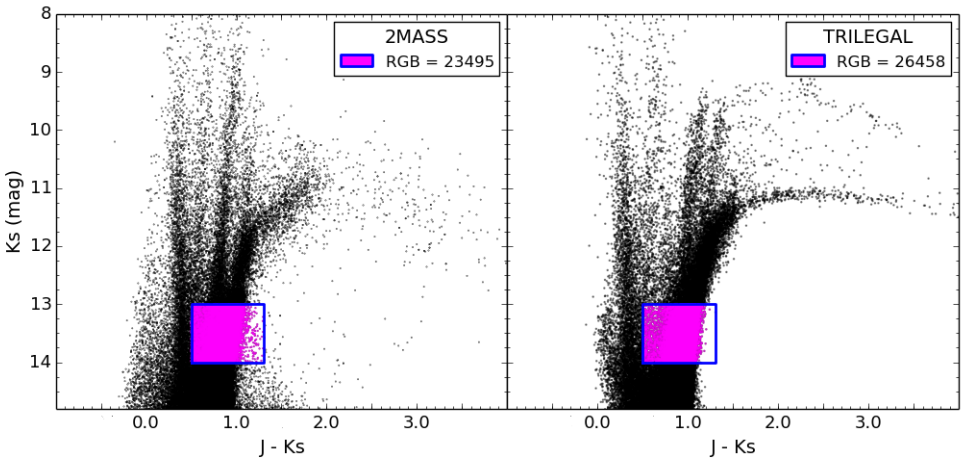

Figure 5.5: 2MASS data (*left*) and TRILEGAL simulation (*right*) of the SMC field that includes the 99 subregions with SAGE-SMC and VMC coverage. The box outlined with a blue line has been defined to check the consistency between the number of observed and simulated RGB stars. The model overestimates the RGB star counts by about 12.6%.

5.3 Selecting AGB stars from the synthetic catalog

Once the 99 single simulations have been joined in a unique synthetic catalog, the next step is the classification of each simulated star which is based on the output stellar parameters. Since the goal of this work is to reproduce as accurately as possible the observed CMDs obtained by Boyer et al. (2011), some of the color-magnitude cuts, described in Section 4.2, have been applied to the synthetic CMDs, in addition to those based only on the stellar outputs predicted by the simulation.

The AGB stars are selected according to a flag which stands for the evolutionary state and the distinction between carbon-rich and oxygen rich AGB stars is based on the C/O ratio: C-AGB stars have a C/O $>$ 1, whereas O-AGB stars have C/O $\leq$ 1. From the set of AGB stars, those with magnitude below the Ks-TRGB and 3.6μm-TRGB, are classified as TP-AGB stars. AGB stars with Ks $>$ 12.7 mag and [3.6] $>$ 12.6 mag are early-AGB stars with magnitudes similar to the most luminous RGB stars.

The extreme AGB stars are selected through the same color-magnitude cuts adopted by Boyer et al. (2011): (1) they are brighter than 3.6μm TRGB and J - [3.6] $>$ 3.1 mag; or (2) they have [3.6] - [8] $>$ 0.8 mag and [3.6]$<$ 3.6μm-TRGB. Since the synthetic photometry is not contaminated by unresolved background galaxies or YSOs, there is no need to apply the two additional criteria used by Boyer et al. (2011), (see Equations 4.4 and 4.5). Furthermore, given that the x-AGB population may include both C-rich and O-rich stars, the sources classified as x-AGB are excluded from the synthetic samples of C-AGB and O-AGB stars.

Boyer et al. (2015) analyzed a sample of 273 aO-AGB stars and found that this population hosts both C-rich and O-rich stars. Since these stars cannot be directly selected from the synthetic catalogs on the basis of their stellar parameters, their contribution to the observed TP-AGB star counts has been taken into account considering that the $\sim$ 45% of anomalous AGB stars turns out to be C-rich and the same percentage (including both M- and S-type spectra) is O-rich (Boyer et al. 2015).

Chapter 6

Comparison of synthetic photometry with observations

In this Chapter, the synthetic photometry derived by the different sets of evolutionary tracks, bolometric corrections and dust models will be compared to the observational data by means of Ks band LFs, J - [8] histograms and CMDs. For each class of TP-AGB stars the corresponding star counts will be compared to those derived from the Boyer et al. (2011) catalog of cool evolved stars of the SMC, in order to provide preliminary indications about the calibration of the TP-AGB life-times, third dredge-up efficiency, mass loss rate and dust production. I emphasize that this kind of detailed analysis can be only carried out by using the stellar models adopted in this study (Marigo and Girardi 2007, Marigo et al. 2013). They are the only models currently available that include the TP-AGB evolutionary phase with the level of completeness and detail necessary to perform a reliable calibration and thus better constrain the key parameters of TP-AGB evolution. In this chapter we will concentrate the discussion on the aspects that regard the TP-AGB evolution. Other models details (SFH, IMF, distances, extinctions, photometric errors) have already been discussed in the previous chapters.

6.1 Simulations dataset

A first set of simulations has been computed without taking into account the effects of dust. For these simulations, the two sets of TP-AGB evolutionary tracks (Gi10 and M13) and the two sets of C-spectra (L01 and A09) have been used. The results will be presented by means of a comparison between the observed J - Ks versus Ks CMD and the synthetic ones and by comparing the star counts of observed and synthetic TP-AGB stars as well. In the second set of simulations the effects of dust have been considered by using different dust bolometric corrections (B98, G06 and N15). On the basis of these simulations, the luminosity functions in the Ks band, the J - Ks versus Ks CMDs and J - [8] histograms have been produced and compared with the observed ones. The different combinations of evolutionary tracks, bolometric corrections, dust models used as input for the TRILEGAL simulations are summarized in Table 6.1.

The uncertainties of both observed and synthetic star counts have been determined by means of the square root of the counts. This approximation is justified by the fact that the present analysis is mainly exploratory. The accurate assessment of the star counts uncertainties will be subject of future works.

Table 6.1: Summary of all input datasets used to simulate the SMC photometry.

Simulation	TP-AGB Tracks	C-star Spectra	Dust Model	SFH
A.1	Gi10	L01	No Dust	Rubele+15
A.2	M13	L01	No Dust	Rubele+15
A.3	Gi10	A09	No Dust	Rubele+15
A.4	M13	A09	No Dust	Rubele+15
B.1	M13	A09	B98	Rubele+15
D.1	M13	A09	G06(1)	Rubele+15
D.2	M13	A09	G06(2)	Rubele+15
D.3	M13	A09	G06(3)	Rubele+15
E	Gi10	A09	N15	Rubele+15
F	M13	A09	N15	Rubele+15

Notes. For G06 calculations, the adopted dust composition for O- and C-rich stars is: (1) 60% AlOx + 40% Silicate and 85% AMC + 15% SiC (2) 100% AlOx and 100% AMC (3) 100% Silicate and 100% AMC.

6.2 Infrared color-magnitude diagrams

6.2.1 Neglecting the effects of dust

As already mentioned, neglecting the reprocessing of photospheric radiation by AGB dusty envelopes leads every model to fail in reproducing the "red tail" of x-AGB stars that characterizes the infrared CMDs of both Magellanic Clouds. By way of example, a first set of simulations have been computed without taking into account the effect of circumstellar dust around AGB stars. The results are shown by means of a comparison between J - Ks vs. Ks synthetic and observed CMDs in Figures 6.1, 6.2, 6.3, 6.4. The star counts for each class of TP-AGB stars and the corresponding uncertainties are shown in Table 6.2.

Table 6.2: TP-AGB star counts obtained from Boyer et al. (2011) catalog and from different combinations of evolutionary tracks and C-star spectra. The effect of dust has been neglected.

Class	Observation	Model			
		M13 & L01	Gi10 & L01	M13 & A09	Gi10 & A09
C-AGB	1516±39 (1989±121)	1997±45	10200±101	2037±62	10510±103
O-AGB	2084±46 (2557±98)	3677±61	2564±51	3772±45	2681±52
x-AGB	300±18	0	0	0	0
a-AGB	1052±33	–	–	–	–

Notes. The number in parenthesis is the total number of C- and O-rich stars obtained as the sum of a-AGB stars expected to be either C-rich or O-rich stars and the number of C-rich and O-rich stars classified by Boyer et al. (2011). The uncertainties associated to the star counts have been estimated by means of the square root of the star counts themselves.

In this case, only a single TRILEGAL simulation of a field that corresponds to tiles from 1 to 7 with a total stellar mass of $\approx 3.44 \times 10^8$ $M_\odot$ and a total area of ≈ 10.5 deg^2, has been computed for the four combinations of evolutionary tracks and carbon star spectra. The extinction in the V-band and the distance values of the simulated field are the mean reddening value (≈ 0.499 mag) and the mean distance value (≈ 59749 pc) of the field. Finally, the SFR and AMR for each subregion of each tile are given together in the same input file. This procedure leads to the loss in resolution of the SFH, but it allows the

computation of a simulation in a shorter time with respect to the procedure described in section 5.2. This choice is motivated by the fact that this first set of synthetic CMDs have been computed only to demonstrate the necessity of including the effect of dust in order to reproduce the very red tail of x-AGB stars.

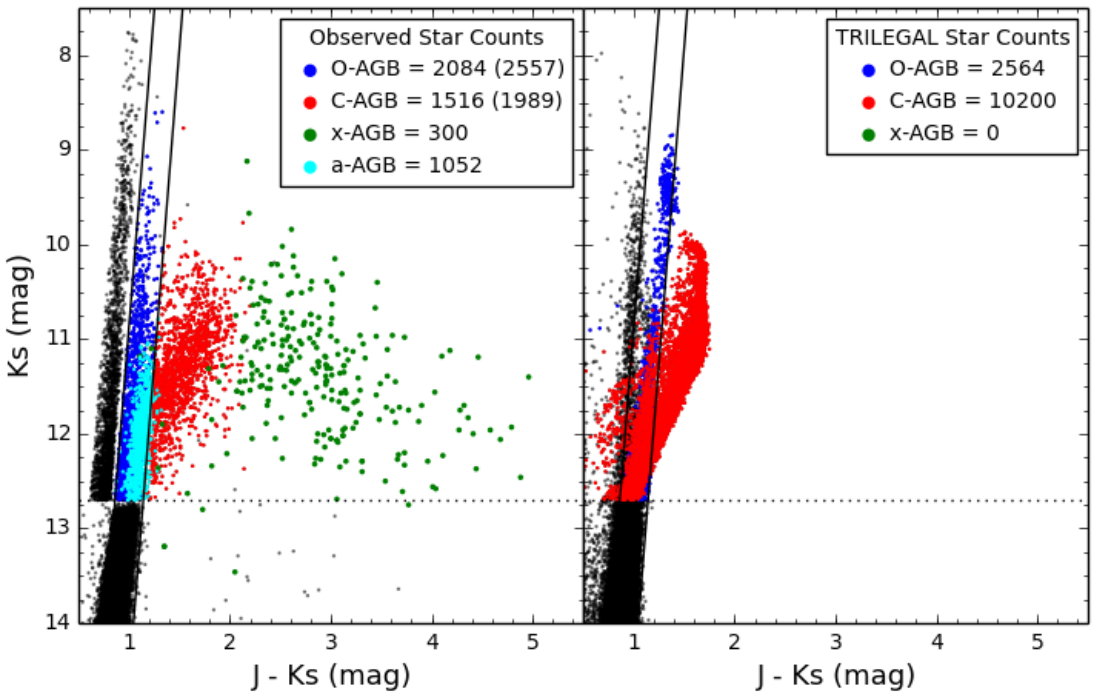

Figure 6.1: The observed J - K vs. Ks CMD (*left*) of the seven SMC tiles covered by both SAGE-SMC and VMC surveys and the simulated CMD (*right*), obtained by using Gi10 evolutionary tracks, C-star spectra from L01 and no dust corrections. C-AGB stars are shown in red, O-AGB in blue, x-AGB in green. The star counts for TP-AGB stars are also shown. In the observed CMD, the class of aO-AGB stars is shown in cyan. The lines that separate the observed sequences of RSG, C-AGB and O-AGB are shown as solid lines. The dotted line is the Ks-TRGB.

Figure 6.1 shows the comparison between the observed J - Ks vs. Ks CMD of the seven SMC tiles covered by both SAGE-SMC and VMC surveys and the simulated CMD (A.1), obtained through the TRILEGAL simulation for which the following inputs have been used: Gi10 evolutionary tracks, C-star spectra from L01 and no dust corrections. C-AGB stars are shown in red, O-AGB in blue, x-AGB in green. In addition, the class of a-AGB stars is shown in cyan in the observed CMD. The star counts for the TP-AGB stars are also shown. Figure 6.2 shows the same kind of comparison, but the simulation has been computed with the evolutionary tracks from M13. The CMDs shown in Figures 6.3 and 6.4 are both computed with C-spectra from A09 and evolutionary tracks from Gi10 and M13, respectively.

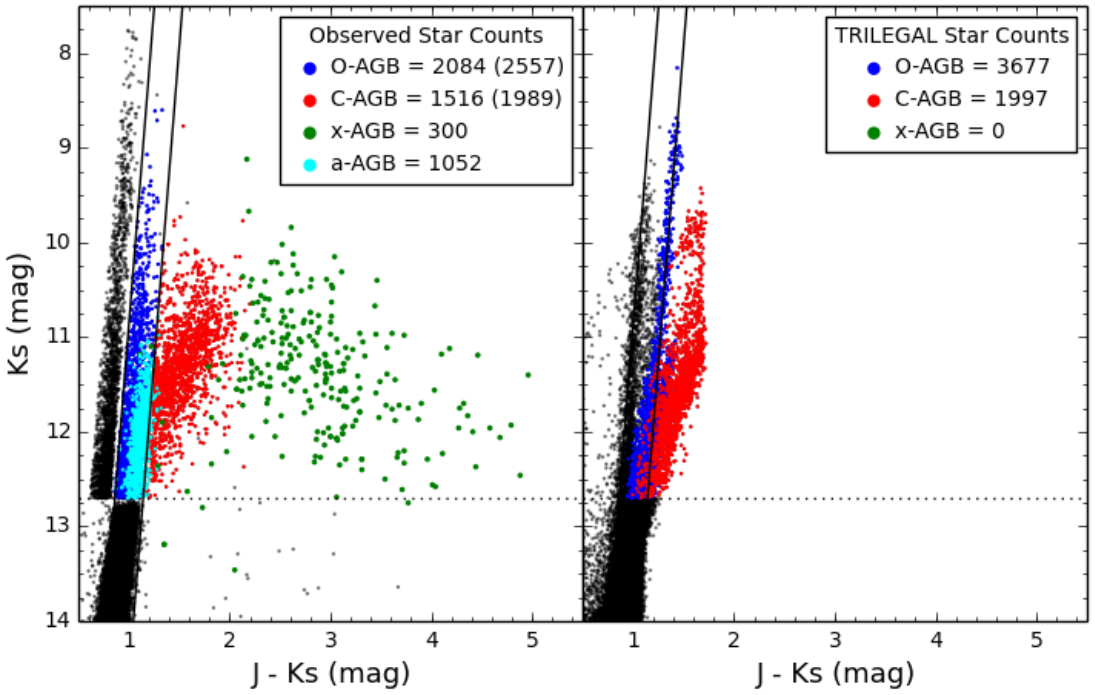

Figure 6.2: The same as in Figure 6.1, with evolutionary tracks from M13 and C-star spectra from L01.

An evident discrepancy, which affects to various extent each model, is that the predicted colors of the RSGs and O-rich AGB sequences are ≈ 0.15 mag redder than the observed one, the difference being much more relevant for the brightest stars. This problem may be due to the fact that the SFR and the AMR have been determined with a fitting procedure that does not include stars brighter than Ks = 12 (see Rubele et al. 2015), but only the less luminous giants (mainly in the RGB and red clump) and stars along the main sequence.

Concerning the color shift, there are basically three reasons that can explain the discrepancy. First, it could be caused by wrong age values being adopted in the SFH recovery. The effect of aging is indeed to shift the color of a population towards the redder part of the CMD. However, this hypothesis is not very likely because the VMC photometry is accurate enough to allow precise age estimates based on the turn-off location. Second, a shift towards redder color may be the result of an over estimation of the metallicity derived through the SFH recovery. Finally, the constant value of the mixing length parameter could not be a reliable approximation when the stellar radius increases along the RGB and AGB. In order to test this hypothesis, it is necessary to recompute all stellar models with different value of mixing length and, even with the use of `COLIBRI` code, it requires a lot of computing time. The color discrepancy will be addressed in future works.

The most evident difference between observed and synthetic CMDs is the absence of TP-AGB stars redder than $J - Ks \approx 1.7$ mag, i.e the x-AGB stars. This feature is common to all synthetic CMDs and it is the result of neglecting the dust effect.

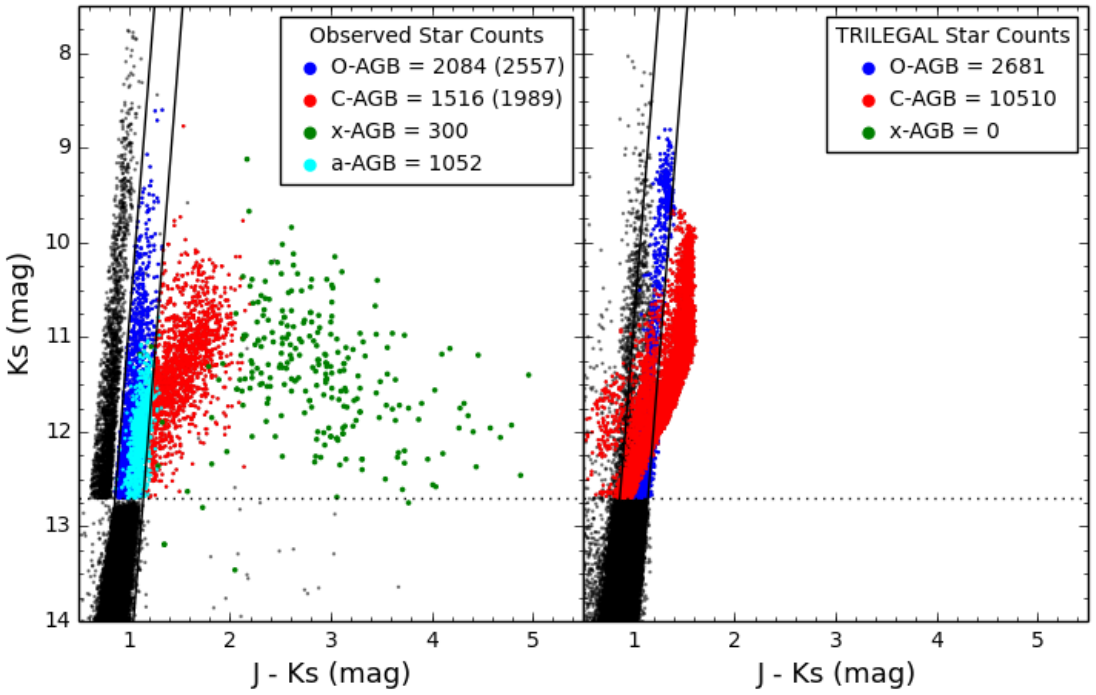

Figure 6.3: The same as in Figure 6.1, with evolutionary tracks from Gi10 and C-star spectra from A09.

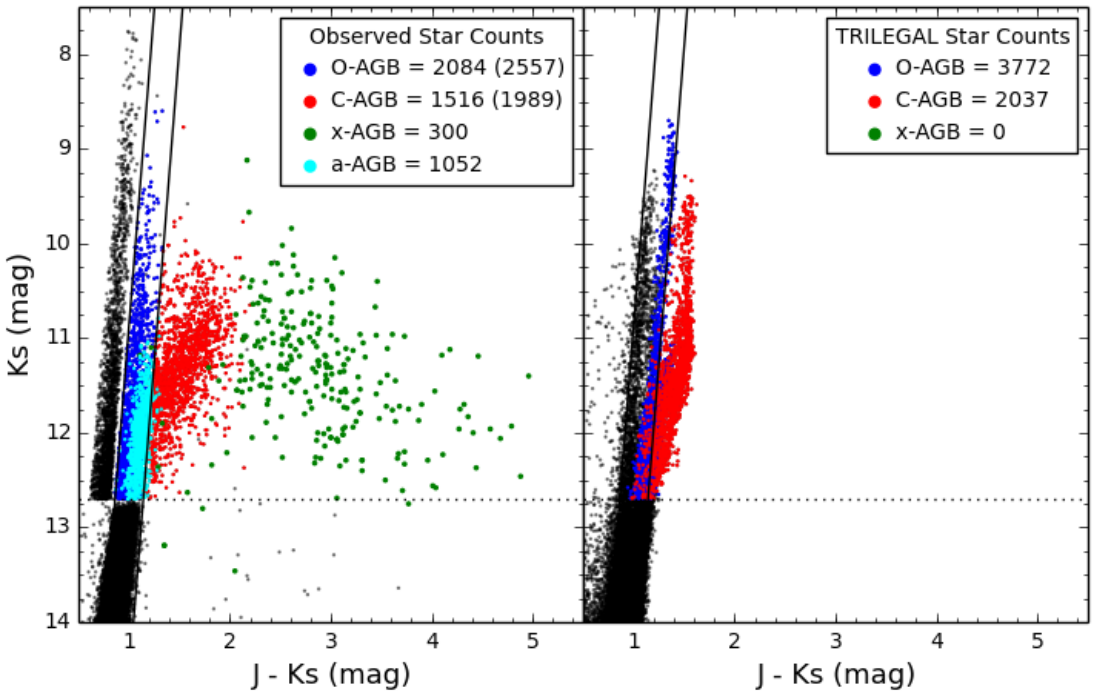

Figure 6.4: The same as in Figure 6.3, with evolutionary tracks from M13 and C-star spectra from A09

By comparing the star counts obtained with the different evolutionary tracks, it is clear that, regardless of the adopted C-spectra, the use of Gi10 tracks leads to an overestimation of the C-AGB star counts by a factor of about 5, while the star counts of carbon stars obtained with the use of M13 tracks is in agreement with the observations within the estimated errors (see Table 6.2). For the O-rich star counts the situation is reversed. By adopting the Gi10 tracks the star counts are well reproduced, while the use M13 tracks leads to an overestimation up to a factor of about 1.5. By looking at the CMDs, it is evident that the synthetic O-rich stars reach higher luminosity with respect to the observed ones, and the values of predicted luminosity and initial mass suggest that these overluminous stars are experiencing HBB. The overestimation of O-AGB star counts is likely caused by an underestimation of the mass loss efficiency of the most massive TP-AGB stars ($\approx$ 3 - 6 $M_{\odot}$) that in turn leads to longer lifetimes. A more detailed analysis of the predicted star counts will be presented in the next section, which shows the luminosity functions, CMDs, J - [8] histograms and star counts derived from simulations in which the effects of circumstellar dust have been taken into account.

6.2.2 The effects of dust

In this section, the synthetic photometry obtained with the inclusion of dust bolometric corrections will be presented. These simulations have been computed by adopting the M13 evolutionary tracks and C-spectra from A09. In addition, a simulation based on Gi10 tracks has been also computed. The different combinations of dust bolometric corrections are shown in Table 6.1. In this case, a simulation has been performed for each subregion of the SMC and the resulting 99 photometric catalogs have been joined in a single catalog, as described in Sec. 5.2.

A qualitative inspection of the J - Ks vs. Ks CMDs (Figs. 6.5, 6.6, 6.7, 6.8, 6.9 and 6.10) shows again a discrepancy between the observed and predicted color of the RSG and O-rich branches. As already explained in the previous section, this may due to factors which are not directly linked with the TP-AGB modelling. On the other hand, it is evident that the inclusion of dust bolometric corrections allows us to reproduce the very red tail of x-AGB stars. However, the various dust prescriptions give different results regarding the predicted star counts, color distributions and apparent magnitudes, especially for the x-AGB stars. Table 6.3 shows the TP-AGB star counts obtained from each model and those obtained from Boyer et al. (2011) catalog. In order to account for the contribution of a-AGB stars, the observed C- and O-AGB star counts have been corrected for the percentage of a-AGB stars that are expected to be C-rich or O-rich.

Table 6.3: TP-AGB star counts and associated errors from Boyer et al. (2011) catalog and from the synthetic catalogs obtained with M13 evolutionary tracks, C-spectra from A09 and different tables of dust bolometric corrections. The star counts obtained with Gi10 evolutionary tracks and dust model by N15 are also shown.

Class	Observation	Evolutionary Tracks and Dust Models					
		Gi10 & N15	M13 & N15	M13 & B98	M13 & G06		
					(1)	(2)	(3)
C-AGB	1531±39 (2013±126)	9783±99	1767±42	1929±44	1844±43	1878±43	1763±42
O-AGB	2113±46 (2595±101)	2342±48	3652±60	3648±60	3609±60	3627±60	3528±60
x-AGB	302±18	1049±32	381±20	187±14	310±18	341±19	347±19
a-AGB	1072±44	–	–	–	–	–	–

Notes. The number in parenthesis is the sum of the number of a-AGB stars expected to be either C-rich or O-rich and the number of C-rich and O-rich stars classified by Boyer et al. (2011).

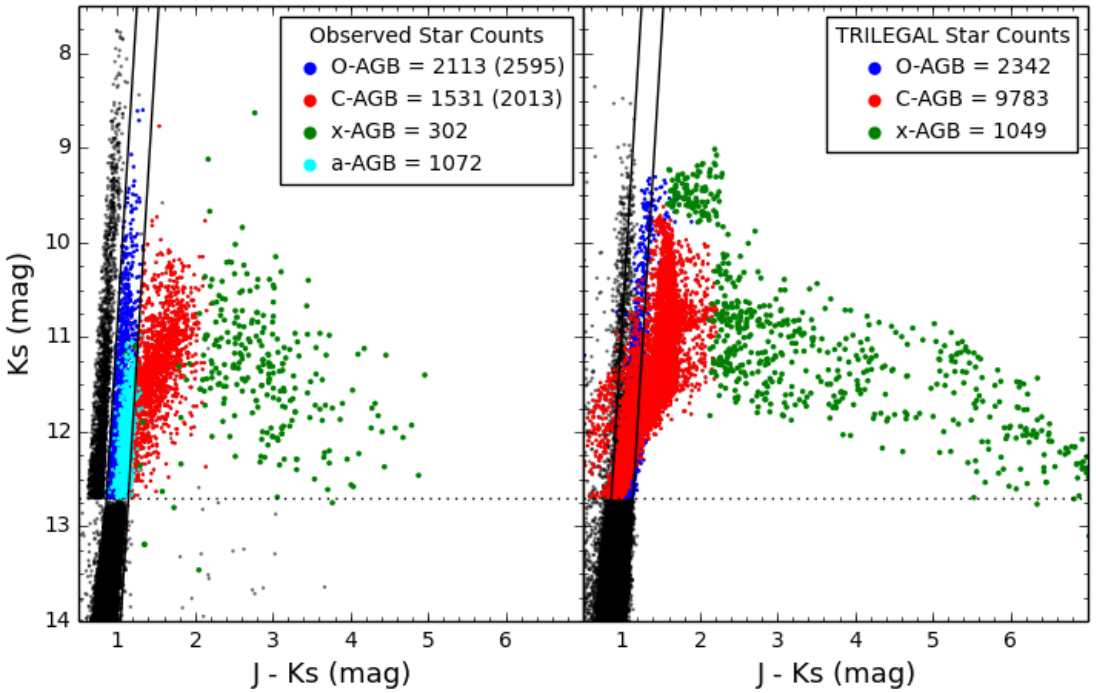

Figure 6.5: The observed J - Ks vs. Ks CMD (*left*) of the SMC field covered by both SAGE-SMC and VMC surveys and the synthetic CMD (*right*) obtained with Gi10 evolutionary tracks, C-star spectra from A09 and dust bolometric corrections from N15. C-AGB stars are shown in red, O-AGB in blue, x-AGB in green. The star counts for TP-AGB stars are also shown. In the observed CMD, the class of aO-AGB stars is shown in cyan. The lines that separate the observed sequences of RSG, C-AGB and O-AGB are shown as solid lines. The dotted line is the Ks-TRGB.

Figure 6.5 shows the comparison between the observed J-K_s vs. K_s CMD of the SMC field covered by both SAGE-SMC and VMC surveys and the simulated CMD obtained by using Gi10 evolutionary tracks, C-star spectra from Aringer et al. (2009) and dust bolometric corrections from N15. Figure 6.6 shows the same kind of comparison, but the adopted evolutionary tracks are from M13. C-AGB star counts from Gi10 tracks result to be largely overestimated (by a factor of ∼4.85), whereas in the case of M13 model the predicted C-AGB star counts are in better agreement, although they are underestimated by about ∼12%. This percentage is different depending on the adopted dust models and in the case of G06(1) it is reduced to ∼7%. It is important to recall that the simulated x-AGB stars have been selected only on the basis of their colors and magnitudes and since the predicted colors result to be slightly shifted with respect to the observed ones, these numbers should be treated with caution.

In the case of an actual underestimation of the predicted C-AGB star counts, the formation of C-rich stars has to be made more efficient. This can be achieved by anticipating the occurrence of the third dredge up, i.e. by decreasing the minimum core mass for dredge-up to start, or by increasing its efficiency. Another alternative would be that of slightly decreasing the mass-loss rates during the C-star phase.

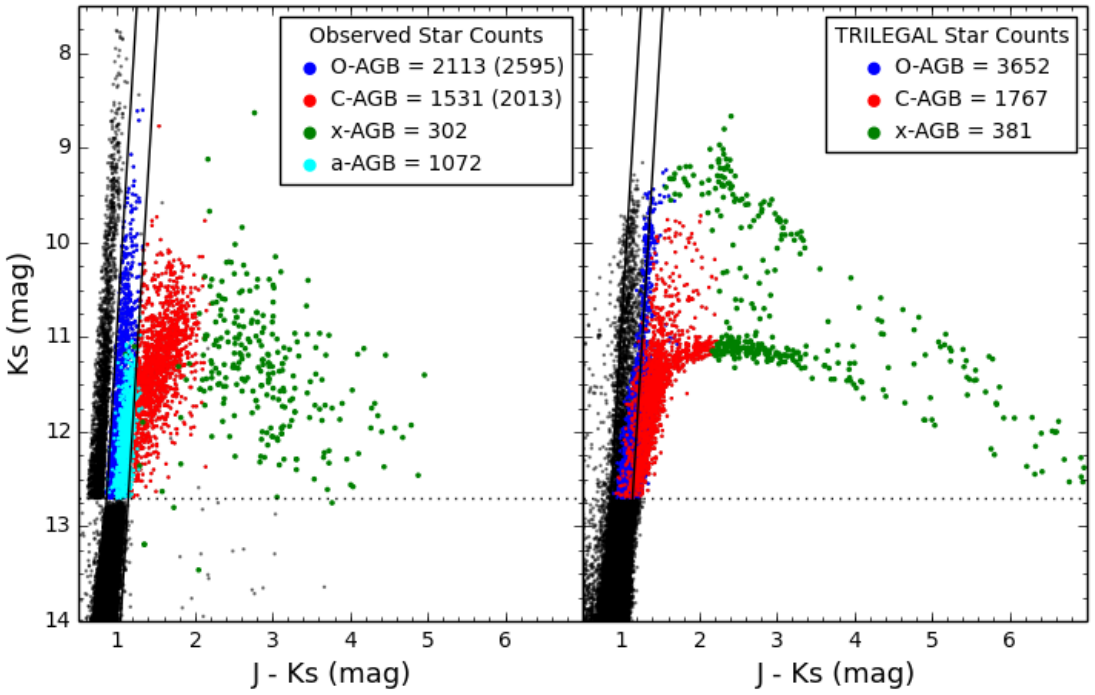

Figure 6.6: The same as in Figure 6.5 but with M13 evolutionary tracks.

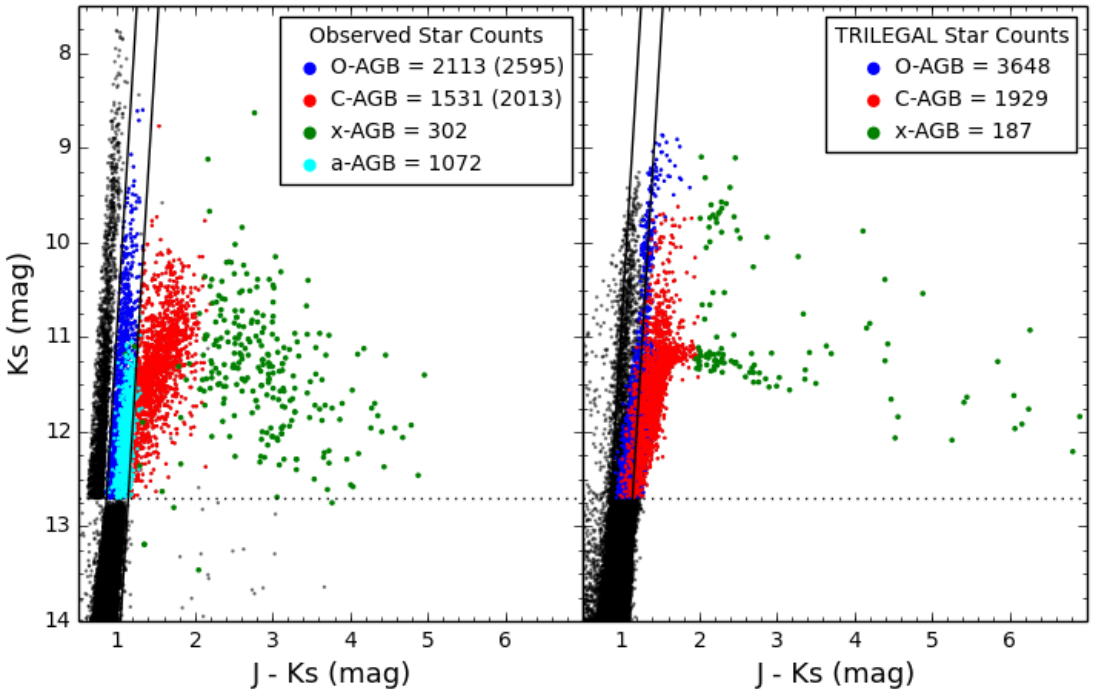

Figure 6.7: The same as in Figure 6.6 with dust bolometric corrections from B98.

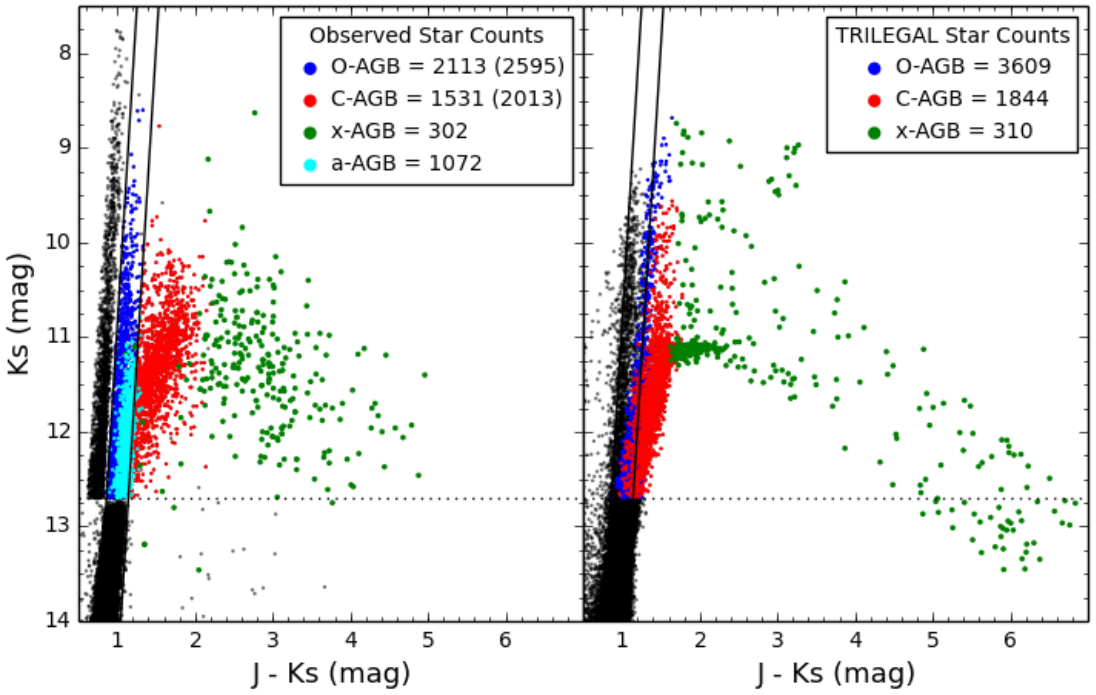

Figure 6.8: The same as in Figure 6.7, but with dust model as in G06 with a combination of of 60% AlOx and 40% Silicate for O-rich stars and a combination of 85% AMC and 15% SiC for C-rich stars.

Figure 6.7, 6.8, 6.9 and 6.10 shows the CMDs obtained by using M13 tracks and different dust bolometric corrections. The synthetic CMD in Figure 6.7 has been computed with B98 dust model, whereas the CMDs in Figures 6.8, 6.9 and 6.10 with G06 model. For G06 computations the adopted dust composition for O- and C-rich stars, respectively is as follows: (1) 60% AlOx + 40% Silicate and 85% AMC + 15% SiC (2) 100% AlOx and 100% AMC (3) 100% Silicate and 100% AMC.

In each model, there is a high concentration of stars at Ks $\approx$ 11 mag which is not visible in the observed CMD. This is likely due to the TP-AGB boosting, an evolutionary effect that occurs for turn-off masses of $\sim$1.75 $M_{\odot}$ and for ages of $\sim$1.6 Gyr (Girardi et al. 2013). Another factor that could contribute to this high concentrated tail is the fact that we do not take into account the variability of TP-AGB stars in the simulations. However, the variability is much more relevant in the optical bands rather than near infrared bands and it is more likely that the cause of the concentration is the boosting effect. Future works will be devoted to the exploration of this issue.

The x-AGB star counts result to be well reproduced in each model, with the exception of B98 that underestimates the number of x-AGB stars. The reason of this discrepancy could be an underestimation of the condensation fraction with respect to the other dust models. A lower condensation fraction produces a lower amount of dust, i.e. a lower optical depth, which in turn implies a lower reddening, hence reducing the number of very red TP-AGB stars. Although the predict x-AGB star counts are in agreement with the observations, the x-AGB J-Ks colors are not exactly reproduced. The overall distribution of these stars extends to redder colors compared to the observed one.

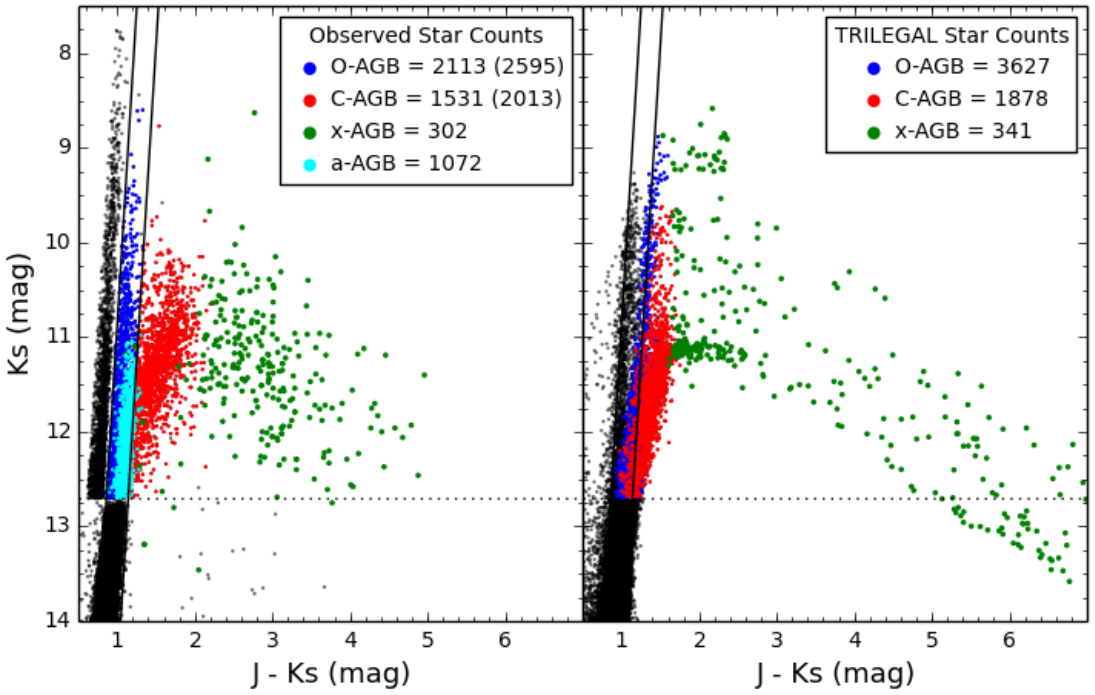

Figure 6.9: The same as in Figure 6.8 but with the following dust composition: 100% AlOx for O-rich stars and 100% AMC for C-rich stars.

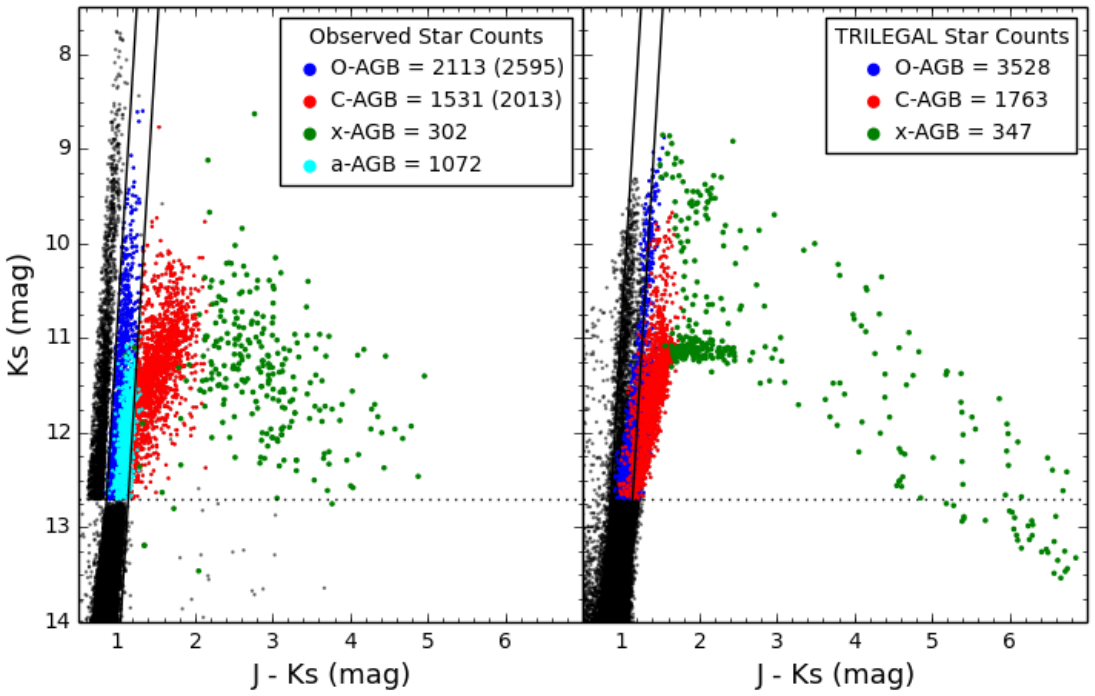

Figure 6.10: The same as in Figure 6.8 but with the following dust composition: 100% Silicate for O-rich stars and 100% AMC for C-rich stars.

In addition, each model predicts a relevant number of O-rich and x-AGB stars brighter than about Ks $\approx$ 10. Among these stars, those that follow into the x-AGB selection criteria result to be O-rich stars. This confirm that the lifetimes of TP-AGB stars with masses between $\approx$ 3 and 6 $M_{\odot}$ need to be reduced.

These comparisons show that the morphology and the star counts are reasonably well reproduced, but there are some discrepancies that are subjects of ongoing studies. In particular, the too extended tail of x-AGB stars seems to be due to the size of the dust grains.

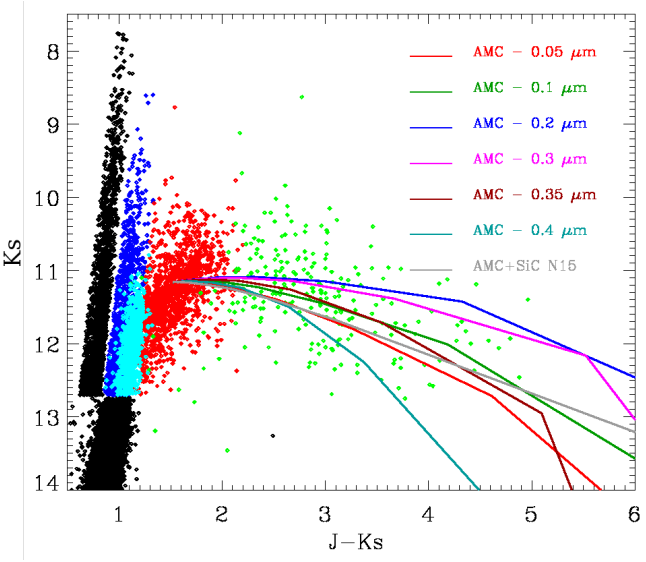

Figure 6.11: Reddening vectors computed by N15 for different grain sizes and applied to a reference C-AGB star of the observed J - Ks v. Ks CMD of the SMC. The adopted dust species is AMC and the vectors are color-coded according to the dust grain sizes. A simulation performed by N15 (grey line) is also shown and it seems to reproduce the mean slope of x-AGB stars in this diagram.

Figure 6.11 shows a series of reddening vectors computed by N15 for different dust grain sizes. The adopted dust species is AMC and the reddening vector are applied to a a reference C-star of the observed CMD. For increasing optical depths they extend towards redder colors until the grain size reaches $0.2\mu m$. When the size is larger than 0.3 μm the absorption in the Ks bands becomes more relevant and for a given J - Ks value also the Ks magnitude is fainter. In the Figure 6.11, a simulation from N15 (grey line) is also shown and it seems to reproduce the mean slope ox x-AGB stars in this diagram.

6.3 Ks luminosity functions and J - [8] histograms

Figure 6.12 shows the comparison between the Ks-band luminosity functions derived from the TRILEGAL simulations with the Gi10 and M13 tracks, upper and lower panels respectively. The adopted C-spectra are those by A09 and the dust model is from N15. The observed LF of TP-AGB stars in the SMC is also shown (grey line).

The better performance of M13 models with respect to Gi10 results to be immediately clear by looking at the LFs of C-rich and x-AGB stars. In general, the magnitude range and the average shape of the LFs of each class of TP-AGB stars is well reproduced by the M13 model. The LF of C-AGB stars shows some discrepancies for magnitude brighter than Ks $\approx$ 11: a slightly underestimation of C-AGB star counts already evident in the synthetic CMDs followed by an overestimation for Ks $\gtrsim$ 10. The O-AGB LF shows an underestimation for Ks between $\approx$ 11.2 and $\approx$ 10.4. In addition, the simulations does not predict O-AGB brigther than Ks $\approx$ 9. In the case of x-AGB stars the most evident discrepancy is the significant number of x-AGB stars predicted to be brighter than Ks $\approx$ 10. The magnitude interval and the shape of x-AGB stars depend on the dust model adopted.

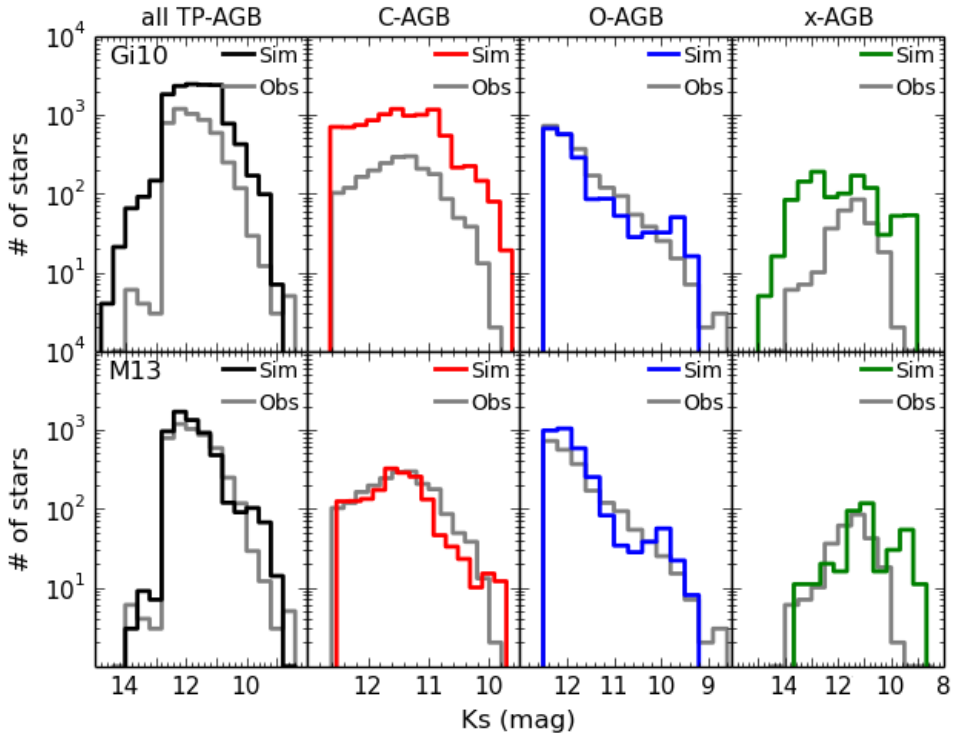

Figure 6.12: Luminosity functions in the Ks band, derived from TRILEGAL simulations using the Gi10 and M31 tracks, and from the observed TP-AGB stars in the SMC Boyer et al. (2011). The adopted dust model is from N15. The solid lines in each panel correspond to the simulated LFs of all TP-AGB (black), C-AGB (red), O-AGB (blue) and x-AGB (green) stars. The grey-line corresponds to Boyer et al. (2011) LF.

Figure 6.13 shows the LFs of TP-AGB stars derived from M13 evolutionary tracks and three sets of dust bolometric corrections. The use of B98 bolometric corrections results in a wider magnitude interval compared to the observations, whereas the magnitude intervals predicted by N15 and G06 are more consistent. The LFs of C-AGB stars results to be affected by the adopted dust bolometric corrections to a small extent. The same is true for the O-AGB LFs, except for Ks $\lesssim$9 where, unlike B98 and G06, N15 model does not predict stars brighter than $\approx$9.4.

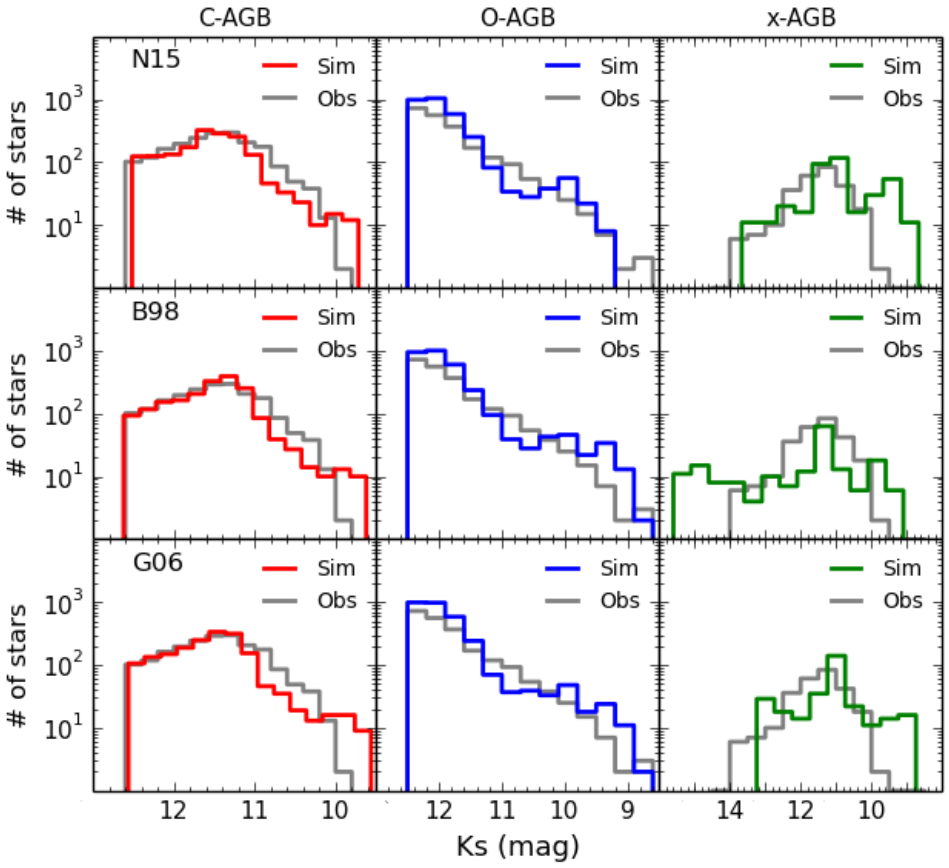

Figure 6.13: Luminosity functions in the Ks band, derived from TRILEGAL simulations using the M13 evolutionary tracks, and from the observed TP-AGB stars in the SMC Boyer et al. (2011). The adopted dust models are from N15, B98 and G06. The solid lines correspond to the simulated LFs of C-AGB (red), O-AGB (blue) and x-AGB (green) stars and the grey-line is the observed LF.

In order to analyze the predicted color distribution, a first set of J - [8] histograms based on M13 and Gi10 evolutionary tracks and dust bolometric corrections from N15 have been produced (Fig. 6.14). As in the case of Ks LFs, the histogram based on M13 tracks result to be more accurate in reproducing the observed J - [8] color distribution with respect to Gi10 tracks. The histogram relative to the whole TP-AGB population is well reproduced in both cases, but for J - [8] $\gtrsim$ 8 mag. This is due to an overestimation of the x-AGB stars with J - [8] color redder than $\approx$ 9 mag (see right-most panel of Fig. 6.14). In the case of C-AGB stars, the better results are obtained with M13 tracks since Gi10 tracks, in addition to the general star counts overestimation, does not reproduce the observed color interval in the blue side (J - [8] $\lesssim$ 1.2) of the histogram. The J - [8] color distribution of O-AGB stars is reproduced quite accurately by both models only in a small color interval (J - [8] $\approx$ 1).

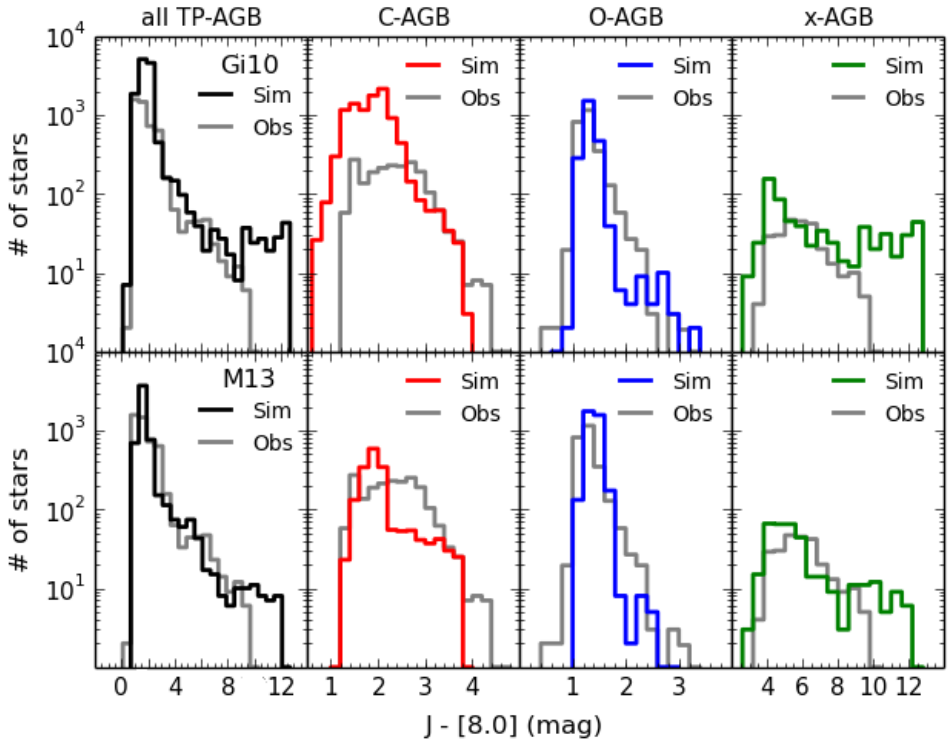

Figure 6.14: J-[8] histograms derived from TRILEGAL simulations using the Gi10 and COLIBRI (M13) tracks, and from the observed TP-AGB stars in the SMC Boyer et al. (2011). The adopted dust model is from N15. The solid lines in each panel correspond to the simulated LFs of all TP-AGB (black), C-AGB (red), O-AGB (blue) and x-AGB (green) stars. The grey-line corresponds to observed LF derived from Boyer et al. (2011) catalog.

Figure 6.15 shows a set of J - [8] histograms computed by using M13 model and N15, B98, G06 dust models. The color interval of C-AGB stars is better reproduced in the case of N15, while B98 and G06 fail to reproduce the color distribution in the redder part of the histogram. In the case of O-AGB stars the adopted dust bolometric corrections affects the color distribution to a smaller extent. On the contrary, the color distribution of x-AGB stars is strongly dependent on dust models and results to be better reproduced in the case of N15.

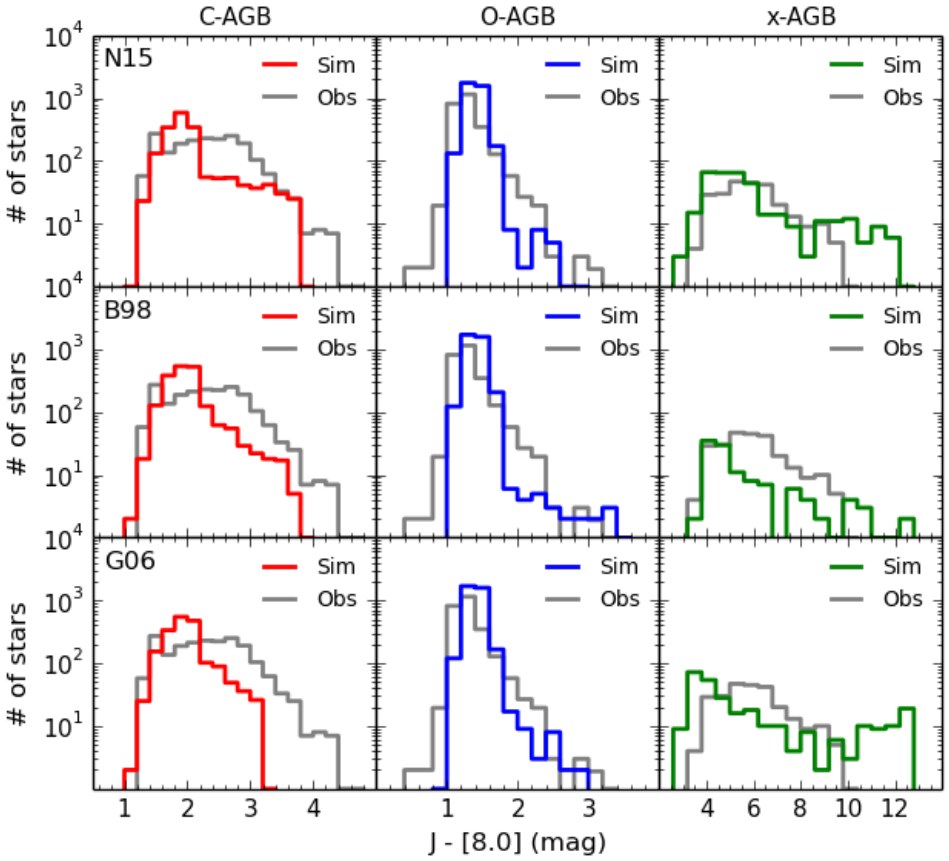

Figure 6.15: J-[8] histograms derived from TRILEGAL simulations using the `COLIBRI` tracks, and from the observed TP-AGB stars in the SMC Boyer et al. (2011). The adopted dust models are from N15, B98 and G06. The solid lines in each panel correspond to the simulated LFs of C-AGB (red), O-AGB (blue) and x-AGB (green) stars. The grey-line corresponds to observed LF derived from Boyer et al. (2011) catalog.

6.4 First indications for the TP-AGB phase calibration

The comparison of the synthetic photometry derived from the TRILEGAL simulations of the SMC with the observations of TP-AGB stars from the SAGE-SMC survey demonstrates that fundamental improvements have been achieved by M13 evolutionary tracks with respect to Gi10. In addition, the new model of dust formation and growth from N15 allows to reproduce the very red tail of x-AGB stars more accurately than B98 and G06. Generally speaking, the predicted star counts of TP-AGB stars, as well as the average shape and magnitude interval of Ks luminosity functions result to be in agreement with observations. However, the detailed comparison between model predictions and observations reveals some discrepancies, which I summarize below together with the corresponding indications for the TP-AGB phase calibration.

(i) An excess of x-AGB stars brighter than Ks $\approx$ 10 mag is predicted. Since these stars turn out to be O-rich HBB stars, their overestimation suggests that the lifetimes of TP-AGB stars with masses above $\approx$ 3 $M_{\odot}$ must be reduced and this, in turn, indicate that the mass-loss efficiency has to be increased.

(ii) The under- and over-prediction of C-AGB and O-AGB star counts that implies a more efficient formation of C-stars which can be obtained by either anticipating the occurrence of the third dredge up or by increasing its efficiency.

(ii) The discrepancies between observed and predicted x-AGB stars color distribution which result from all dust models adopted. This mismatch could be the result of neglecting the x-AGB stars variability, but since in the case of infrared bands this phenomenon is much less relevant than in the optical bands, it is more likely that some prescriptions used in modelling the dust effects should be revised. In this context, very promising results have already been achieved with the N15 models by changing the grain size which affects the optical properties of dust grains formed in the CSEs of TP-AGB stars. The dust effects are indeed much more relevant for x-AGB stars which experience strong mass-losses and possess a thick dusty envelope.

Before proceeding with the actual calibration of the key parameters of TP-AGB evolution, it is necessary to further investigate the above mentioned discrepancies and expand the present grids of TP-AGB evolutionary tracks and dust radiative transfer models. Moreover, some other details of the modelling can be improved, for instance these results have been obtained by using the mean values of SFR, AMR, extinction in the V-band and distance, but not considering the corresponding uncertainties which, despite being not very large, could lead to slightly different results. In addition, the identification of observed TP-AGB stars is only based on photometric classification criteria and it cannot be considered 100% accurate.

Chapter 7

Conclusions and future perspectives

In this thesis, I carried out an exploratory analyses of the synthetic photometry of the SMC derived from the population synthesis code TRILEGAL, with the aim of providing the first indications for extending the calibration of the latest TP-AGB models from Girardi et al. (2010) and Marigo et al. (2013).

Despite its importance in galaxy evolution, the TP-AGB phase is indeed affected by large uncertainties due to the complex interplay between the third dredge-up, the HBB and the mass-loss, for which a robust theory is still lacking. For this reason, it is necessary to calibrate, as a function of age and metallicity, the key parameters of TP-AGB evolution, i.e. stellar lifetimes, efficiencies of third dredge-up and mass-loss, dust production, on the basis of observational data. In this context, substantial improvements of the model calibration come from the high-quality data of resolved TP-AGB populations in nearby and dwarf galaxies, which allow to extend the classic calibration based on Magellanic Clouds clusters.

One of the essential datasets for this work is the catalog of cool evolved stars in the SMC compiled by Boyer et al. (2011), which classified the bulk of TP-AGB stars of the SAGE-SMC survey on the basis of photometric selection criteria. The classification scheme adopted by Boyer et al. (2011) led to separate the TP-AGB population in C-AGB, O-AGB and x-AGB stars. The observed photometry includes optical to far infrared data and has been compared to the synthetic photometry derived from the TRILEGAL simulations.

In order to reproduce as accurately as possible the observed photometry, several theoretical ingredients have been included in the population synthesis code. First, a reliable SFH of the SMC galaxy must be available and second the stellar models must be detailed enough to allow an accurate comparison between observed and predicted quantities. The SFH adopted in this thesis has been derived by Rubele et al. (2015), which used a CMD reconstruction method to recovery the spatially-resolved SFH of 120 subregions of the SMC, including its main body and wing. As a result of this procedure the best-fitting star formation rate, the age metallicity relation, the distance and the mean reddening of each subregion have been used in this work as input for the TRILEGAL simulations. The stellar models from Girardi et al. (2010) and Marigo et al. (2013) are the only TP-AGB models currently available that include the TP-AGB evolutionary phase with the level of completeness necessary to perform a detailed comparison with resolved stellar populations and thus to better constrain the TP-AGB uncertain parameters. In addition, the latest libraries of C- and M- stars spectra Aringer et al. (2009; in prep.) are included in the TRILEGAL code, as well as several sets of dust bolometric corrections based on Bressan

et al. (1998), Groenewegen (2006) and Nanni et al. (2013; in prep.) models. With this respect, taking into account the reprocessing of stellar radiation in the circumstellar dusty envelopes of TP-AGB stars results to be fundamental in order to accurately reproduce the observed photometry. This is evident from the results obtained from the first set of simulations which have been computed without taking into account the dust effects. The comparison between observed and simulated J - Ks versus Ks CMDs revealed that the very red tail of x-AGB stars is not reproduced, regardless of the C-spectra or evolutionary tracks adopted.

The second set of simulations has been computed taking into account the effects of dust by adopting the dust bolometric corrections already mentioned. On the basis of these simulations, the J - Ks versus Ks CMDs, the luminosity functions in the Ks band and J - [8] color histograms for each class of TP-AGB stars have been produced and compared with the observed ones. As a general comment, I found that the predicted TP-AGB star counts, the magnitude intervals and the average shapes of the luminosity functions, as well as the morphology of the observed CMDs result to be better reproduced in the case of Marigo et al. (2013) evolutionary tracks computed by means of the `COLIBRI` code. However, some discrepancies have emerged. The most evident one, not directly linked to the TP-AGB modelling, is related to the predicted colors of the RSGs and O-rich sequences, which result to be redder than the observed ones. The most likely explanation of this color shift, which affects the RGB to a smaller extent, is a possible overestimation of the metallicity derived from the SFH recovery, as well as the failure of a constant mixing length approximation. In addition, each synthetic CMD shows a high concentration of stars (C-rich and x-AGB stars) at Ks $\approx$ 11 which is not visible in the observed CMD. This effect is very likely due to the TP-AGB boosting at ages $\approx$ 1 Gyr, but the variability of TP-AGB stars could also play a role. The color discrepancy as well as the high concentrated tail of stars will be subjects of future investigations.

The detailed comparison of the synthetic CMDs, LFs and histograms derived by using the TP-AGB tracks from Marigo et al. (2013) allowes to provide the first indications for the calibration of the uncertain parameters of the TP-AGB phase.

The excess of O-AGB and x-AGB stars with magnitude brighter than Ks $\approx$ 10 mag indicates that the lifetimes of the most massive TP-AGB stars, experiencing the HBB process, must be shortened. This suggests that the mass-loss efficiency of TP-AGB stars with masses between $\approx$ 3 and 6 $M_{\odot}$ has to be increased.

The underestimation of the predicted C-AGB star counts and the corresponding overestimation of O-rich stars imply that the formation of C-AGB stars must be more efficient. In order to increase the efficiency of C-star formation, one possibility is to anticipate the occurrence of the third dredge-up by decreasing the minimum core-mass for dredge-up to start. Other alternatives or concurring factors would be those of increasing its efficiency as well as slightly decreasing the mass-loss rates during the C-AGB phase.

The discrepancies between the observed and predicted distribution of colors of the x-AGB population, which is strongly dependent on the adopted dust models, suggest that some prescriptions used in modelling the dust effects should be revised. With this respect, some improvements have been already achieved by Nanni et al. (in prep.) by modifying the dust grain size adopted in the dust formation and growth model. Preliminary results show that by increasing the grain size, which affects the optical properties of dust grains in the TP-AGB CSEs, the mean slope of x-AGB stars distribution in the J - Ks versus Ks seems to be better reproduced.

Prior to performing the actual calibration of TP-AGB lifetimes, efficiencies of the third dredge-up, HBB and mass-loss, it is necessary to further investigate the above mentioned

discrepancies and expand the present grids of TP-AGB evolutionary tracks and dust radiative transfer models. Moreover, some other details of the modelling can be improved, for instance these results have been obtained by using the mean values of SFR, AMR, extinction in the V-band and distance, without taking into account the corresponding uncertainties which, despite being not very large, could lead to slightly different results. In addition, the classification of observed TP-AGB stars is only based on photometric criteria and it cannot be considered 100% accurate. A further source of uncertainty comes from the fact that the observed C-AGB and O-AGB star counts have been corrected in order to account for the contribution of the anomalous AGB stars. A relevant number of TP-AGB stars has been indeed originally classified as anomalous O-AGB stars in the Boyer et al. (2011) catalog. However, a further investigation of a sub-sample of anomalous AGB stars, shows that this population hosts both C- and O-rich stars, in the nearly same proportion (Boyer et al. 2015).

On the basis of the present analysis, future works will be devoted to further investigate those discrepancies which, despite not being due to the TP-AGB modelling, would affect the result of a very detailed comparison between observed and synthetic photometry, hence giving inaccurate indications for the calibration of the uncertain parameters of TP-AGB evolution. In addition, further studies will be performed in order to produce grids of models able to reproduce, at the same time, several observable of the SMC, i.e. star counts, mass-loss rates, pulsation periods. In parallel with this, taking advantage of the results based on both photometric and spectroscopic surveys, the identification and classification of TP-AGB resolved populations will be made more accurate than the present one. As a result, the calibration of the TP-AGB phase based on this kind of observations will be made much more reliable. Finally, the same analysis will be carried out for the Large Magellanic Cloud, as soon as its spatially-resolved SFH becomes available.

Bibliography

Alongi, M., Bertelli, G., Bressan, A., and Chiosi, C. (1991). Effects of envelope overshoot on stellar models. A&A, 244:95–106.

Aringer, B., Girardi, L., Nowotny, W., Marigo, P., and Lederer, M. T. (2009). Synthetic photometry for carbon rich giants. I. Hydrostatic dust-free models. A&A, 503:913–928.

Badnell, N. R., Bautista, M. A., Butler, K., Delahaye, F., Mendoza, C., Palmeri, P., Zeippen, C. J., and Seaton, M. J. (2005). Updated opacities from the Opacity Project. MNRAS, 360:458–464.

Bedijn, P. J. (1988). Pulsation, mass loss, and evolution of upper asymptotic giant branch stars. A&A, 205:105–124.

Boothroyd, A. I. and Sackmann, I.-J. (1988a). Low-Mass Stars. II. The Core Mass–Luminosity Relations for Low-Mass Stars. ApJ, 328:641.

Boothroyd, A. I. and Sackmann, I.-J. (1988b). Low-Mass Stars. III. Low-Mass Stars with Steady Mass Loss: Up to the Asymptotic Giant Branch and through the Final Thermal Pulses. ApJ, 328:653.

Bowen, G. H. and Willson, L. A. (1991). From wind to superwind - The evolution of mass-loss rates for Mira models. ApJ, 375:L53–L56.

Boyer, M. L., McDonald, I., Srinivasan, S., Zijlstra, A., van Loon, J. T., Olsen, K. A. G., and Sonneborn, G. (2015). Identification of a Class of Low-mass Asymptotic Giant Branch Stars Struggling to Become Carbon Stars in the Magellanic Clouds. ApJ, 810:116.

Boyer, M. L., Srinivasan, S., van Loon, J. T., McDonald, I., Meixner, M., Zaritsky, D., Gordon, K. D., Kemper, F., Babler, B., Block, M., Bracker, S., Engelbracht, C. W., Hora, J., Indebetouw, R., Meade, M., Misselt, K., Robitaille, T., Sewiło, M., Shiao, B., and Whitney, B. (2011). Surveying the Agents of Galaxy Evolution in the Tidally Stripped, Low Metallicity Small Magellanic Cloud (SAGE-SMC). II. Cool Evolved Stars. AJ, 142:103.

Bressan, A., Fagotto, F., Bertelli, G., and Chiosi, C. (1993). Evolutionary sequences of stellar models with new radiative opacities. II - Z = 0.02. A&AS, 100:647–664.

Bressan, A., Granato, G. L., and Silva, L. (1998). Modelling intermediate age and old stellar populations in the Infrared. A&A, 332:135–148.

Bressan, A., Marigo, P., Girardi, L., Salasnich, B., Dal Cero, C., Rubele, S., and Nanni, A. (2012). PARSEC: stellar tracks and isochrones with the PAdova and TRieste Stellar Evolution Code. MNRAS, 427:127–145.

Caffau, E., Ludwig, H.-G., Steffen, M., Freytag, B., and Bonifacio, P. (2011). Solar Chemical Abundances Determined with a CO5BOLD 3D Model Atmosphere. Sol. Phys., 268:255–269.

Chen, Y., Bressan, A., Girardi, L., Marigo, P., Kong, X., and Lanza, A. (2015). PARSEC evolutionary tracks of massive stars up to 350 M_{odot} at metallicities $0.0001 \leq Z \leq 0.04$. MNRAS, 452:1068–1080.

Cioni, M.-R. L., Clementini, G., Girardi, L., Guandalini, R., Gullieuszik, M., Miszalski, B., Moretti, M.-I., Ripepi, V., Rubele, S., Bagheri, G., Bekki, K., Cross, N., de Blok, W. J. G., de Grijs, R., Emerson, J. P., Evans, C. J., Gibson, B., Gonzales-Solares, E., Groenewegen, M. A. T., Irwin, M., Ivanov, V. D., Lewis, J., Marconi, M., Marquette, J.-B., Mastropietro, C., Moore, B., Napiwotzki, R., Naylor, T., Oliveira, J. M., Read, M., Sutorius, E., van Loon, J. T., Wilkinson, M. I., and Wood, P. R. (2011). The VMC survey. I. Strategy and first data. A&A, 527:A116.

Cioni, M.-R. L., Girardi, L., Marigo, P., and Habing, H. J. (2006). AGB stars in the Magellanic Clouds. II. The rate of star formation across the LMC. A&A, 448:77–91.

Frogel, J. A., Mould, J., and Blanco, V. M. (1990). The asymptotic giant branch of Magellanic Cloud clusters. ApJ, 352:96–122.

Gail, H.-P. and Sedlmayr, E. (1987). Dust formation in stellar winds. V - The minimum mass loss rate for dust-driven winds. A&A, 177:186–192.

Girardi, L., Bressan, A., Bertelli, G., and Chiosi, C. (2000). Evolutionary tracks and isochrones for low- and intermediate-mass stars: From 0.15 to 7 M_{sun}, and from Z=0.0004 to 0.03. A&AS, 141:371–383.

Girardi, L., Groenewegen, M. A. T., Hatziminaoglou, E., and da Costa, L. (2005). Star counts in the Galaxy. Simulating from very deep to very shallow photometric surveys with the TRILEGAL code. A&A, 436:895–915.

Girardi, L., Marigo, P., Bressan, A., and Rosenfield, P. (2013). The Insidious Boosting of Thermally Pulsing Asymptotic Giant Branch Stars in Intermediate-age Magellanic Cloud Clusters. ApJ, 777:142.

Girardi, L., Williams, B. F., Gilbert, K. M., Rosenfield, P., Dalcanton, J. J., Marigo, P., Boyer, M. L., Dolphin, A., Weisz, D. R., Melbourne, J., Olsen, K. A. G., Seth, A. C., and Skillman, E. (2010). The ACS Nearby Galaxy Survey Treasury. IX. Constraining Asymptotic Giant Branch Evolution with Old Metal-poor Galaxies. ApJ, 724:1030–1043.

Gordon, K. D., Meixner, M., Meade, M. R., Whitney, B., Engelbracht, C., Bot, C., Boyer, M. L., Lawton, B., Sewiło, M., Babler, B., Bernard, J.-P., Bracker, S., Block, M., Blum, R., Bolatto, A., Bonanos, A., Harris, J., Hora, J. L., Indebetouw, R., Misselt, K., Reach, W., Shiao, B., Tielens, X., Carlson, L., Churchwell, E., Clayton, G. C., Chen, C.-H. R., Cohen, M., Fukui, Y., Gorjian, V., Hony, S., Israel, F. P., Kawamura, A., Kemper, F., Leroy, A., Li, A., Madden, S., Marble, A. R., McDonald, I., Mizuno, A., Mizuno, N., Muller, E., Oliveira, J. M., Olsen, K., Onishi, T., Paladini, R., Paradis, D., Points, S., Robitaille, T., Rubin, D., Sandstrom, K., Sato, S., Shibai, H., Simon, J. D., Smith, L. J., Srinivasan, S., Vijh, U., Van Dyk, S., van Loon, J. T., and Zaritsky, D. (2011). Surveying the Agents of Galaxy Evolution in the Tidally Stripped, Low Metallicity Small Magellanic Cloud (SAGE-SMC). I. Overview. AJ, 142:102.

Grevesse, N. and Sauval, A. J. (1998). Standard Solar Composition. Space Sci. Rev., 85:161–174.

Groenewegen, M. A. T. (2006). The mid- and far-infrared colours of AGB and post-AGB stars. A&A, 448:181–187.

Groenewegen, M. A. T. (2012). An extension of the DUSTY radiative transfer code and an application to OH 26.5 and TT Cygni. A&A, 543:A36.

Groenewegen, M. A. T. and de Jong, T. (1993). Synthetic AGB evolution. I - A new model. A&A, 267:410–432.

Herwig, F. (2005). Evolution of Asymptotic Giant Branch Stars. ARA&A, 43:435–479.

Hill, V., Barbuy, B., and Spite, M. (1997). Carbon, nitrogen, oxygen and lithium abundances of six cool supergiants in the SMC. A&A, 323:461–468.

Ivezic, Z., Nenkova, M., and Elitzur, M. (1999). User Manual for DUSTY. *ArXiv Astrophysics e-prints*.

Izzard, R. G., Tout, C. A., Karakas, A. I., and Pols, O. R. (2004). A new synthetic model for asymptotic giant branch stars. MNRAS, 350:407–426.

Kalirai, J. S., Saul Davis, D., Richer, H. B., Bergeron, P., Catelan, M., Hansen, B. M. S., and Rich, R. M. (2009). The Masses of Population II White Dwarfs. ApJ, 705:408–425.

Karakas, A. I. and Lattanzio, J. C. (2014). The Dawes Review 2: Nucleosynthesis and Stellar Yields of Low- and Intermediate-Mass Single Stars. PASA, 31:30.

Karakas, A. I., Lattanzio, J. C., and Pols, O. R. (2002). Parameterising the Third Dredge-up in Asymptotic Giant Branch Stars. PASA, 19:515–526.

Kerber, L. O., Girardi, L., Rubele, S., and Cioni, M.-R. (2009). Recovery of the star formation history of the LMC from the VISTA survey of the Magellanic system. A&A, 499:697–710.

Lagadec, E., Zijlstra, A. A., Sloan, G. C., Matsuura, M., Wood, P. R., van Loon, J. T., Harris, G. J., Blommaert, J. A. D. L., Hony, S., Groenewegen, M. A. T., Feast, M. W., Whitelock, P. A., Menzies, J. W., and Cioni, M.-R. (2007). Spitzer spectroscopy of carbon stars in the Small Magellanic Cloud. MNRAS, 376:1270–1284.

Loidl, R., Lançon, A., and Jørgensen, U. G. (2001). Spectra of carbon-rich asymptotic giant branch stars between 0.5 and 2.5 mu m: Theory meets observation. A&A, 371:1065–1077.

Marigo, P. and Aringer, B. (2009). Low-temperature gas opacity. ÆSOPUS: a versatile and quick computational tool. A&A, 508:1539–1569.

Marigo, P., Bressan, A., Nanni, A., Girardi, L., and Pumo, M. L. (2013). Evolution of thermally pulsing asymptotic giant branch stars - I. The COLIBRI code. MNRAS, 434:488–526.

Marigo, P. and Girardi, L. (2007). Evolution of asymptotic giant branch stars. I. Updated synthetic TP-AGB models and their basic calibration. A&A, 469:239–263.

Marigo, P., Girardi, L., and Bressan, A. (1999). The third dredge-up and the carbon star luminosity functions in the Magellanic Clouds. A&A, 344:123–142.

Marigo, P., Girardi, L., Bressan, A., Groenewegen, M. A. T., Silva, L., and Granato, G. L. (2008). Evolution of asymptotic giant branch stars. II. Optical to far-infrared isochrones with improved TP-AGB models. A&A, 482:883–905.

Marigo, P., Girardi, L., and Chiosi, C. (2003). The red tail of carbon stars in the LMC: Models meet 2MASS and DENIS observations. A&A, 403:225–237.

Nanni, A., Bressan, A., Marigo, P., and Girardi, L. (2013). Evolution of thermally pulsing asymptotic giant branch stars - II. Dust production at varying metallicity. MNRAS, 434:2390–2417.

Nowotny, W., Höfner, S., and Aringer, B. (2010). Line formation in AGB atmospheres including velocity effects. Molecular line profile variations of long period variables. A&A, 514:A35.

Reimers, D. (1975). Circumstellar absorption lines and mass loss from red giants. *Memoires of the Societe Royale des Sciences de Liege*, 8:369–382.

Renzini, A. and Buzzoni, A. (1986). Global properties of stellar populations and the spectral evolution of galaxies. In Chiosi, C. and Renzini, A., editors, *Spectral Evolution of Galaxies*, volume 122 of *Astrophysics and Space Science Library*, pages 195–231.

Rubele, S., Girardi, L., Kerber, L., Cioni, M.-R. L., Piatti, A. E., Zaggia, S., Bekki, K., Bressan, A., Clementini, G., de Grijs, R., Emerson, J. P., Groenewegen, M. A. T., Ivanov, V. D., Marconi, M., Marigo, P., Moretti, M.-I., Ripepi, V., Subramanian, S., Tatton, B. L., and van Loon, J. T. (2015). The VMC survey - XIV. First results on the look-back time star formation rate tomography of the Small Magellanic Cloud. MNRAS, 449:639–661.

Rubele, S., Kerber, L., Girardi, L., Cioni, M.-R., Marigo, P., Zaggia, S., Bekki, K., de Grijs, R., Emerson, J., Groenewegen, M. A. T., Gullieuszik, M., Ivanov, V., Miszalski, B., Oliveira, J. M., Tatton, B., and van Loon, J. T. (2012). The VMC survey. IV. The LMC star formation history and disk geometry from four VMC tiles. A&A, 537:A106.

Schröder, K.-P. and Cuntz, M. (2005). A New Version of Reimers' Law of Mass Loss Based on a Physical Approach. ApJ, 630:L73–L76.

Schröder, K.-P., Wachter, A., and Winters, J. M. (2003). The IR-colour-mass-loss relation of carbon-rich, dust-driven superwinds and a synthetic (J-K, M_{Bol}) diagram. A&A, 398:229–237.

Seaton, M. J. (2005). Opacity Project data on CD for mean opacities and radiative accelerations. MNRAS, 362:L1–L3.

Skrutskie, M. F., Cutri, R. M., Stiening, R., Weinberg, M. D., Schneider, S., Carpenter, J. M., Beichman, C., Capps, R., Chester, T., Elias, J., Huchra, J., Liebert, J., Lonsdale, C., Monet, D. G., Price, S., Seitzer, P., Jarrett, T., Kirkpatrick, J. D., Gizis, J. E., Howard, E., Evans, T., Fowler, J., Fullmer, L., Hurt, R., Light, R., Kopan, E. L., Marsh, K. A., McCallon, H. L., Tam, R., Van Dyk, S., and Wheelock, S. (2006). The Two Micron All Sky Survey (2MASS). AJ, 131:1163–1183.

Vassiliadis, E. and Wood, P. R. (1993). Evolution of low- and intermediate-mass stars to the end of the asymptotic giant branch with mass loss. ApJ, 413:641–657.

Wagenhuber, J. and Groenewegen, M. A. T. (1998). New input data for synthetic AGB evolution. A&A, 340:183–195.

Willson, L. A. (2000). Mass Loss From Cool Stars: Impact on the Evolution of Stars and Stellar Populations. ARA&A, 38:573–611.